AN ABSTRACT OF THE THESIS OF

Gregory Nigon for the degree of Master of Science in Materials Science presented on March 5, 2020.

Title: Selective Laser Melting of Duplex Stainless Steel 2205 for Seawater Applications: Microstructure, Mechanical Properties, and Corrosion Performance

Abstract approved: _____

Somayeh Pasebani O. Burkan Isgor

The aim of this work was to assess the viability of duplex stainless steel 2205 components built via selective laser melting for seawater applications. First, a comprehensive additive manufacturing assessment was done. The duplex stainless steel 2205 components were selectively laser melted from gas atomized powder (D90 <45μm) using a 250 W laser in nitrogen environment. A relative density of 99.1±0.3% was achieved, but a heat treatment was necessary to restore the balanced duplex microstructure. A comparison of electron backscatter diffraction, optical microscopy, and magnetometer phase analysis techniques was done yielding ferrite contents of 51.7±0.7 %, 53.0±4.8 %, and 55.7±1.0 %, respectively. The grain orientation before and after heat treatment was heavily influenced by the layerwise building and scan strategy, which resulted in a [001] ferritic texture. However, the austenite had a mixed orientation. The processing conditions did not affect the bulk chemical composition, however elemental segregation was observed. Characterization of bulk properties was done on samples built from optimized parameters. While the measured microhardness of 258±8 HV was comparable to wrought, the ultimate tensile strength (622±19 MPa) and % elongation (21.3±1.4 %) were inferior. A high surface roughness was observed across at all processing conditions (> 5μm Ra). Finally, a study on corrosion performance was done. Two build orientations (parallel and

perpendicular to build direction) and as-built (no heat treatment) and annealed conditions were studied. Parts manufactured by SLM were characterized for corrosion properties in a 3.5% NaCl electrolyte and compared to results obtained for wrought DSS 2205. The measured corrosion rates from linear polarization resistance were < 1 μm/year for all conditions. The as-built conditions showed anisotropic corrosion rates due to the preferred crystallographic orientation of the different build orientations. The anisotropy was not replicated on the annealed conditions, possibly due to elemental segregation of Si and Mn, or porosities. A novel finding was that the as-built parallel condition showed superior performance to wrought (0.33±0.10 μm/year vs 0.59±0.10 μm/year corrosion rate). No steady state pitting behavior occurred during the cyclic polarization (CP) test for any conditions tested, although certain SLM conditions showed metastable pitting (up to 10-5 A/cm2 measured during CP), likely due to open surface pores. The exception was as-built, parallel to build direction, which showed no metastable pitting due to the strongly resistant [110] ferrite texture.

Selective Laser Melting of Duplex Stainless Steel 2205 for Seawater Applications: Microstructure, Mechanical Properties, and Corrosion Performance

by
Gregory Nigon

A THESIS

submitted to

Oregon State University

in partial fulfillment of
the requirements for the
degree of

Master of Science

Presented March 5, 2020
Commencement June 2020

Master of Science thesis of Gregory Nigon presented on March 5, 2020

APPROVED:

_____

Co-Major Professor, representing Materials Science

_____

Co-Major Professor, representing Materials Science

_____

Director of the Materials Science Program

_____

Dean of the Graduate School

I understand that my thesis will become part of the permanent collection of Oregon State University libraries. My signature below authorizes release of my thesis to any reader upon request.

_____

Gregory Nigon, Author

ACKNOWLEDGEMENTS

I express appreciation to my advisers Dr. Somayeh Pasebani and Dr. Burkan Isgor. Their guidance and professionalism made this thesis possible. Additionally, their teaching and expertise has given him many more skills and knowledge than when I started graduate school. I also express gratitude to the School of MIME and the various professors and instructors I worked with during my GTA appointment, especially Scott Campbell, Dr. Brian Paul, Dr. Karl Haapala, and Dr. Ali Tabei.

I thank my committee members, Dr. Megumi Kawasaki and Dr. Bo Sun, for taking the time to attend and evaluate my defense.

I thank Peter Eschbach and Teresa Sawyer for helping me complete my microscopy work, especially the EBSD data. I also thank Dr. Albrecht Jander for his time spent on magnetometer data collection and analysis.

I thank the facility staff at ATAMI for maintaining a wonderful facility and occasionally providing assistance in the lab.

I thank the various students I have worked with, especially Pratik, Milad, and Saereh, who generously spent their time training me on the various tools and experiments used in this thesis.

Finally, I thank Kate and my family for their continual support.

TABLE OF CONTENTS

Page

TABLE OF CONTENTS (Continued)

Page

TABLE OF CONTENTS (Continued)

Page

LIST OF FIGURES

Figure Page

LIST OF FIGURES (Continued)

Figure Page

LIST OF FIGURES (Continued)

Figure Page

LIST OF TABLES

Table Page

DEDICATION

I dedicate this thesis to Larry Nigon, a guinea pig, who passed away on a hot summer day.

“Dr. Hoenikker used to say that any scientist who couldn’t explain to an eight year old what he was doing was a charlatan.” Cat’s Cradle, Kurt Vonnegut Jr.

Chapter 1. Introduction

1.1 Background

Duplex stainless steels (DSS) are an important and versatile class of steel currently in use around the world. They have a dual phase microstructure, consisting of roughly equal proportions of ferrite and austenite [1]. They are notable in that they either match or improve on the corrosion properties of more traditional stainless steels (304, 316L) but have approximately twice the strength [2]. The resistance to pitting corrosion for duplex stainless steels tends to be superior to the traditional 300 series [3]. This is an effect of the chemical composition, most notably the chromium content [1]. The combination of high strength and good corrosion resistance makes duplex stainless steels notably resistant to stress corrosion cracking (SCC) [1]. Additionally, due to their high strength they can be cost competitive, as less material may be used [3]. While duplex stainless steel has been in use since the 1930s, investigators continue to search for ways to innovate, such as finding alternative manufacturing processes for specific components.

Additive manufacturing is a fast and growing field. In terms of processing it offers the advantage of enabling near net shape, complex designs [4]. Other potential advantages include reduced lead times, lightweighting, and individualization (such as medical implants) [5]. There are ongoing research efforts to expand the material library of additively manufactured materials. Stainless steels, including duplex stainless steel, are one such material of interest [6–8].

There has yet to be a report of an additively manufactured duplex stainless part that has been implemented commercially. However, certain developments suggest that this could be something which happens in the near future. For example, a paper has been published on the design of selectively laser melted pump impellers [9] as shown in Figure 1.1. The motivating factor of the paper was the design of small or complex impellers which are impossible or cost prohibitive to cast. The materials processed in the study were an unspecified grade of stainless steel, and Inconel 625. Duplex stainless steel is commonly used as a material for pump components in harsh seawater environments, such as in desalination plants [3].

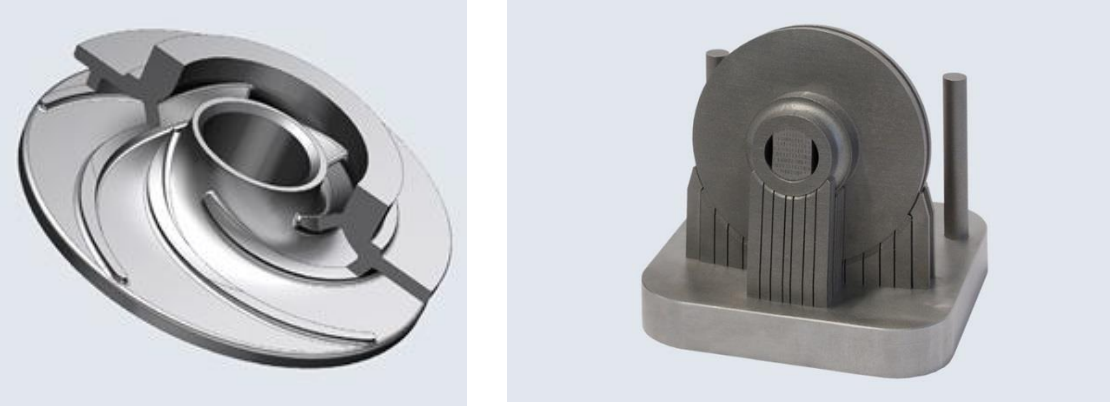

Figure 1.1. Pump impeller (a) design and (b) prototype made by selective laser melting. The material in picture is IN625 but the target material is stainless steel, and diameter is 92.4 mm [9]

The additive methodology studied in this thesis is selective laser melting (SLM), a laser powder bed fusion process. Other metal additive manufacturing methods include binder jetting, directed energy deposition (DED), electron beam melting (EBM), among others. Both SLM and EBM rapidly melt and solidify a metal powder feedstock to form a solid part [4]. As with all additive technologies, SLM is a layerwise process whereby a new layer of material is deposited over the previously solidified layer. The scanning path and the number of layers is dictated by a solid 3D model [4]. The difference between SLM and EBM is the heat source. EBM uses an electron beam whereas SLM uses a high-powered laser, such as ytterbium fiber.

Relative to other metal additive manufacturing methods, SLM offers key advantages. It does not require any binding material, which could reduce post processing time [10]. However, it is important to note that many metals, such as duplex stainless steel, often require a final annealing regardless of the processing route. Other advantages are the potential for high relative density [10] and the ability to reuse powder [4]. Over 99.9% dense parts have been printed [10]. Disadvantages include the use of expensive lasers, slow build times relative to DED, anisotropic properties, and high residual stresses [4,10].

The subsequent literature review will provide a broad introduction to duplex stainless steel, covering its chemistry, microstructure, mechanical properties, corrosion properties, and conventional processing. Challenges with conventional manufacturing will also be discussed. It will cover the related literature for SLM of duplex stainless steel. Finally, the specific objectives of the project will be discussed.

1.2 Objectives and Novelty

The overarching goal of this work is the evaluation of the SLM manufactured parts as functional parts for the seawater applications. Considering this objective and the literature review presented below an investigation into SLM of duplex stainless steel 2205 was done. The results of this investigation are compiled here in the form of two manuscripts.

The first manuscript is focused on the manufacturability, microstructure, texture, and mechanical properties. Identifying optimal SLM processing conditions is a novel topic that has yet to reach consensus, and it is important that the results from different researchers who are using different powders and tools is catalogued. The relationship between selected processing conditions, grain orientation, and texture is an area where deeper understanding is desired. Anisotropy of mechanical properties for additively manufactured parts is widely reported [11–13] and ultimately ties back to the processing. This work makes novel connections between the processing conditions and the resulting grain orientation and texture for duplex stainless steels. It also analyzes the effect of heat treatment on grain orientation. Another novelty of the work is a study of three different techniques for measuring the austenite-ferrite ratio after annealing. Besides microstructure and mechanical properties, there are overlooked properties such as chemical composition and surface roughness which have practical importance. Appropriate surface finishing takes time and energy and should be kept in mind. All these topics are covered in the first manuscript.

The second manuscript in this thesis is a novel, in depth corrosion investigation. The initial investigation on pitting behavior by Papula et al. [8] is limited and has some key issues. A comprehensive report on corrosion behavior occurs here and focuses on the effects of heat treatment and build orientation. The two factors connect well with the findings and discussion of the first manuscript. Additionally, the corrosion properties of the SLM manufactured components are compared to wrought duplex steel 2205. Taken collectively, this work confirms certain properties of SLM duplex stainless steel alloys, builds on prior work with additional characterization, introduces some results which challenge prior work, and recommends topics for future researchers. It is a helpful guide for those interested in implementing and studying SLM duplex stainless steels.

1.3 Literature Review

1.3.1 Bulk Chemistry

Duplex stainless steel may be characterized by the types and compositions of alloying elements. First and foremost is chromium. Chromium in excess of 12% allows for the formation of a passive film, and is the key component in any stainless steel [1]. It also acts as a ferrite stabilizer. Another ferrite stabilizer present is molybdenum [14]. The elements of Mn and Ni are crucial for stabilizing the austenite phase at room temperature, and thus need to be in the formulation as well [14]. A dual austenitic-ferritic structure is achieved in a steel with the right proportions of these four elements. Typical duplex stainless steels contain ~20-25 % Cr, ~0.05-5 % Mo, ~1-8 % Ni, and ~0-6 % Mn [2].

Another important alloying agent is nitrogen. Solution alloying with nitrogen was implemented to solve an industry problem in which the heat affected zone during welding would suffer a loss in toughness and corrosion resistance [15]. The reason cited was a loss of austenite, and even sometimes a full reversion to pure δ-ferrite [16]. It was found that by adding nitrogen to gas flow during decarburization, the steel could be doped with nitrogen [15]. The added nitrogen was found to stabilize the austenite during welding and retain the properties of the weldment [15]. Nitrogen also allows for lower usage of nickel (cost savings). It is typically used at ~0.05-0.34 % [2].

Copper may be added at ~0.5-3 % to improve corrosion resistance [2]. Elements such as silicon (0-1%) may be added to increase strength, although it is also considered an impurity. Other elements are also present as impurities. Sulphur in excess of 30 ppm causes severe cracking and reduced ductility during hot rolling while phosphorus up to 150 ppm has no effect [17].

1.3.2 Microstructure

The desired microstructure of DSS is unique in comparison to other stainless steels in that it is a mixture of ferrite α, and austenite, γ. It is the equilibrium microstructure over a specific range of concentration for chromium and nickel. It is defined as the region δ (ferrite) + γ (austenite) from the phase diagram shown in Figure 1.2.

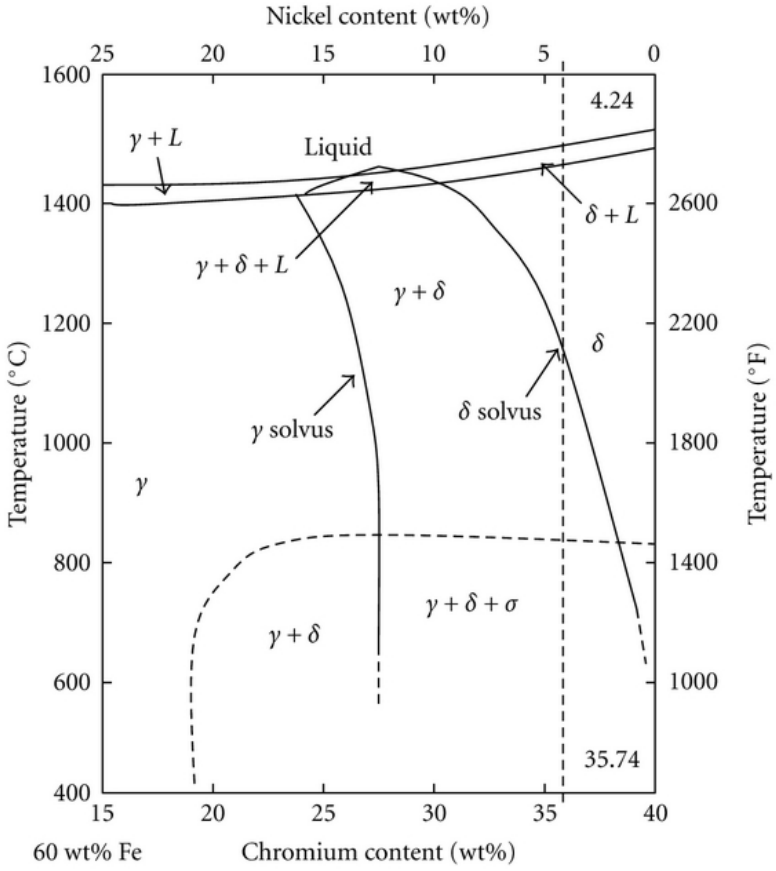

Figure 1.2. Fe-Cr-Ni phase diagram for a stainless steel with 60% Fe [18]

Austenite, or γ, is a face centered cubic (FCC) structure while ferrite, α/δ, is a body centered cubic (BCC) structure. To distinguish between δ-ferrite and α-ferrite one must first consider the typical Fe-C phase diagram. The δ-ferrite is the stable form of BCC-Fe or BCC-Fe-C (low C) at 1400-1535 ^{o}C [19]. The BCC α-ferrite is the stable from room temperature to 900^{o} C [19]. If the BCC-Fe forms as a result of a slow cooling process in which the FCC γ forms and then transforms to BCC through a diffusion process, it is termed α-ferrite [20]. If the BCC Fe forms from a rapid solidification process (such as in laser melting) in which γ is never an stable phase, it is termed δ-ferrite [20]. The δ and α phases have the same BCC structure, and only behave differently when iron content is > 90% [1]. This does not apply to stainless steels. Determining whether the ferrite in duplex stainless steel is δ or α is difficult. Unlike typical steel, in stainless steel the dual phases can coexist from low temperature up to the melt, as shown in Figure 1.2. In accordance with Figure 1.2, all ferrite for duplex stainless steel in this paper will be termed δ-ferrite. Because SLM

manufactured parts are cooled rapidly from the melt (> 10^6 ºC/s [21]), so it is generally accepted that any BCC Fe is δ-ferrite.

There is a gap in the literature about specifying the exact fractions of austenite and ferrite to constitute a duplex microstructure, but authors have reported expected duplex properties from as low as 30% ferrite [1] to as high as 80% ferrite [22]. The specification per ASTM A890 for duplex stainless steel castings is 30-60% ferrite [23]. When cooled from the melt the microstructure manifests as islands of austenite within a base ferrite phase [15]. The lighter sections are the austenite islands as shown in Figure 1.3.

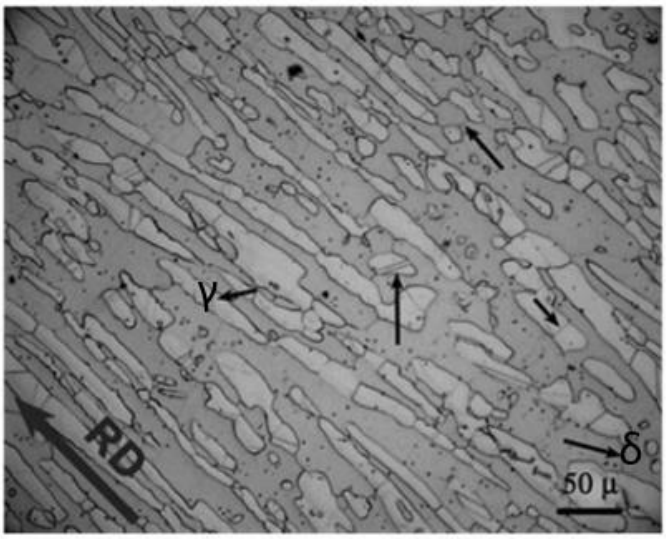

Figure 1.3. Microstructure of hot rolled duplex stainless steel 2205 [24]

Other phases beyond austenite and ferrite may form in DSS which are detrimental to the performance. These include σ, $\acute{\alpha}$, χ, chromium nitride (Cr_2N, CrN), and various metal carbides ($M_{23}C_6$, M_7C_3) [1]. The σ phase is Cr-rich phase and preferably forms at the boundary between austenite and ferrite. It is the most deleterious phase [25]. It precipitates out between 700 and 900 ºC in as little as 10 minutes [25] as shown in Figure 1.4.

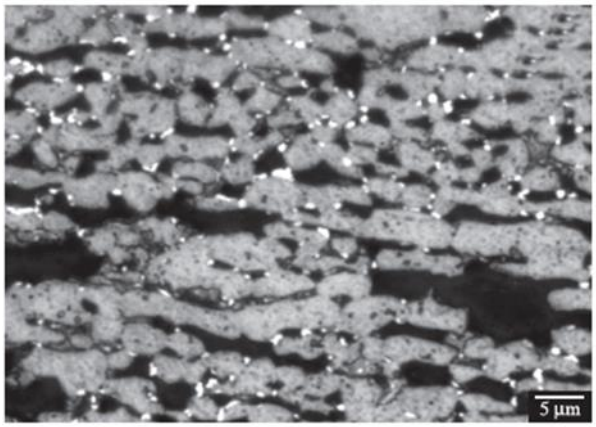

Figure 1.4. Sigma phase (bright white) precipitating at austenite-ferrite grain boundaries [25]

The dominant mechanism for sigma phase, σ, formation is nucleation from the ferrite phase, originating at the grain boundaries. The growth rate of the sigma phase is dependent on the diffusion of chromium from ferrite to the grain boundary. In the range of 700-850 ^{o}C σ. phase nucleates at ferrite-austenite grain boundaries and grows through thermally activated diffusion mechanism [25]. Above 900 ^{o}C σ phase is no longer a thermodynamically stable for most duplex alloys [1]. The precipitation and growth of sigma coincides with consumption of ferrite. Over extended periods of time (~100 hours) the ferrite may be completely consumed [25].

Alpha prime ($\acute{\alpha}$) is another common precipitate phase. It is Cr-rich and shares the same crystal structure as the ferrite (BCC) [1]. The common industry term for this phase is 475 ^{o}C embrittlement, a reference to its formation temperature. The real temperature range of formation is ~300 ^{o}C [14] to 525 ^{o}C [1]. It has been shown that $\acute{\alpha}$ forms by a spinodal decomposition of ferrite into iron-rich and chromium-rich phases [1]. The kinetics for $\acute{\alpha}$ are much slower than σ (10's, 100's, or even 1000's of hours for embrittlement to set in, depending on temperature) which means it is not much of a concern in processing [1]. However, it restricts the use of duplex to temperatures less than 300 ^{o}C.

Many other precipitates may form in duplex steels. In high nitrogen steels the precipitation of chromium nitride can occur during welding operations if the weld is cooled too rapidly due to nitrogen oversaturation in the ferrite, or more generally, it may precipitate in wrought duplex if the cooling rate is too slow through the range of 600-900^{o}C [15]. Chi, χ, an ordered cubic phase with composition $Fe_{36}Cr_{12}Mo_{10}$ forms at temperatures of 600-700 ^{o}C, and various iron carbides ($M_{23}C_6$, M_7C_3) form at 850-1050 ^{o}C [1]. If

secondary phases are present in the material they will lead to embrittlement, loss of toughness, and lower corrosion resistance [14]. For samples without the desired microstructure, a full solution anneal is often conducted at temperatures >1050 ^{o}C. The cooling rate post anneal must be sufficiently fast to avoid precipitation of σ phase, hence water quench is preferred [7].

1.3.3 Mechanical Properties

Duplex stainless steels have ~2-3X the yield strength of standard stainless steels, both ferritic and austenitic steels [1]. It has significantly higher tensile strength than traditional stainless steels such as 304L and 316L [2]. The tradeoff is that DSS are not as ductile as the austenitic family. The percent elongation of DSS 2205 is typically 25% [23] whereas both 316L and 304 have an elongation of 40% [2]. The specific grade of material under study in this thesis is DSS 2205. The allowable mechanical properties of DSS 2205 per ASTM A790/A890 is shown in Table 1.1. ASTM A790 is for welded pipe and ASTM A890 is for castings [23,26].

Table 1.1. ASTM specifications on mechanical properties for duplex stainless steel 2205 [23,26]

Specification	**Microhardness (HV)**	**Yield Strength (MPa)**	**Tensile Strength (MPa)**	**Elongation (%)**
ASTM A790 (A890)	293 MAX	450 (448)	620 (620)	25 (25)

Within the family of DSS there is still a wide variety of mechanical properties. Type 2304 is a weaker type (yield strength of 400 MPA) whereas the super duplex types like 2507 are stronger (yield strength of 550 MPa) [2]. The lower elongation means that the austenitic stainless steels are easier to machine and form in the factory. The difficulty in applying forming processes to DSS makes SLM an attractive alternative as it is near net shape processes. Despite these drawbacks, the main reason why austenitic brands dominate the market is still economical. They are usually sold at slightly lower cost and their stocking and availability has historically been superior [27].

Early literature on mechanical properties of DSS reported that it follows a rule of mixtures, meaning the mechanical properties would fall between austenitic and ferritic grades [1]. This is not the case. A smaller grain size is typically obtained in dual austenite-

ferrite microstructure which is not easily obtained in single phase steels, resulting in superior mechanical properties [28]. The duplex steels have been found to follow the Hall-Petch relationship [1].

1.3.4 Corrosion Properties

Steels containing >12 wt. % chromium, known as stainless steels, form a stable passive film and are resistant to corrosion in nearly all aerated solutions [29]. More specifically, they are resistant to general corrosion, which is uniform and continuous removal of material [29]. Duplex stainless steel 2205, with 22 wt. % Cr, is no exception. For stainless steels, the passive film is known to contain an inner barrier layer that is rich in Cr_2O_3, CrO_3, Fe_2O_3, and FeO and an outer layer that is rich in $Cr(OH)_3$ and FeO(OH) [30]. Molybdenum and manganese are also present in the film as oxides, and it is known that molybdenum reduces the concentration of chlorides in the oxide layer and thus strengthens the passive film [30]. A recent study on duplex stainless steel 2205 confirmed the presence of the aforementioned Cr and Fe oxides, although the relative amounts of each species depended on the potential applied to the surface [31].

Despite having excellent resistance to general corrosion, stainless steels are susceptible to pitting and crevice corrosion. Pitting and crevice corrosion are localized, rapid attacks. Pitting occurs on the surface of the metal whereas crevice corrosion occurs in tight gaps formed by deposits or joined surfaces. The mechanism driving both forms of corrosion is the differential aeration cell. A differential aeration cell occurs when there is a gradient in oxygen concentration at the surface, resulting in preferential corrosion where oxygen concentration is poor [29]. As a result of the preferential corrosion in the pit or crevice, and with the presence of chlorides, acidification occurs which further drives the reaction. A schematic of this process is shown in Figure 1.5, along with examples of pits (arrows) in lean duplex stainless steel.

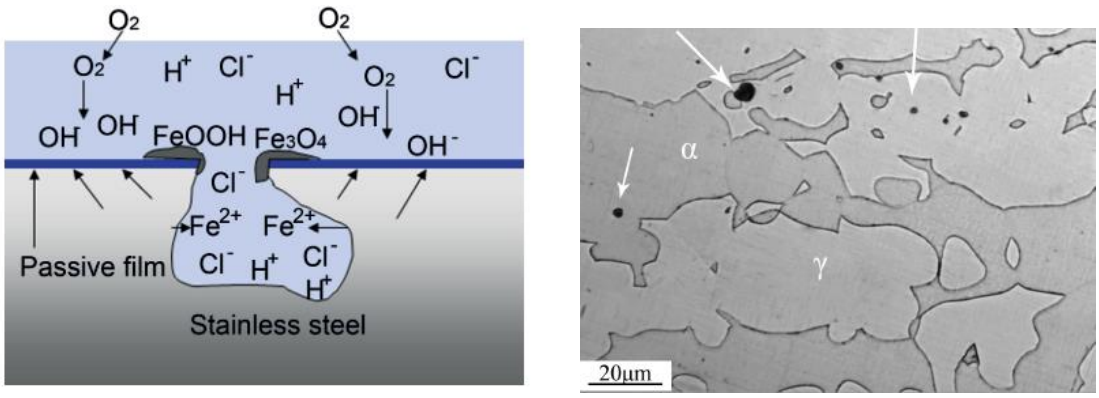

(a) (b)

Figure 1.5. (a) Schematic of pitting corrosion on stainless steel [30] and (b) micrographs of pitting attack in lean 2101 duplex stainless steel [32]

For crevice corrosion, the formation of the differential aeration cell is obvious, as there are tight gaps which inhibit oxygen transport. For pitting, the initiation is less clear. Pitting corrosion in 300 series initiates preferentially at MnS inclusions [29]. Dissolution of the precipitates may form microcrevices, or they may form a microgalvanic couple with the steel [29]. Initiation of pitting in duplex stainless steels may occur at high sulfur content grain boundaries, oxide/sulfide inclusions, or at the Cr depleted regions nearby high Cr precipitate phases such as σ phase or $\acute{\alpha}$ [1]. As discussed earlier, these precipitate phases are prevented by an appropriate heat treatment. Relative to the 300 series, duplex stainless steels have excellent resistance localized forms of corrosion [33]. One characteristic for predicting resistance to pitting and crevice corrosion is the chemistry of the steel. A formula for rating steels is used and is called the Pitting Resistance Equivalent Number (PREN):

$$\text{PREN} = \%\text{Cr} + 3.3(\%\text{Mo}) + 16(\%\text{N}) \text{ (wt. \%) [34]} \quad (1)$$

The determination of this relationship comes from linear regressions of extensive empirical data and can be used as a good guide for ranking stainless steels in terms of corrosion performance. What this equation says at a basic level is that the resistance to pitting is largely dependent on the chromium, molybdenum, and nitrogen content. As discussed earlier, this ties to the strength of the passive film. The PREN of duplex stainless steels falls between 25 and 40 depending on the grade. For contrast, 316 falls between 24 and 28 [35]. It should be noted that the PREN can be an oversimplification. For example, alloying agents such Ni are also known to improve pitting resistance [30].

Many early implementations of DSS were due to its superior resistance to chloride stress corrosion cracking (SCC) [15]. The conditions which cause SCC are a corrosive environment coupled with a tensile stress [36]. This can be either applied stress, like a load bearing part, or residual stresses that result from prior working and forming the material. During SCC, a crack initiates and propagates normal to the applied load, causing a brittle failure [29]. DSS has consistently been shown to have superior SCC resistance than austenite 300 series in chloride environments (seawater, NaCl, boiling $MgCl_2$) [1] [37].

Explanations for the superiority of DSS for SCC vary in the literature. Some suggest a galvanic protection mechanism of ferrite to austenite, while others believe microscopic changes in composition or stress distribution due to the dual microstructure are the key [37]. More recent sources cite factors such as higher yield stress (lower likelihood of plastic deformation) and small grain size (resist crack growth) [34]. Some important context is that certain grades of austenitic stainless steel, known as super-austenitic, match or improve on the resistance compared with DSS due to their high nickel and molybdenum contents [38]. Additionally, in certain environments DSS is not superior to, and is sometimes worse than 300 series alloys. Factors which degraded the resistance to SCC are high temperature, low pH, and the presence of H_2S [1].

As mentioned earlier, secondary phases are detrimental to the corrosion resistance of duplex stainless steels. The reason is that precipitated phases such as σ phase or $\acute{\alpha}$ are Cr-rich, leaving behind Cr-poor areas. These chromium depleted areas are susceptible to selective corrosion attack [39]. This is supported by decades of post failure inspection in the field, as well as bench top laboratory tests. A literature search of documented failures of DSS parts found that nearly 50% of all failures coincided with precipitation of undesired phases, especially sigma phase [40]. Figure 1.6 shows the effect of σ phase on corrosion rate in the Huey test (boiling 60% sulfuric acid).

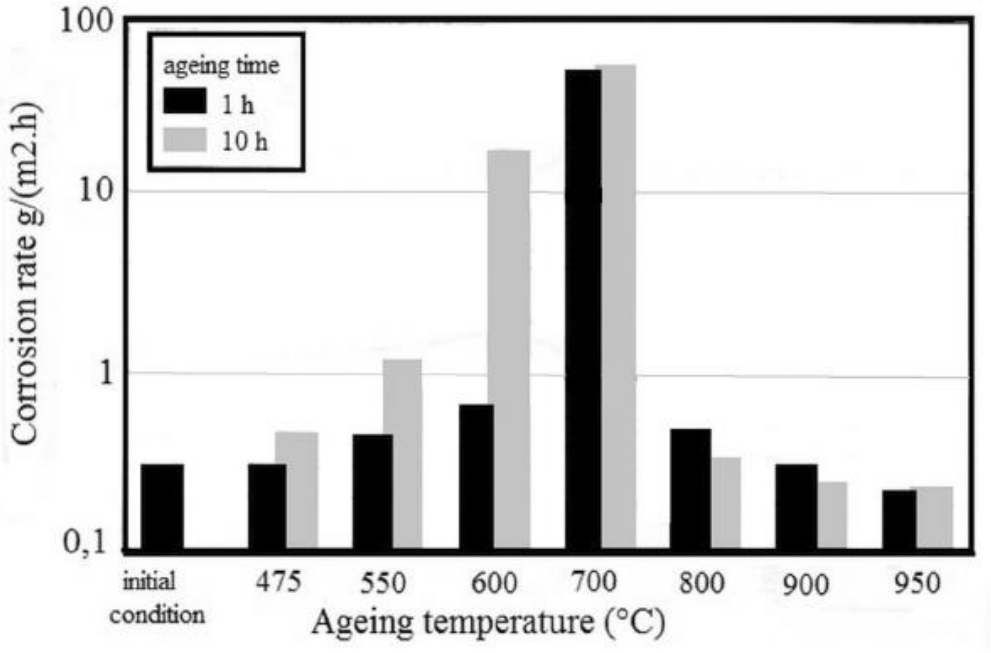

Figure 1.6. Effect of aging temperature and time (precipitation of sigma) on corrosion rates of duplex stainless steel [40]

The condition of the surface for stainless steels affects the corrosion properties, most notably the resistance to pitting [41]. It has been shown that rougher surfaces increase the susceptibility of wrought duplex stainless steel to pitting due to higher exposed surface area, presence of surface occlusions, and higher number of sites of pitting initiation [41]. The surface finish of SLM alloys tends to be undesirable [4], and must be characterized.

1.3.5 Conventional Manufacturing

Duplex stainless steel can be manufactured by conventional methods such as casting, forging, rolling, forming, and welding. The only challenges associated with rolling and forming DSS are due to its high strength. These limitations mean that for products which require several complicated forming procedures, like sinks, DSS is not the best option [14]. One way to make the forming process easier is by doing hot forming. DSS offers excellent hot forming at temperatures up to 1100 °C [15]. Warm forming at temperatures of ~300 °C is also a common practice. These forming operations must be followed up by a full solution anneal and quench to get rid of any possible secondary phases that may have formed during the process.

Cold forming is challenging due to the high strength and tendency to springback. Furthermore, when undergoing bending DSS will work harden, and resist the operation to a higher degree than austenitic steel [15]. There are several mechanisms which explain this behavior. First, the grain sizes of dual phase structures tend to be smaller than single phase, and the δ/γ phase boundaries impedes dislocation motion more than γ/γ (310 vs 225 MPa*μm^2, Hall-Petch type coefficient)[42]. Additionally, local plastic strain gradients near the phase boundaries tend to produce geometrically necessary dislocations[42]. Certain types of more complicated forming like spinforming and press forming may require intermediate annealing steps to bring back the ductility [15].

Duplex stainless steels are relatively simple to manufacture via static or centrifugal casting [43]. The microstructure of cast parts is known to be a dual austenitic-ferritic structure, but often comes with additional inclusions or phases. Most notably, a high concentration of fine precipitates accumulates along the austenite-ferrite grain boundaries which must be dissolved with a subsequent solution anneal [43]. Inclusions also form but generally do not dissolve away. The reason for their formation is the fast cooling rate which does not give enough time for the equilibrium microstructure to stabilize [43]. As-cast parts with no solution annealing showed greater penetration of intergranular corrosion than the as-cast solution annealed part [43]. With the standard solution anneal, the properties of the cast can be restored and are comparable to wrought specifications [44]. ASTM A890 requires that all casted parts with corrosion applications undergo the heat treatment [23]. Various versions of the heat treatment are specified for different situations, but in general it consists of a minimum temperature in the range of 1010-1130^o C, a holding time of 15 minutes or greater (60 minutes is common), followed by a water quench [23].

There are some issues with casting that cannot be overcome by solution annealing. Processing defects exist for cast parts. The most common type of defect is the shrinkage void, which results from local variations in cooling rate. Isolated melt spots form which form a void when they solidify (due to shrinkage). It is thought that these defects act as sites for crack propagation, so factors of safety are often designed to account for them [45]. Additionally, thin walled structures can be very difficult to cast, as the induced thermal stress results in cracking and deformation [46].

Over the years welding procedures have been optimized for duplex stainless steels. In the past welds have frequently suffered from poor phase balance and precipitation of unwanted phases which affect the corrosion performance and mechanical properties [47]. If the cooling rate from the melt is too high, austenite will not reform, and if the cooling rate is too low, secondary phases will grow [48]. However, using Ni-enriched fillers and nitrogen atmosphere can prevent most of these problems [47]. Still, the process will occasionally yield defects. If the cooling rate is too fast, Cr_2N will precipitate along with secondary γ [49] as shown in Figure 1.7. One study showed precipitation of Cr_2N when cooling rate was >40°C/s [50].

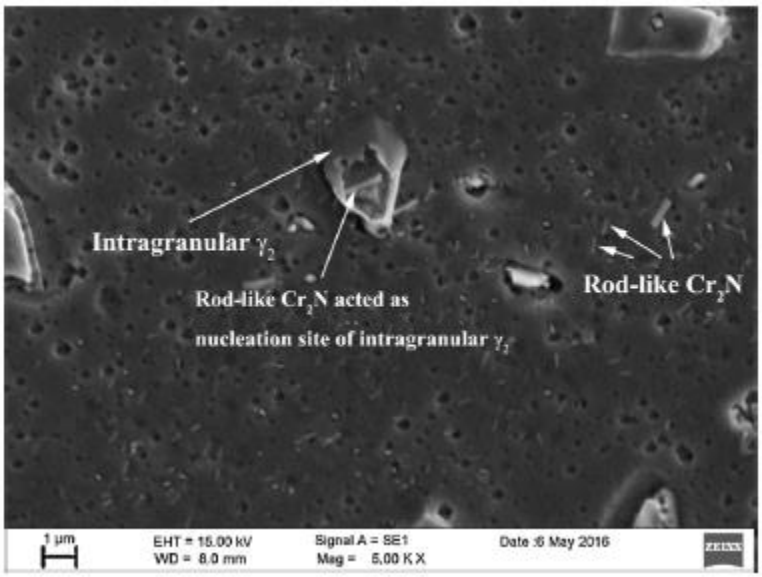

Figure 1.7. TEM micrograph of Cr_2N and secondary γ precipitates in duplex stainless steel welding [51]

Duplex stainless steel may also be processed via the powder metallurgy route. Utrilla et. al [46] studied the properties of duplex stainless steel obtained by mixing 316L and 434L powders. After mixing the powders were pressed at 700 MPa and sintered at 1250 °C [52]. While the basic microstructure was achieved (46% ferrite), the sample had a high porosity (15%). This resulted in poor corrosion performance. Pores consume O_2 (g) faster than can be replenished, so the passive film may not form [52]. Another explanation could be that a differential oxygen cell was created with the pore acting as the anode.

Dobranski et. al [53] obtained porosities as low as 7.34% with equal mixtures of 316L and 430L. This could have been due to the higher compaction pressure of 800 MPa. The σ phase precipitated for the slow cooled samples, but not for water quenched [53].

Finally, samples with equally mixed powders achieved UTS of up to 650 MPa but ductility of only 10% [53] due to the porosity. Clearly, there is much improvement that can be obtained for manufacturing duplex stainless steel through powder methodologies.

This review of traditional manufacturing brings potential applications for SLM duplex stainless steel into focus. The main opportunity is as an alternative to casting for thin walled structures such as in pump impellers which are difficult or impossible to cast [9]. Duplex stainless steel pump components, such as impellers, find use in the desalination industry (generation of fresh water from seawater for drinking) [3]. Highly complex components may also require many forming steps, so SLM may help to save time by printing the part in one shot. Finally, implementation of an SLM part which eliminates the need for welding and joining would be beneficial to avoid crevice corrosion.

1.3.6 Selective Laser Melting of Duplex Stainless Steel

The selective laser melting of duplex stainless steel from powder feedstock is a new area of research. There are only a handful of papers which have come out very recently once this thesis was started. Davidson et al [6] printed a super duplex stainless steel 2507. Optimization of parameters was done by fixing all parameters except laser power. Instead of an austenitic-ferritic microstructure, a nearly pure ferritic microstructure was observed after SLM due to the high cooling rates [6]. After full solution annealing the equilibrium microstructure was recovered (45% austenite), although the morphology of the austenite was “needle-like” [6]. The densities achieved were 85-90% [6].

In a follow up paper Davidson et.al [54] ran a matrix skew of laser power and laser volumetric energy densities (VED) to better understand the process-microstructure relationship. The volumetric energy density, E, (J/mm^3) is a common parameter studied when selective laser melting, however cannot capture the complex physics during SLM process [55]:

$$E = \frac{P}{vht} \tag{2}$$

In equation 1 P is power (W), ν is scan speed (mm/s), h is scan line spacing or hatch spacing (mm), and t is powder layer thickness (mm).

An interesting finding of Davidson et.al [54] was that the SLM processed duplex stainless steel showed white, spherical precipitates in the microstructure. Davidson et al.

[54] proposed these precipitates to be CrN, which can form under conditions of high temperature (>1273 K) and fast cooling rates (>20K/s). The authors hypothesized these precipitates would decrease ductility and increase pitting corrosion rates. Another interesting result was the hardness of 408.4 HV, which was 125.9 HV higher than their wrought measurement. The CrN precipitates may explain this high hardness, although the microstructure could also be the reason. The studied samples were predominantly ferrite and the grains were elongated and columnar (average length ~370 µm, average width ~35 µm) as shown in Figure 1.8 [54].

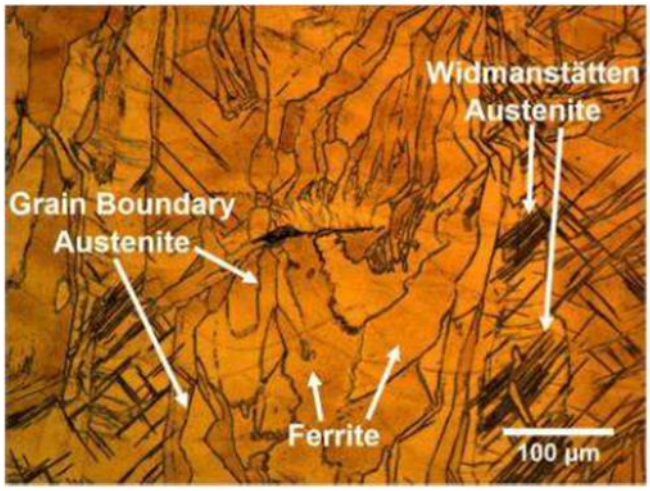

Figure 1.8. Microstructure of as-built duplex stainless steel 2507 [54]

Hengsbach et. al. [7] manufactured SLM samples with 99% ferrite and densities >99% [7]. This density is a significant improvement over the prior work and is likely due to proper selection of processing parameters (275W, 775 mm/s scan speed, and energy density 59 J/mm^3). According to Hengsbach et al. [7] the expected mechanical properties of DSS can be recovered after heat treatment as shown in Figure 1.9. They showed that as-built samples were brittle with high dislocation densities and presence of nitrides, but heat treatment of 900-1200 °C restored the ductility and toughness [7]. They explained the result in light of the recovery of the duplex microstructure (up to 34% austenite) [7].

Another very recent study was done by Papula et al. [8]. They also found that the as-built parts were fully ferritic, hard, and brittle, but that solution annealing restored the duplex microstructure (up to 46.4% austenite recovered) [8]. A notably high relative density of 99.97% was claimed and supported by an ultimate tensile strength of > 800 MPa

and elongation >40% [8]. The elongation is surprising as wrought specifications typically list 25%. Papula et al. [8] recommended high power (>250W) and a 67^{o} scan rotation strategy for obtaining maximum density. Initial studies on pitting corrosion suggested the as-built condition was susceptible to pitting while the annealed condition was not [8].

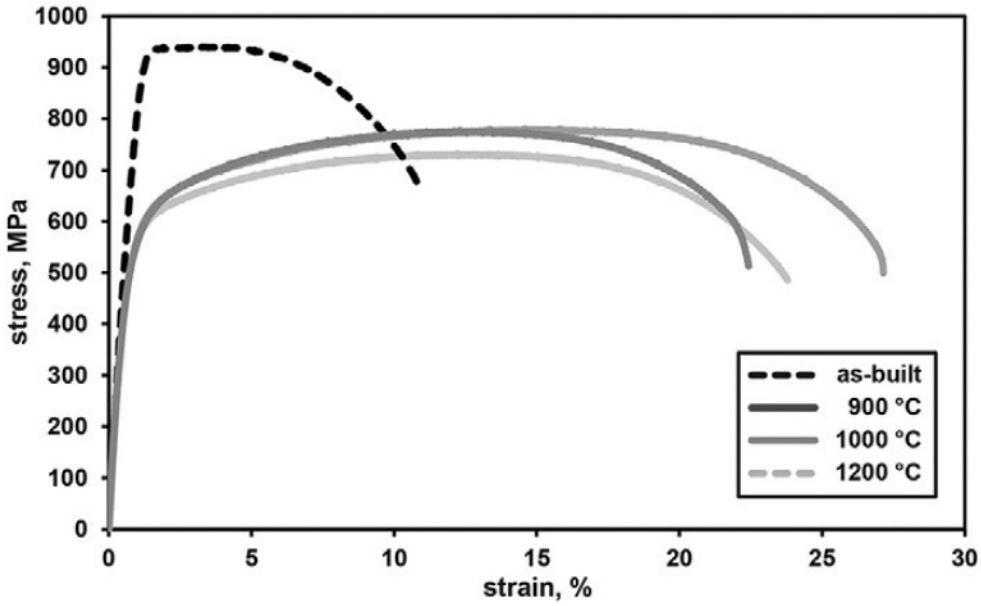

Figure 1.9. Recovery of mechanical properties for SLM manufactured duplex stainless steel 2205 by heat treatment [7]

There are several knowledge gaps in SLM of duplex stainless steel in light of the literature review. First and foremost is corrosion behavior. The prior work on this subject in limited and has key issues. Secondly, strong correlations between processing, grain orientation, and properties (mechanical and corrosion) have not been identified. Measurements and methods to study phase balance have been limited. Finally, important manufacturing challenges, such as chemical composition and surface roughness have not been analyzed in depth.

Chapter 2. Selective Laser Melting and Annealing of Duplex Stainless Steel 2205: Phase Balance, Grain Orientation, and Manufacturing Challenges

Greg N. Nigon [a,c], O. Burkan Isgor [b,c], and Somayeh Pasebani [a,c,1]

[a] School of Mechanical, Industrial and Manufacturing Engineering, Oregon State University, Corvallis, OR, 97330

[b] School of Civil and Construction Engineering, Oregon State University, Corvallis, OR, 97330

[c] Advanced Technology and Manufacturing Institute (ATAMI), Corvallis, OR 97330

2.1 Abstract

Duplex stainless steel 2205 components were built using gas atomized powder ((D_{90} <45μm) via selective laser melting with a 250 W laser and nitrogen environment. Maximum relative density was 99.1±0.3%. Annealing restored the duplex microstructure. A comparison of electron backscatter diffraction, optical microscopy, and magnetometer phase analysis techniques was done yielding ferrite contents of 51.7±0.7 %, 53.0±4.8 %, and 55.7±1.0 %, respectively. The grain orientation was influenced by the layerwise building and scan strategy. The as-built and annealed ferrite grains showed [001] texture. The austenite had mixed orientation. The measured microhardness of 258±8 HV compared to wrought, but the ultimate tensile strength (622±19 MPa) and % elongation (21.3±1.4 %) were inferior. Manufacturing challenges of process optimization, obtaining expected chemical composition, and surface roughness were investigated. Expected composition was achieved, but segregation of Cr was observed in as-built components, and Si/Mn in annealed components. Surface roughness was > 5 μm across processing conditions.

Keywords: SLM; Duplex Stainless Steel 2205; Processing; Microstructure; Grain Orientation

[1] Corresponding author (Somayeh Pasebani): e-mail: somayeh.pasebani@oregonstate.edu; phone: +1-541-737-3685

2.2 Introduction

Duplex stainless steels (DSS) are notable in that they either match or improve on the corrosion properties of more traditional austenitic stainless steels (304, 316L) but have approximately twice the strength as discussed by [1]. This is achieved by a unique microstructure which consists of roughly equal proportions of ferrite and austenite phases. The combination of strength (from ferrite) and corrosion resistance (from austenite) makes it attractive for applications where resistance to stress corrosion cracking (SCC) is critical. The grade of DSS investigated here is 2205 with composition of Fe-22Cr-5Ni-3Mo-1Mn (wt.%) and is one of the most widely used duplex grades in various applications.

The main limitation in using DSS is the precipitation of deleterious secondary phases such as sigma (σ), alpha prime (α'), chromium nitride, chi (χ), and metal carbides (M_7C_6 or $M_{23}C_6$) [1] in certain temperature ranges. At temperatures between 700 -900 °C, the Cr-rich sigma phase (σ) forms by diffusion of chromium from the enriched ferrite phase to the grain boundary between austenite and ferrite in approximately 10 minutes. Over extended periods (~100 hours) ferrite may be completely consumed by the σ phase [25]. Another Cr-rich phase is α' that forms from ~300 to 525 °C through a spinodal decomposition of ferrite into iron-rich and chromium-rich BCC phases [1]. However, the kinetics for α' are much slower than σ; therefore, it is not of concern during conventional processing such as hot forming [1]. The precipitation of chromium nitride can occur in the ferrite phase during welding operations of high nitrogen steels [56]. The chi (χ) phase, an ordered cubic phase with composition $Fe_{36}Cr_{12}Mo_{10}$ forms at 600-700 °C, and metal carbides such as M_7C_6 and $M_{23}C_6$ form at 850-1050 °C [1]. These unwanted phases introduce brittleness and chromium depletion sites to the metal, and negatively impact both mechanical and corrosion performance. The amount of chromium segregation combined with the width of the grain boundary area (where segregation occurs) would have a significant impact on the corrosion properties of DSS [1].

Duplex stainless steels are successfully manufactured using conventional methods such as casting and forging. Other processing techniques such as rolling, forming, and welding have also been implemented with success. Occasionally undesired microstructures result from casting or forming, and a solution annealing heat treatment is necessary for recovery [15]. Welding can also result in poor phase balance and precipitation of undesired

phases, but is usually overcome by using a Ni-enriched filler metal and nitrogen shielding gas as well as careful control over heat input and weld time. If the weld is cooled too rapidly under nitrogen gas, chromium nitrides may precipitate [49].

One type of powder bed-based additive manufacturing is selective laser melting (SLM), a field which is growing rapidly. For example, SLM has been investigated as a method of producing pump impellers whose designs are impossible to manufacture via casting [9]. Impellers made from duplex stainless steel find use in the desalination industry [57]. SLM of DSS could also be used for on demand replacement parts in marine and naval applications.

Work is well underway on SLM of duplex stainless steels [6–8]. Formative work on super duplex 2507 identified that parts made by SLM have a fully ferritic, rather than duplex microstructure, and contain residual porosity [6]. Further work by Hengsbach *et al.* [7] showed that the fully ferritic as-built microstructures of duplex 2205 contained chromium nitrides, similar to rapidly cooled welds, and were strong yet brittle. Additionally, it was shown that solution annealing heat treatments could restore both the duplex microstructure (up to 34% recovered austenite) and the strong and ductile mechanical properties [7]. Very recently, a comprehensive work on SLM DSS 2205 confirmed this behavior, but achieved a notably high relative density of 99.97%, with up to 46% recovered austenite, and improved strength and ductility over the wrought counterparts. The factors which contributed to the high density were the processing parameters (power of 250W, scan speed of 850 mm/s, and low volumetric energy density of 59 J/mm^3), and implementation of a 66^o scan rotation strategy [8]. Preliminary work was also conducted on understanding the crystallographic texture and corrosion properties of the DSS parts built by SLM [8].

The aim of this work is to fill certain key learning gaps for producing DSS 2205 by SLM. There are three novelties of this work. One is the comparative analysis of three phase balance measuring techniques. Another is an analysis of the effect of layerwise building laser scan strategy on the grain orientation, as well as the effect of the heat treatment on grain orientation, specifically for duplex stainless steel. The third is a comprehensive study of specific manufacturing challenges of selectively laser melted duplex stainless steel 2205,

such as surface roughness, obtaining appropriate chemical composition, and process optimization.

For both DSS 2507 and 2205 SLM parts, it has been shown that the heat treatment restores the duplex microstructure, with austenite recrystallizing in proportions up to 45% [6–8]. Different methods can be used to determine phase content, such as optical microscopy (OM), EBSD, and magnetometer. However, a good comparison of these three phase content measuring methods for SLM of duplex is lacking. This is another aim of this research.

SLM parts have been widely reported to have preferred grain orientation due to the thermal gradients and resulting directional solidification during the layer by layer build [8,58]. The layer by layer build also results in highly anisotropic properties and strong [001] textures for SLM parts [12]. A goal of this research is to directly tie the layerwise nature of SLM, along with the scan strategy, to the grain orientation and crystallographic structure of both the ferrite and austenite. The effect of the heat treatment will also be shown.

The condition of the surface effects the corrosion properties [59]; therefore, careful attention must be placed on surface roughness for additive manufacturing (i.e. SLM) of duplex stainless steel as the process is known to frequently produce undesirable surfaces. Researchers have found that the increasing SLM roughness produces higher corrosion rates for aluminum alloys [60]. To date, the surface roughness of SLM DSS 2205 has not been characterized. This is important, as it will inform engineers on the types of finishing processes that are necessary in different applications.

The final goal is to do a comprehensive study on chemical composition. The chemical composition of the steel is important and could be altered during SLM. Studies have shown that vaporization of elements such as Cr may occur, affecting the final composition of the alloy [61]. This is important when considering resistance to pitting corrosion, which generally improves as the concentration of key elements, such as Cr, Mo, and N, increases [29]. Additionally, large changes in chemical composition will result in an undesired phase balance which is detrimental to mechanical properties due to grain size effects because Cr and Mo stabilize ferrite while Ni, Mn and N stabilize austenite [1].

In summary, this paper addresses the key learning gaps in SLM DSS 2205 with a novel approach to obtain and measure phase balance, correlate scan strategy with grain orientation and size, and analyze surface roughness and chemical composition of the built components. Results are also reported on the optimization of laser processing parameters to achieve maximum relative density and the resultant mechanical properties.

2.3 Experimental Methods

2.3.1 SLM, Relative Density, Surface Roughness

Gas-atomized DSS 2205 powder and wrought DSS sheet were procured from Carpenter Inc. and Langley Alloys, respectively. The chemical composition of both DSS powder and wrought are shown in Table 2.1.

Table 2.1. Chemical composition of duplex 2205 stainless steel powder and wrought duplex

Alloys	**Elements (wt.%)**								
	C	**Mn**	**Si**	**Cr**	**P**	**Ni**	**Mo**	**N**	**Fe**
2205 powder	0.018	1.08	0.68	22.2	0.015	5.4	2.97	0.18	Balance
2205 Wrought	0.015	1.41	0.40	22.3	0.019	5.7	3.19	0.179	Balance

The apparent density and tapped density were measured in accordance with ASTM B212 and ASTM B527, respectively. The ratio of tapped density to apparent density was calculated as the Hausner Ratio. The particle size distribution was measured with a Malvern Mastersizer 3000, a tool using liquid dispersion and a laser [62]. The dispersion unit operated at 2400 RPM and sonication was set to 80% for the duration of the test. The measurement was recorded at ~1-2% obscuration. Duplex stainless steel 2205 powder morphology was characterized using an FEI Quanta 600F scanning electron microscope (SEM).

SLM parametric optimization was done on an ORLAS Laser Creator SLM machine. All variables were fixed except for power and scan speed. Different combinations of power and scan speed were used to print samples over a range of 107-207 W and 200-1000 mm/s, respectively. This was completed in two rounds of printing, with 9 cylinders printed each time. The fixed parameters are shown in Table 2.2.

Table 2.2. Fixed parameters for initial process skew

Parameter	Value	Parameter	Value
Layer height	30 µm	Coater Speed	27%
Line thickness	50 µm	Powder Feed Rate	230%
Oxygen content	0.01%	Temperature	22 min. 32 max (°C)
Nitrogen gas Flow	35%	Samples	8X8 mm cylinders

All printed samples were characterized for relative density and surface roughness. Density was measured using the Archimedes method and relative density was calculated by comparing to a wrought sample with a measured density of 7.79 g/cm^3. Surface roughness was characterized with a Mitutoyo SJ-210 surface profilometer. All measurements were done on a black granite surface plate with flatness tolerance of 0.000075". The condition selected for further analysis was processed at 187 W and 800 mm/s.

2.3.2 Heat treatment, Microstructure, and Phase Analysis

The solution heat treatment in this study was done at 1100 °C for 1hr in air atmosphere followed by water quenching. This is the specified heat treatment on the wrought sample used as a comparison in this study. Phase determination was done using a Bruker D8 discover X-ray diffraction (XRD) from $2\theta = 30°$ to $2\theta = 90°$ with 3°/minute and increment of 0.03°. Magnetic saturation moments were measured with a SQUID magnetometer. The scan range was -1.2 -1.2 T. The magnetic moment was collected as one way to estimate the ferrite content in the sample.

Sample preparation for microscopy included cutting, mounting, polishing and electrochemical etching. Samples were cut with a diamond precision cutting saw. Hot mounting was done using phenolic resin at 200°C. The polishing sequence was 240, 400, 600, 800, and 1200 grit SiC paper followed by 0.05 µm alumina polishing suspension liquid. The as-built samples were etched in 10 vol.% oxalic acid at 6V for 2 mins. For heat treated samples etching was done in 40vol.% KOH solution at 3V for 2-6s. Electron back scatter diffraction (EBSD) was done with an FEI Quanta 3D dual beam equipped with EBSD system. The operating voltage and current were 20kV and 1.7 nA, respectively. The

scan was conducted at 1000X magnification with 1 μm step size. Samples were prepared for EBSD using the same polishing sequence as OM, with additional finishing with 0.05 μm diamond vibratory polishing for 18 hrs.

Chemical composition of the duplex stainless steel parts were analyzed using Energy Dispersive Spectroscopy (EDS). An FEI Quanta 600F environmental SEM equipped with X-Ray Energy Dispersive Spectrometer was used for this purpose. EDS spectrums were taken in two modes; area and spot. In area mode the HFW was fixed at 100 μm, encompassing several grains.

2.3.3 Mechanical Properties

The microhardness and tensile properties were measured and compared to wrought duplex stainless steel 2205. Vickers microhardness with 500 grams force for 15s was measured ten times. Tensile tests were done on samples with dimensions according to ASTM E8 specimen five for round samples (10 mm gauge length, 2.5 mm thickness). An Instron Universal Testing Machine, model eXpert 2653, was used. A constant displacement of 0.24 mm/min, corresponding to 2.5 $\times 10^{-4}$ s^{-1} strain rate, was used here.

2.4 Results

2.4.1 Powder Analysis

The DSS 2205 had spherical morphology as shown in the SEM micrograph in Figure 2.1. Results of the quantitative particle analysis, apparent density, tapped density, and the Hausner ratio are shown in Table 2.3.

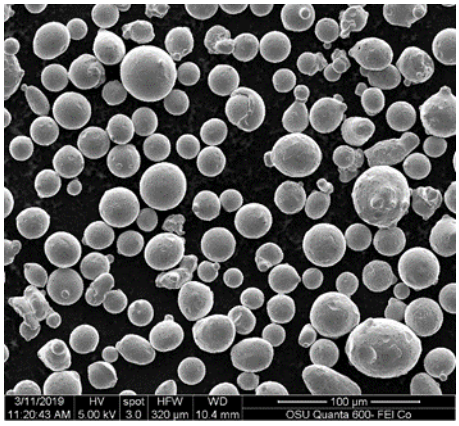

Figure 2.1. SEM micrograph showing the spherical morphology of duplex stainless steel 2205 powder

Table 2.3. Physical powder properties of duplex stainless steel 2205 powder

D10 (µm)	D50 (µm)	D90 (µm)	Apparent Density (g/cm^3)	Tapped Density (g/cm^3)	Hausner Ratio
17.60±0.1	28.50±0.2	47.50±1.4	4.29±0.01	4.88±0.05	1.14±0.01

2.4.2 Optimization of SLM Parameters

A power and scan speed map with all process parameters screened is shown in Figure 2. The highest volumetric energy density (VED) (140W, 200 mm/s, 463 J/mm^3) and lowest VED (107W, 600 mm/s, 119 J/mm^3) showed the lowest relative density (96-97%). In Figure 2.2, 14 of the 18 samples showed relative densities within a 1% range (97.7%-98.7%) over a wide range of VED (129 – 357 J/mm^3). According to Figure 2.2, there is a visual trend suggesting higher power results in consistently higher relative densities.

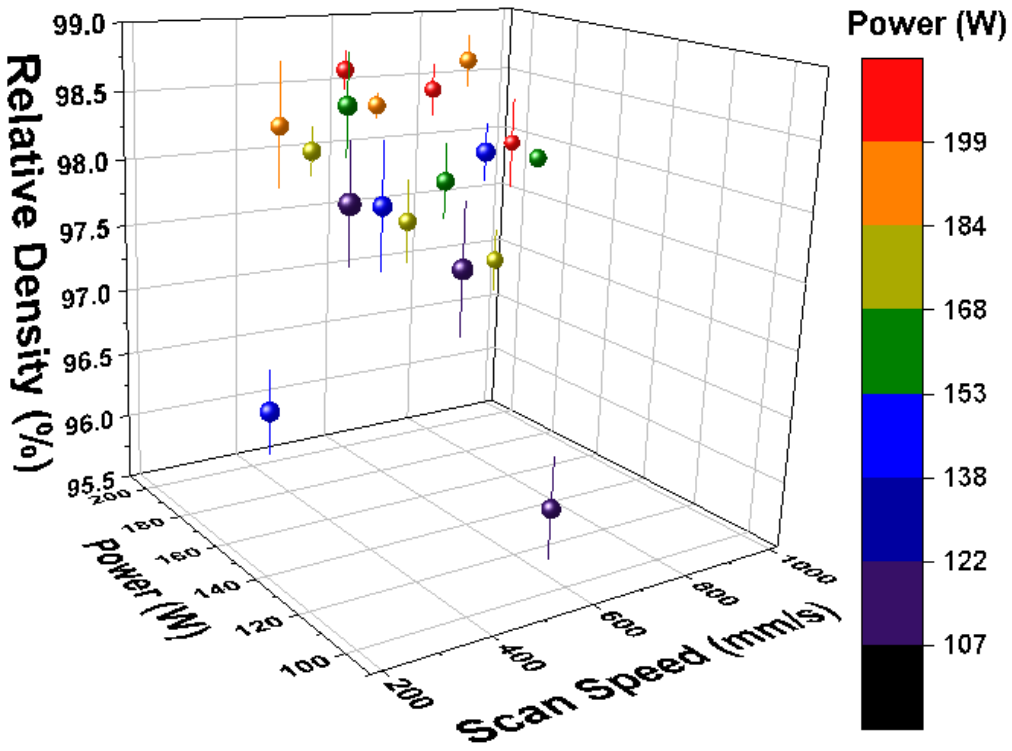

Figure 2.2. SLM parametric optimization based on varying power from 107-207 W and scan speed from 200-1000 mm/s (layer thickness was 0.03 µm and hatch spacing was 0.05 µm).

It should be noted that the values for relative density reported in Figure 2.2 are based on a wrought DSS 2205 sample with density of 7.79 g/cm^3. This is important as the reference sample has a balanced duplex microstructure, while the as-built samples are fully ferritic as will be shown in the XRD results. It is expected that the phase change will cause an increase in density. FCC austenite is more closely packed than BCC ferrite, with an atomic packing factor of 0.74 vs 0.68. It has been shown that at the BCC to FCC transition temperature of 907 ^{o}C pure iron increases density by 8-9% [63]. After heat treatment, the measured relative density of the selected sample (187 W, 800 mm/s) increased by ~0.5%. This is much less than the expected increase in density according to pure iron. The presence of alloying agents and voids are the likely limiting factors.

The final condition, 187 W, 800 mm/s and 156 J/mm^3, was selected as optimized SLM parameters because it had the highest relative density measured before heat treatment (98.6±0.3%) and after heat treatment increased to 99.1±0.3%. This processing parameter did not overheat the chamber as some of the 207W conditions did and operated at a favorably high scan speed which reduced processing time significantly.

2.4.3 Phase Analysis

During solution annealing at 1000-1200°C followed by water quenching there is a transition from a fully ferritic to an austenitic-ferritic duplex microstructure. Both delta ferrite (δ) and austenite (γ) are seen after heat treatment. Delta ferrite, as opposed alpha ferrite (α), forms when the liquid is cooled so fast that the traditional phase transformation sequence of δ to γ to α does not occur [20]. This is certainly the case for SLM, with cooling rates >10^4 ^{o}C/s [21]. The phase content has been analyzed in three ways: Optical microscopy, EBSD, and magnetometer methods. Results obtained from three measurements are shown in Table 2.4.

Table 2.4. Results of phase analysis for DSS 2205 processed by SLM at 187W and 800 mm/s

Measurement method	**EBSD**	**Optical Microscopy**	**Magnetometer**
Phase Content (% Ferrite)	51.7±0.7	53.0±4.8	55.7±1.0

The optical microscopy method relies on selective etching of ferrite to reveal the grains, taking optical micrographs, and subsequent image analysis by FIJI *Image J2* [64,65]. The analysis technique uses a converted grayscale image. Image threshold adjustment then segments the grains into light and dark, and the software can then determine ratios of light to dark and vice versa. Figure 2.3 shows an example of such a measurement conducted at 10X magnification.

EBSD phase maps can be automatically generated from the diffraction data after a scan is complete as shown in Figure 2.4. The phases determined were δ ferrite (red color) and γ austenite (green color). It is inconclusive whether the residual austenite shown (0.7%) is a result of some recrystallized γ austenite during the melt or simply a measurement noise.

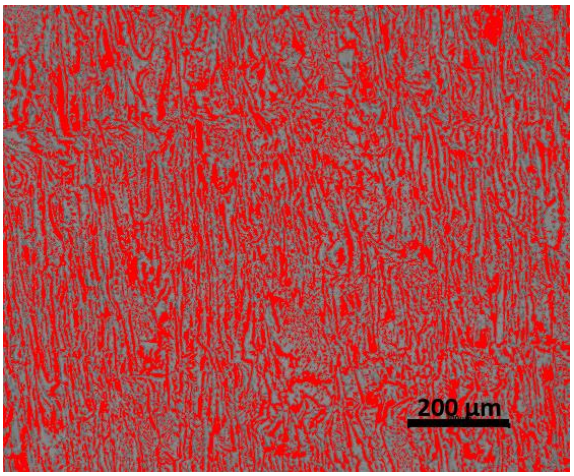

Figure 2.3. Sample micrograph analysis for phases from OM on DSS 2205 processed by SLM at 187W and 800 mm/s

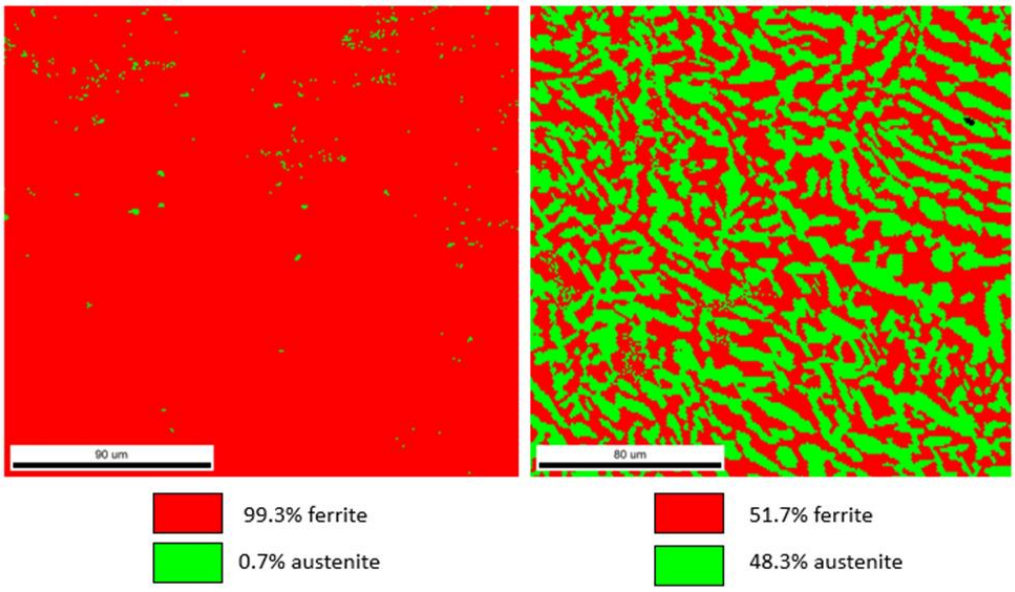

Figure 2.4. EBSD phase map for DSS 2205 processed by SLM at 187W, 800 mm/s showing the percentage of each phase in (a) as-built, (b) annealed sample

As ferrite is a magnetic phase while austenite is not, magnetic measuring tools may be used to estimate the ferrite content [66,67]. Magnetometer method uses an applied magnetic field to find the magnetic saturation moment, M_s (Am^2), which can be normalized to volume magnetization, $4\pi M_s$ ($\frac{A}{m}$), given a known volume, V (m^3). See Equation 1.

$$4\pi M_s = \frac{M_s}{V} \left(\frac{A}{m}\right) \quad (1)$$

Figure 2.5 shows a plot of magnetic moment as a function of applied magnetic field for as-built and annealed conditions. The M_s can easily be found as it is the value at which magnetic moment saturates[68].

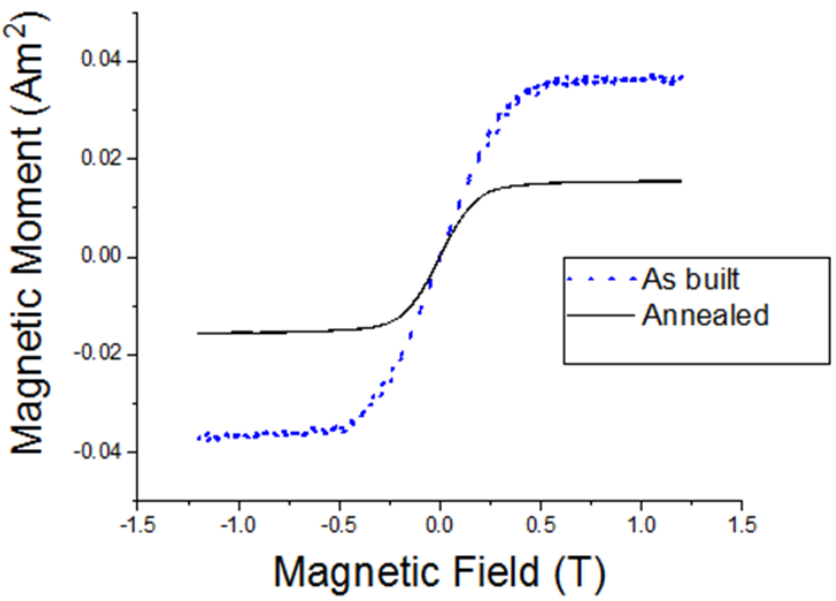

Figure 2.5. Magnetic moment as a function of applied magnetic field for as-built and annealed sample (SLM manufactured at 187W, 800 mm/s

Using the calculated $4\pi M_s$ from equation 1, the fraction of ferrite can be estimated. See equation 2.

$$F_f = \frac{4\pi M_{s,A}}{4\pi M_{s,B}} \times C_f \quad (2)$$

F_f is the fraction of ferrite, C_f is a correction factor, $4\pi M_{s,A}$ is the volume magnetization of the annealed condition, and $4\pi M_{s,B}$ is the volume magnetization of the as-built condition. Equation 2 is an estimate based on the assumption that ferrite is the sole contribution to the volume magnetization, as austenite is a non-magnetic phase. The main source of error is the porosity, which is non-magnetic and consumes volume. However, given that porosity in these parts is ~1%, the error is acceptable for the purposes of this study.

The correction factor, C_f, is based on the difference in chemical composition between the ferrite in the annealed sample and the ferrite in the as-built sample. To calculate C_f, the theoretical volume magnetization, $4\pi M_{s,T}$, of the ferrite in the as-built ($4\pi M_{s,TB}$) and the ferrite in the annealed condition ($4\pi M_{s,TA}$) must first be calculated. Merinov *et al.* [66] developed an empirical relationship for calculating $4\pi M_{s,T}$ of steels from chemical composition . See equation 3.

$$4\pi M_{s,T}\ (G)=21600-275(Cr)-330(Ni)-280(Mn)-610(Si)-260(Mo)-670(Ti)-630(Al)\ (wt.\ \%) \quad (3)$$

The individual elements are input into the equation as wt. %. Using compositional information determined from EDS (as shown in Table 2.6-2.7) the theoretical $4\pi M_s$ can be calculated for ferrite in the annealed sample and in the as-built sample. The correction factor, C_f, is the ratio of these values for theoretical, as-built to annealed as shown in equation 4:

$$C_f=\frac{4\pi M_{s,TB}}{4\pi M_{s,TA}} \quad (4)$$

Here, C_f was measured to 0.980±0.004 for this system. The calculated percent ferrite of 55.7 ± 1.0 % is consistent with the results measured by other methods, 51.7 ± 0.7 % in EBSD micrographs and 53.0 ± 4.8 % in optical micrographs.

2.4.4 Microstructure Analysis

Figures 2.6a-b show the microstructure of DSS 2205 as-built, parallel and perpendicular to build direction, respectively. The parallel cross section, Figure 2.6a, shows an intersection of melt pools and grains where grains are clearly oriented along the build direction. Using Heyn's lineal intercept method [69] the grain length and width were estimated. The length was calculated as 32.7 ± 4.3 μm. The width was measured as 18.8 ± 3.4 μm. This yielded an aspect ratio of 2:1.

In the perpendicular cross section, Figure 2.6b, the grain orientation resulting from the melt tracks can be seen. They show a crisscross pattern, consistent with the +45°/-45° hatching pattern. The thickness of the tracks (53.8 ± 11.6 μm) is consistent with the hatch spacing of 50 μm. The width and length of the grains from these cross sections measured 15.1 ± 4.3 μm and 15.1 ± 8.0 μm, respectively. From Figure 2.6c-d, the grain orientation is still present even after heat treatment. When analyzed parallel to the build direction, it is clear a significant portion of austenite grains have grown along the build direction (Figure 2.6c). However, when analyzed perpendicular to build direction, it can be seen that some of the grains have grown according to the direction of the melt tracks as shown in Figure 2.6d. For the cross section parallel to build direction, the measured length was 12.7 ± 4.7 μm and the width was 5.4 ± 0.8 μm with an aspect ratio of ~ 2:1. For the cross section perpendicular to build direction the measured length was 5.0 ± 0.5 μm and the measured

width was 5.1 ± 0.3 μm. The heat treatment resulted in a smaller grain size due to the change from single to dual phase.

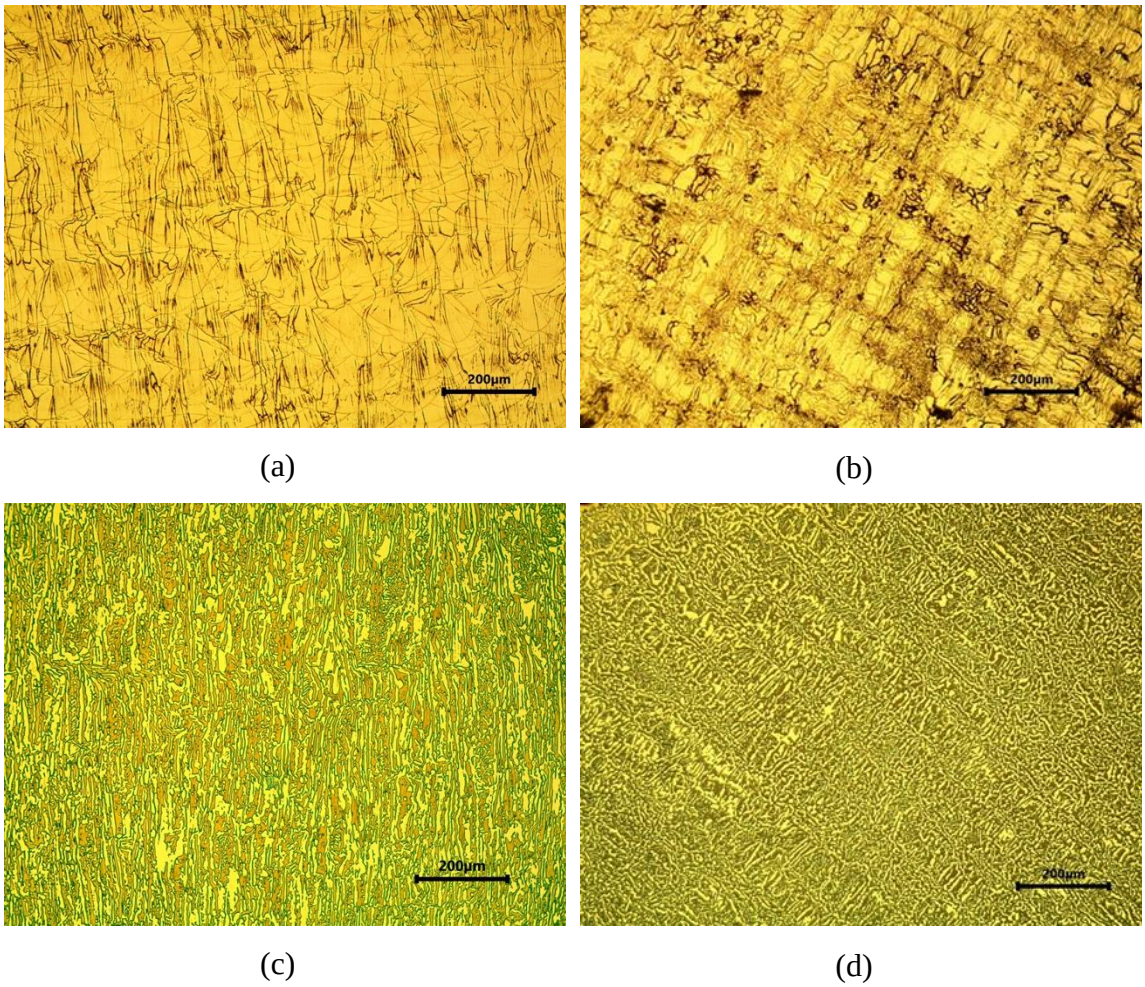

Figure 2.6. Optical micrographs DSS 2205 processed by SLM at 187 W and 800 mm/s (10X magnification) of (a) as-built parallel to build direction, (b) as-built perpendicular to build direction, (c) heat treated parallel to build direction and (d) heat treated perpendicular to build direction

Higher magnification (50X) micrographs were taken from as-built and heat treated in parallel and perpendicular to build direction and shown in Figures 2.7a-d. Finer details of the as-built grain structure are presented in Figures 2.7a-b. The closer inspection of the as-built condition, Figure 2.7b, shows three general types of grains including very small circular grains (2-10 μm), thin grains elongated along the melt track direction (2-5 μm X 40-70 μm), and a few larger round grains (20-40 μm). To the contrary, the higher magnification of the parallel cross section (Figure 2.7a) shows a few long (>100μm) grains

with lesser width (10-50 μm) oriented along the build direction. Again, the faint texture of the melt pool can be seen in the as-built parallel condition although it is masked by the heavy etching marks from the grain boundaries.

There is a noticeable reduction in grain width for the annealed parallel cross sections as shown in Figure 2.7c. A general orientation along the build direction is maintained in the parallel cross section. In the annealed perpendicular cross section, a few hints at orientation according to the scan tracks is also seen, see Figure 2.7d.

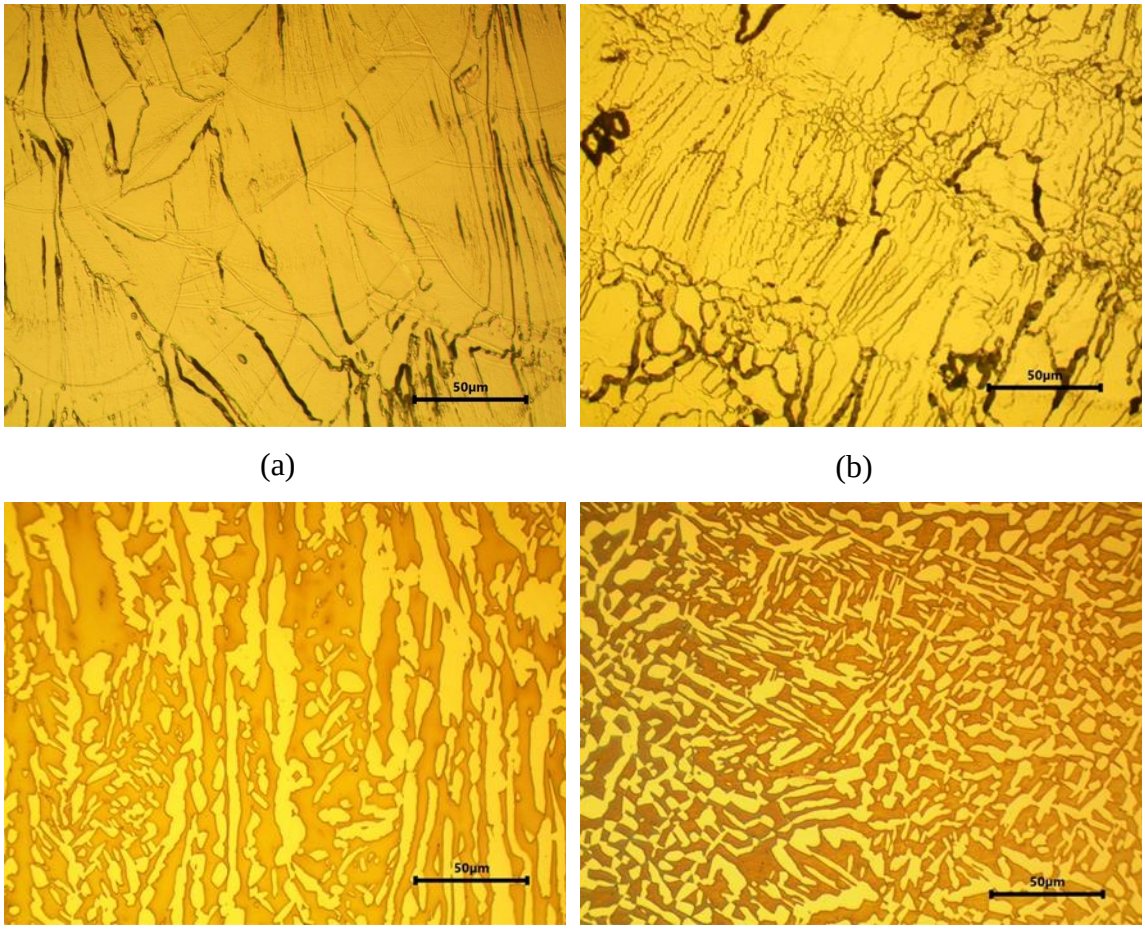

(a) (b)

(c) (d)

Figure 2.7. Optical micrographs of SLM manufactured duplex 2205 at 187 W and 800 mm/s (50X magnification) of (a) as-built parallel to build direction, (b) as-built perpendicular to build direction, (c) heat treated parallel to build direction and (d) heat treated perpendicular to build direction. Austenite is bright, ferrite is dark.

In certain areas which were heavily etched, there can be seen dark bands which are oriented in the same manner as the build layers as shown in Figure 2.8. The thickness of

the bands (111 ± 24 μm) exceeds the programmed layer thickness (30 μm) by a factor of 3-4.

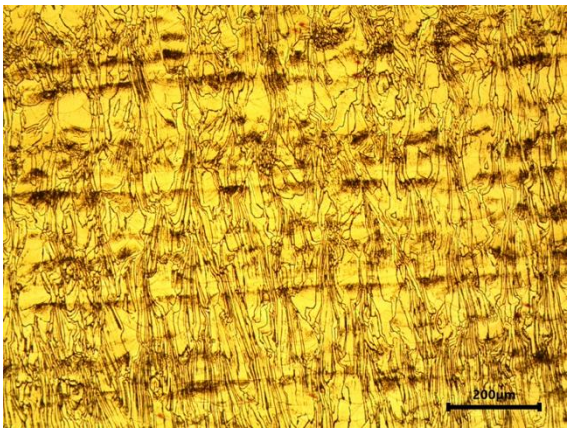

Figure 2.8. Optical micrograph of DSS 2205 processed by SLM at 187 W and 800 mm/s as-built and parallel to build direction (magnification 10X)

2.4.5 Texture analysis

The XRD patterns collected for the as-built and annealed conditions, perpendicular and parallel to build direction, are shown in Figure 2.9. The XRD patterns confirm the transition from fully ferritic to duplex structure after heat treatment and show evidence for a preferred orientation.

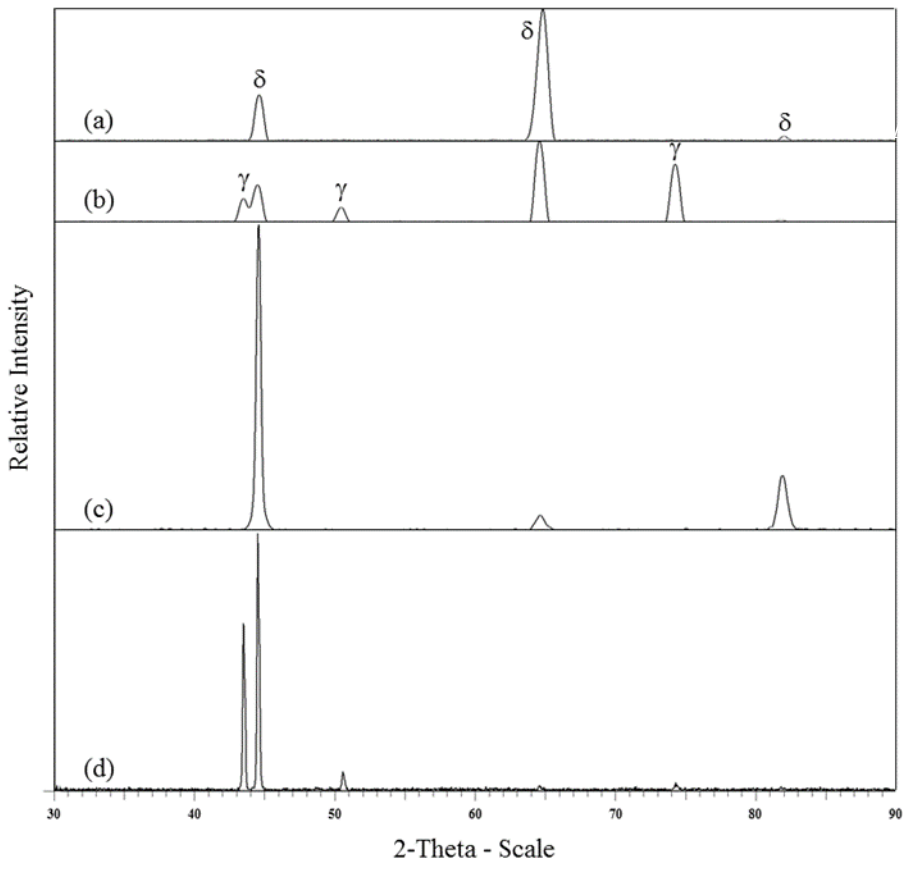

Figure 2.9. The XRD pattern of DSS 2205 processed by SLM at 187W and 800 mm/s
(a) as-built perpendicular and (b) annealed perpendicular (c) as-built parallel and (d) annealed parallel

The relative intensities presented in Table 2.5 were calculated based on the maximum peak intensity. The relative intensities of ferrite before and after heat treatment, and austenite after heat treatment, are compared to the relative intensities for BCC and FCC Fe-Cr-Ni given in the Crystallography Open Database, made available by Bruker in the EVA software [70]. The peak corresponding to the (200) hkl plane in the ferrite from the perpendicular cross section shows nearly a 10-fold increase in relative intensity compared to the reference database. It is the most prominent peak, whereas it is the least prominent peak according to the reference database. This peak corresponds to the (200) hkl peak, or the [001] direction [71]. The austenite from the perpendicular cross section shows relative intensities more in line with the reference database. However, the (110) and (200) hkl relative intensities are half the relative intensity expected. This indicates the (220) hkl peak is more strongly preferred than usual, which is the [110] direction [71]. The parallel cross

sections show that when analyzed from a different orientation, different hkl planes are diffracted. Specifically, the (110) for ferrite and the (111) for austenite. This again confirms preferred crystallographic orientation in the sample. It should be made clear that the relative intensity data does not quantitatively describe the texture [71]. It gives a general idea for the preferred orientation. However, quantitative data was extracted was XRD. Using the Williamson-Hall procedure[71], the crystallite size was calculated. This is also shown in Table 2.5. The crystallite size is larger on the parallel cross sections, consistent with expectations from the grain analysis. No evidence of secondary phases was seen from XRD. The electron backscatter diffraction (EBSD) data shows the crystallographic orientation in each individual grain, as shown in Figure 2.10.

Table 2.5. Relative intensities and crystallite size calculated on DSS 2205 processed by SLM on phases before and after heat treatment, perpendicular and parallel to build direction

Phase	**As-Built Ferrite**			**Annealed Ferrite**			**Annealed Austenite**		
(hkl)	(110)	(200)	(211)	(100)	(200)	(211)	(111)	(200)	(220)
Relative Intensity (RI), Perpendicular	0.35	1	0.03	0.46	1	0.02	0.40	0.25	1
RI, Parallel	1	0.05	0.18	1	0.02	0.01	1	0.11	0.05
RI from reference (Fe-Cr-Ni) BCC/FCC [70]	1	0.128	0.337	1	0.128	0.337	0.811	0.534	1
Crystallite Size, Perpendicular (nm)		11				11			
Crystallite Size, Parallel (nm)		15				13			

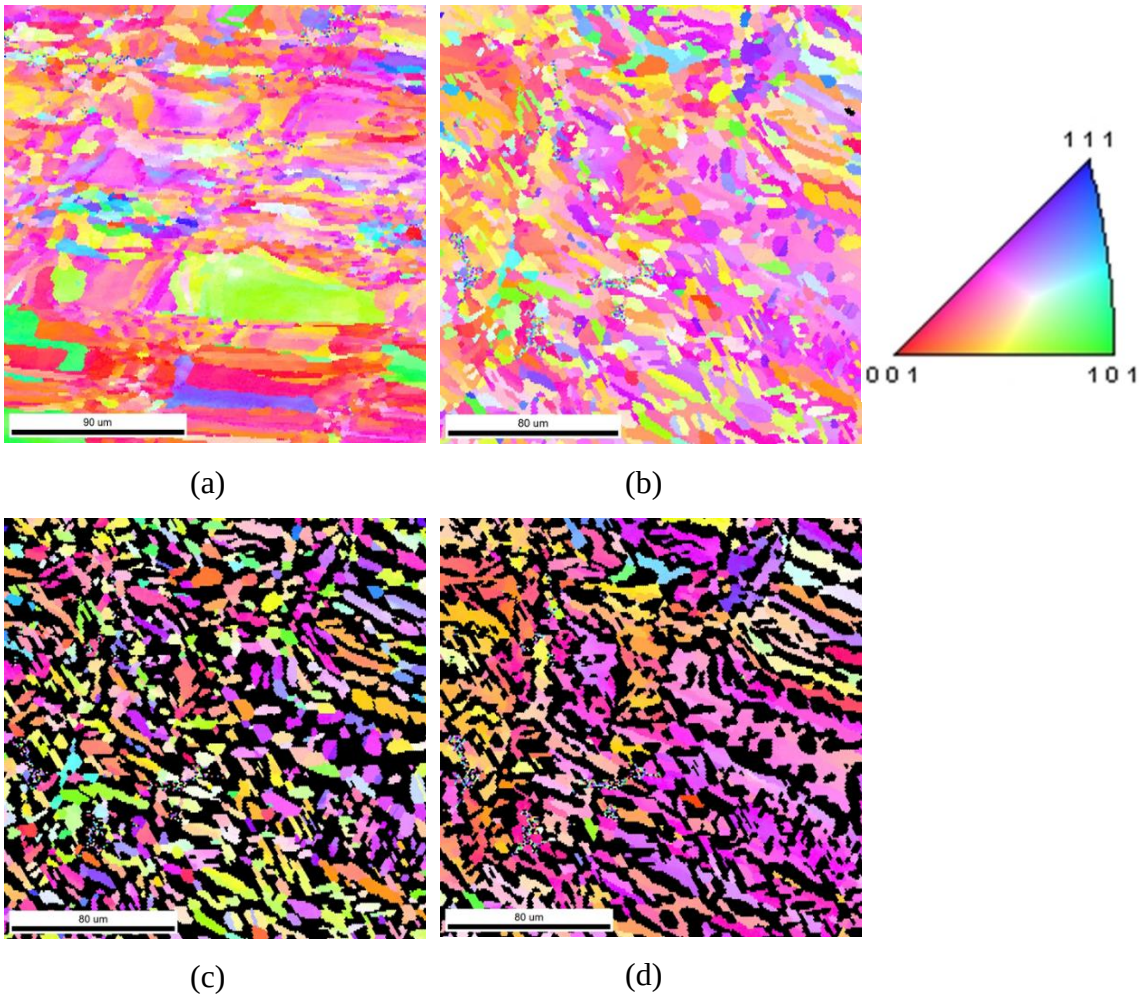

Figure 2.10. Inverse pole figures of duplex 2205 processed by SLM at 187W and 800 mm/s perpendicular to build direction (a), as- built (b) annealed (c) annealed austenite only (d) annealed ferrite only

The cross section shows a general preferred orientation with grains color coded purple being predominant and grains color coded orange being secondary as shown in Figure 2.10a. Both as-built (Figure 2.10a) and heat treated (Figure 2.10b) show similar textures. For the annealed sample, Figure 2.10b, ferrite and austenite grains were isolated using the EBSD software, as shown in Figure 2.10 c-d. In short, Figures 2.10c-d combined are the same as Figure 2.10b. When segmented into ferrite and austenite maps for the heat treated sample, it is clear that this preferential texture is more pronounced in the ferrite phase as evident in Figure 2.10d than in the austenite phase as shown in Figure 2.10c.

The texture was measured by using pole figures as shown in Figure 2.11. For ferrite as-built and annealed, the preferred orientation was in the [001] build direction, where the

maximal texture index of 19.1 and 17.8 respectively were measured. This is consistent with XRD results in Figure 2.9. The austenite showed a mixed texture. Maximal texture index of 8.5 occurred in the [110] direction, but [001] followed closely with a texture index of 8.4. This texture in austenite is not entirely consistent with the XRD data shown in Figure 2.9. The XRD data shows [110] as significantly higher from the relative intensity.

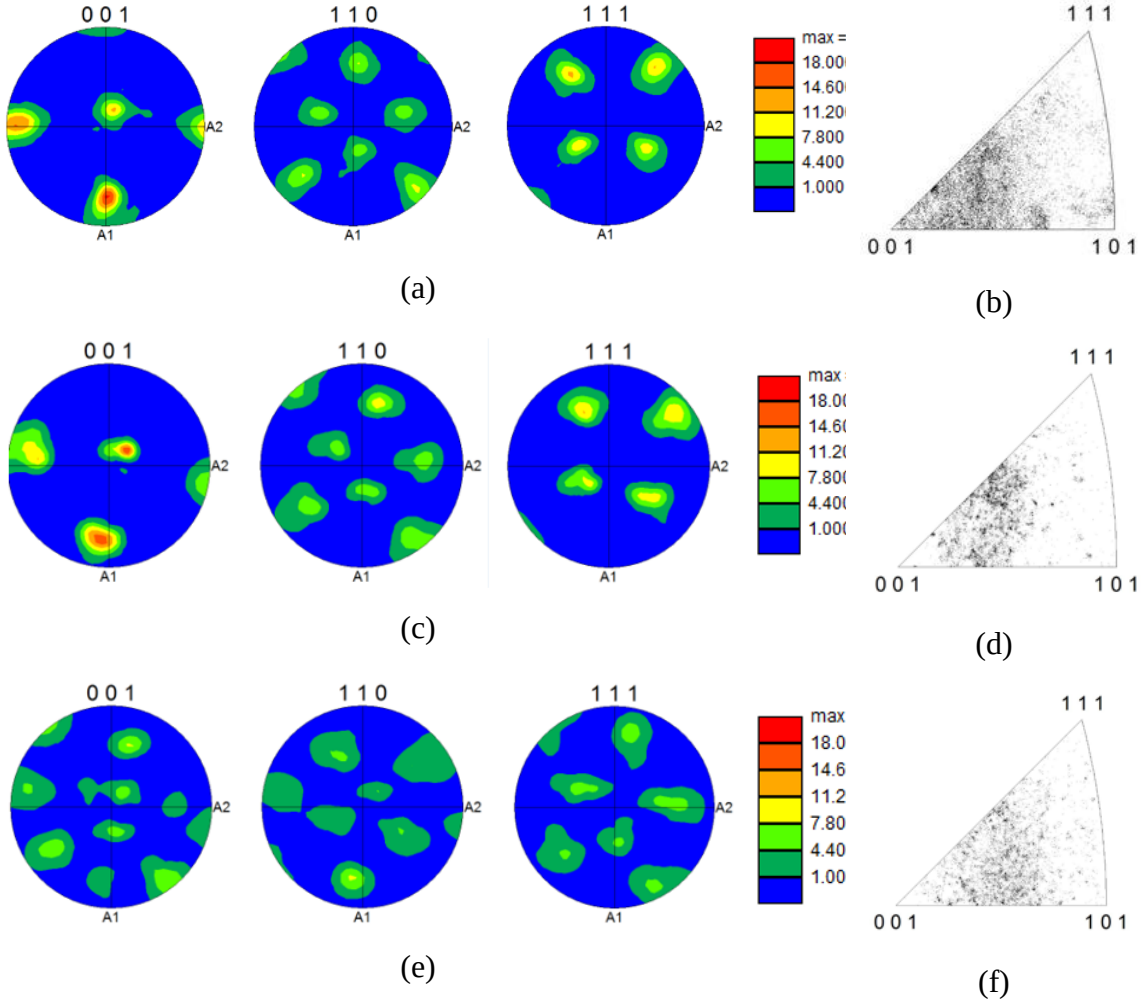

Figure 2.11. Pole figures and inverse pole figures ([001] reference) for DSS 2205 processed by SLM at 187W and 800 mm/s showing three most prominent hkl planes for (a-b) as-built, (c-d) heat treated ferrite and (e-f) heat treated austenite

2.4.6 Compositional Analysis

The bulk composition of the SLM processed DSS 2205 was determined by the EDS and the comparative results between the powder, as-built, and heat treated samples are presented in Table 2.6. The measured concentrations were largely consistent with the

powder feedstock composition with minor deviations. For example, Si is lower in the SLM samples than in the powder (0.68 wt.% in powder, 0.42-0.51 wt.% in SLM), and Ni was slightly higher in SLM compared to powder (5.40 wt.% in powder, 5.51-5.89 wt.% in SLM). The data for the powder is provided by the vendor, so it is difficult to ascertain whether these differences are significant.

Table 2.6. Results of bulk EDS analysis for DSS 2205 manufactured by SLM at 187W and 800 mm/s. The information for the powder is provided by the vendor, Carpenter Technology.

EDS composition (wt.%)	**Fe**	**Cr**	**Ni**	**Mo**	**Mn**	**Si**
DSS 2205 powder	67.30	22.20	5.40	2.97	1.06	0.68
DSS 2205 as-built	67.10±0.26	22.42±0.10	5.70±0.19	3.29±0.10	0.99±0.10	0.49±0.02
DSS 2205 annealed	67.26±0.21	22.24±0.21	5.76±0.13	3.19±0.11	1.08±0.10	0.46±0.04

Spot EDS was done on individual ferrite and austenite grains as shown in Table 2.7. The ferrite grains showed elevated Cr and Mo which supported their role as ferrite stabilizers [1]. The austenite grains showed higher Ni and Mn, supporting their role as austenite stabilizers [1].

Table 2.7. Results of spot EDS analysis for DSS 2205 processed by SLM at 187W and 800 mm/s targeted at select ferrite and austenite grains

EDS composition (wt.%)	**Fe**	**Cr**	**Ni**	**Mo**	**Mn**	**Si**
DSS 2205 annealed ferrite	66.73±0.16	23.26±0.05	4.70±0.10	3.86±0.16	0.93±0.14	0.52±0.05
DSS 2205 annealed austenite	68.06±0.07	20.73±0.04	6.94±0.04	2.69±0.06	1.14±0.10	0.44±0.02

Figure 2.12 a-b shows spot EDS conducted on suspect dark contrast spots present in the as-built and annealed samples, respectively. Table 2.8 presents the spot EDS analysis associated with Figure 2.12 a-b. The spots were selected at random locations on the sample. If these spots were simply voids, one would expect their composition to fall inside the

compositional window established in Table 2.6, between ferrite and austenite. However, in both the as-built (Figure 2.12a) and annealed (Figure 2.12b) samples, significant elemental segregation was observed on these spots. For example, the range for Cr content is 20.69 – 23.31 wt. % from Table 2.7. The spot EDS yielded 26.87±0.42 wt.%. The as-built samples showed Cr-enrichment coupled with high reduction in Ni and Mo. The heat treated sample also showed evidence of inclusions at the dark contrast spots, where there was a sharp increase in Mn and Si coupled with a decrease in Fe. For example, the compositional range for Mn is 0.79-1.24 wt. %. The measured concentration in the dark contrast spots was 4.43±0.85 wt.% in the annealed sample. The spots occurred exclusively along grain boundaries for the as-built sample but were both within grains and along grain boundaries in the annealed sample.

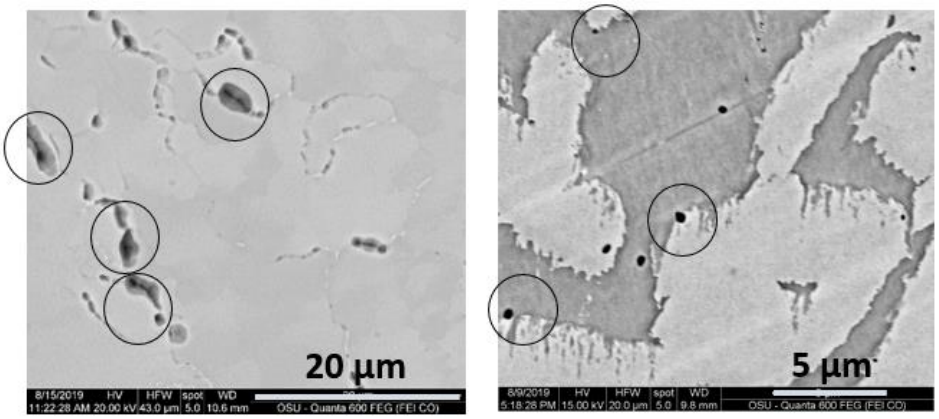

(a) (b)

Figure 2.12. Spot EDS on DSS 2205 processed by SLM at 187W and 800 mm/s
(a) as-built and (b) annealed

Table 2.8. Results of spot EDS analysis for DSS 2205 processed by SLM at 187W and 800 mm/s

EDS composition (wt.%)	**Fe**	**Cr**	**Ni**	**Mo**	**Mn**	**Si**
DSS 2205 as-built grain boundary spots	67.67±0.17	26.87±0.42	3.36±0.31	0.32±0.09	1.78±0.16	0.01±0.01
DSS 2205 annealed grain boundary spots	62.62±0.51	21.14±0.54	5.58±0.31	3.72±0.86	4.43±0.85	2.53±0.82

2.4.7 Mechanical Properties

Characterization of mechanical properties is important for determining viability in load and pressure bearing applications. Microhardness, yield strength, tensile strength, and percent elongation are summarized in Table 2.9. Microhardness was characterized both parallel and perpendicular to the build direction to generate an initial understanding for how the grain orientation effects bulk properties. Results are compared to the vendor reported properties as well as the requirements per ASTM A790 [26].

Table 2.9. Results from mechanical properties testing for DSS 2205 processed by SLM at 187 W and 800 mm/s

Sample	**Microhardness (HV) perpendicular to build direction**	**Microhardness (HV) Parallel to build direction**	**Yield Strength (MPa)**	**Tensile Strength (MPa)**	**Elongation (%)**
As-built	419±7	362.74±14	826±32	872±33	11±2
Heat treated	258±8	265±4	465±3	622±19	21.3±1.4
Wrought (ASTM A790)	267±4 (293 MAX)	267±4 (293 MAX)	655 (448)	882 (621-1103)	25 (25)

2.4.8 Surface Roughness Measurements

The surface roughness shown in Figures 2.13a-b was collected on all samples printed in the initial optimization run. Both parallel and perpendicular surfaces to the build direction were measured. For the surface perpendicular to the build direction, there was a general trend of decreasing surface roughness with increasing VED. The lowest surface roughness was obtained at 139 W, 200 mm/s, and 463 J/mm^3. The main outlier to this trend was observed at 107W, 200 mm/s, and 357 J/mm^3. When considering the parallel surface there was no obvious trend of surface roughness with VED.

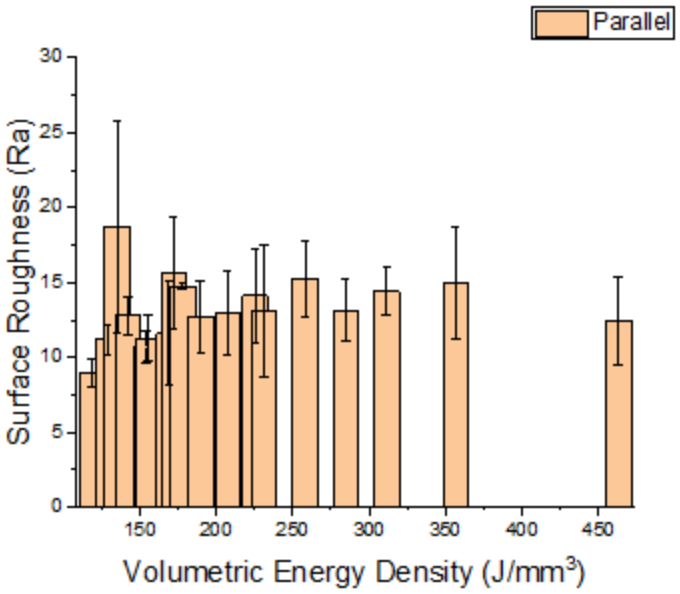

(a)

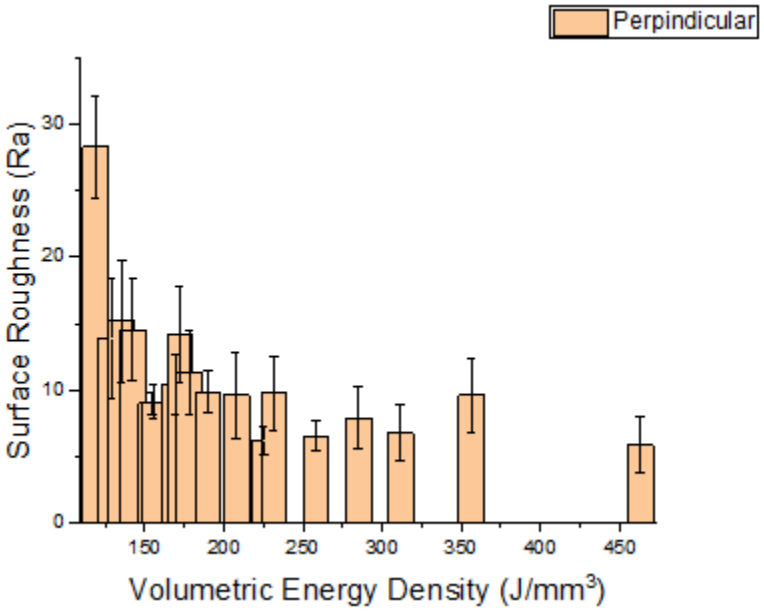

(b)

Figure 2.13. Surface roughness measurements of DSS 2205 manufactured by SLM at 187W and 800 mm/s (a) parallel and (b) perpendicular to build direction

2.5 Discussion

2.5.1 SLM parametric trends

The spherical particle morphology and fine particle size (D_{50}=28.50±0.20) demonstrate that the powder analyzed in this study is compatible with SLM requirements. The Hausner ratio is 1.14, which rates as good flow according to the Carr flowability scale [72]. This is promising for achieving good powder bed density after spreading on the build plate. The processed sample with the lowest VED showed the lowest relative density due to insufficient melting and lack of fusion defects. The processed sample with the highest VED also had the lowest relative density, which could have been due to keyhole porosity, as has been shown in the literature [73]. However, an in-depth analysis of the pore structure was not done to determine with certainty that keyhole porosity occurred in this work. Apart from these extreme limits, no meaningful trend was found with the energy density parameter. Prashansh *et al.* [74] showed that drastically different densities can be obtained with identical energy density but different power and scan speed combinations. This work supports the fact that energy density is not a meaningful parameter for process optimization as published by Bertoli *et al.* [55].

The combinations of high power and high scan speed produced better results than low power and low scan speed at the same volumetric energy density (i.e. 320W, 1455 mm/s versus 40W, 182 mm/s for Al-12Si) [74]. Indeed, the highest reported relative density for Duplex 2205 occurred at 250W and 850 mm/s [8] in contrast to the 187W, 800 mm/s parameters used in this study. Qiu *et al.* [21] showed that laser power had the most significant effect on porosity for 316L stainless steel. Figure 2.2 indicates that high relative densities are consistently obtained at higher powers, however there is still some variability; The maximum allowable power for this study was 207 W. It was not evident going to maximum power (207 W) provided any benefit over 187W. This suggests other factors may be at play.

It has also been shown that a 66^{o} scan rotation results in a higher relative density (99.97%) compared to no rotation (99.01 %) [8]. The scan rotation used here was +45^{o}/-45^{o}. A comprehensive study on the effect of different scan rotation strategies on relative density could be a topic of future work.

2.5.2 Heat treatment and phase analysis

Effect of the post processing heat treatment for DSS 2205 processed by SLM on the phase content and other properties is published [7,8] with a maximal austenite content achieved at temperatures of 1000-1050 ^{o}C [7,8]. However, maximum austenite content of 34% (5 min, 1000 ^{o}C, vacuum) was measured by EBSD in [7], whereas maximum austenite contents of 43.2% and 46.4% (5 min, 1000 ^{o}C, air and 60 min, 1000 ^{o}C, air, respectively) were measured by EBSD in [8]. According to ASTM A890 [23], the minimum annealing temperature for duplex castings should 1040 ^{o}C to achieve optimal corrosion properties. According the phase diagram, δ and γ are thermodynamically stable together up to 1300 ^{o}C for an Fe-Cr-Ni alloy with 22% Cr [75].

Heat treatment at 1100 ^{o}C for one hour in air followed by water quench was used as the heat treatment here. The austenite content measured by EBSD was 48.3% as shown in Figure 2.4, indicating a nearly balanced microstructure had been achieved after heat treatment. The three methods of measuring ferrite content in this work were reasonably consistent with each other. When considering all three methods together, it is evident that the real value for austenite content was between 42.2-51.8%, as shown in Table 2.4. Magnetometer measured 55.7% ferrite, or 44.3% austenite in the bulk of specimen while the EBSD measurement is only scanning a small cross section of the specimen. While an austenitic-ferritic stainless steel of this composition will meet the technical definition of duplex with 30%-80% ferrite [1], it has been reported that optimal mechanical properties occur when the phases are closely balanced [76], as is the case here. This is a result of the fine grain size which can be obtained with a balanced microstructure [76].

2.5.3 Microstructure and Grain Orientation

The microscopy data shows that certain grain orientation patterns can be seen in the as-built and annealed conditions which are connected to the processing conditions (Figures 2.6-7). Ferrite and austenite grains tend to align in certain directions, suggesting the layerwise building and +45^{o}/-45^{o} scan strategy influence the location of ferrite grain boundaries. This influences the nucleation and growth of the austenite after heat treatment. In accordance with general theories of heterogeneous nucleation, the austenite would prefer to nucleate and grow at the grain boundaries [77]. When analyzed parallel to build direction (Figure 2.6 and 2.7 (a,c)) the effects of the layering and grain elongation along the build

direction are most noticeable, but when analyzed perpendicular (Figures 2.6 and 2.7 (b,d)) the effects of the scan strategy are most noticeable. The fact that the texture remains after the heat treatment is further proof the austenite tends to crystallize at the grain boundaries.

When analyzed parallel to build direction, it is clear that a significant proportion of grains are elongated along the build direction as shown in Figures 2.6-7. This is supported by the grain size measurements. The length and width of as-built grains measured 32.7 ± 4.3 μm and 18.8 ± 3.4 μm, respectively. The length and width of the annealed grains measured 12.7 ± 4.7 μm and 5.4 ± 0.8 μm, respectively. However, Figures 2.6b and 2.7b shows the influence of $+45^{o}/-45^{o}$ scan strategy on the grain orientation. The grain size measurements also determined that there is a net reduction in grain size after the heat treatment. This is likely an effect of transitioning from a single-phase material to a dual phase material. The measured grain sizes from the perpendicular cross sections further support this theory. The measured width and length of the as-built grains were 15.1 ± 4.3 μm and 15.1 ± 8.0 μm, respectively. The measured width and length of the annealed grains were 5.1 ± 0.3 μm and 5.0 ± 0.5 μm, respectively.

Certain microstructural features warrant additional explanation such as the layering bands in Figure 2.8. Based on the measured distance between the bands (111±24 μm) and the layer thickness of 30 μm it would seem that every 3-4 layers (90-120 μm) there is insufficient melting. Reasons for the insufficient melting are unclear at this time but one hypothesis is that it is related to combined effects of the dimensional solidification shrinkage and the high powder feed ratio (2.3) needed to ensure uniform spreading. The powder feed ratio is the ratio of the distance the powder reservoir moves upwards to the distance the build platform moves downwards. It is >1 to ensure uniform spreading. It's possible during the print that > 30 μm may be deposited and melted for a single layer, resulting in lower than expected energy density and thus layering defects from lack of fusion.

The preferred grain orientation results in a crystallographic texture, per the EBSD data in Figure 2.11. The texture observed for the ferrite, [001], is common for SLM materials due to the highly directional heat flow and solidification of each layer [12]. The austenite shows a more mixed texture as shown in Figure 2.11. There is a discrepancy between the texture determined for austenite from EBSD, and the preferred orientation

observed in the XRD data, given in Figure 2.9. XRD shows a predominately [110] orientation, while EBSD shows a mixed orientation with [110] and [001] being the most prominent. The reasons for why EBSD is showing a more mixed texture for austenite than XRD is unclear at this time. XRD collects information on a larger volume of material. Penetration depths for XRD are on the order of microns, while penetration depths for EBSD are on the order of nanometers. With XRD, relative intensity measurements show preferred orientation, but do not fully quantify the texture unless techniques which tilt and rotate the sample stage are done to generate pole figures [71]. It is evident from the combined results of microscopy, XRD, and EBSD that the layerwise processing and $+45^{o}$ / -45^{o} scan strategy influence the grain orientation. This is important as preferred orientation will likely influence the resultant mechanical properties, and possible the corrosion performance as well.

2.5.4 Compositional Analysis

Vaporization of Cr, Mn, and Ni elements can occur during selective laser melting at high energy density [61], and reduction in Cr content could be detrimental to pitting corrosion resistance. The bulk EDS measurements did not show any evidence of elemental vaporization as show in Table 2.6. The processing parameters used here of 187W, 800 mm/s, and 156 J/mm^3 did not cause any significant vaporization.

Elemental segregation is indicative of the presence of secondary phases which are not present in high enough amounts to be detected by the XRD. However, compositional gradients may introduce sites for corrosion attack to occur. For example, if Cr-enriched sigma phase is present, the area in the vicinity of the sigma grains will be depleted in Cr and hence, susceptible to corrosion attack. From the spot EDS results reported in Table 2.5, elemental segregation was observed in both as-built and annealed samples at the locations shown in Figure 2.12. It has been reported that intergranular chromium nitrides (Cr_2N) form during SLM for DSS 2205 [7]. A possible mechanism for formation is that the delta ferrite, which may be supersaturated in nitrogen as a result of the nitrogen filled chamber, is held at temperature of 700-900 °C for ample time after solidification, thus providing the conditions at which Cr_2N can form [7]. This is similar to conditions which could occur during welding and precipitation of chromium nitrides as a result [49]. Another theory which should be considered is formation of sigma phase (σ). However, if sigma phase had

precipitated, there would be an increase in Mo to go along with the increase in Cr which was not observed here. Nevertheless, Cr segregation is an indication that the as-built sample could be susceptible to pitting corrosion as there may be depleted Cr adjacent to the enriched area.

The spot EDS results from Table 2.8 show Si and Mn enriched inclusions in the annealed samples. The locations are shown in Figure 2.12. While Si could be explained as impurities from the SiC polishing paper, the Mn cannot. Thus, other explanations must be explored. Mn and Si have been reported along with O in 316L during SLM [21,78]. The researchers hypothesize they are particulates of SiO_2 and MnO_2. According to the Ellingham Diagram [79] Mn and Si have the most thermodynamically stable oxides of all elements present. Their free energies of formation at 1100 ^oC are -580 J/mol O_2 and -630 J/mol O_2 respectively [79]. The powder feedstock has an oxygen content of 0.03 wt. %. This is the likely source of the oxygen, as the print is maintained at <0.01% oxygen atmosphere. It is possible oxides may form during the print, but clearly the 1100 ^oC anneal causes significant precipitation and growth.

In another work Mn segregates at M-γ grain boundaries and was explained as a function of the relatively slow diffusion of Mn in γ austenite compared to M [80]. Another paper showed the diffusivity of Mn in ferrite is 1-2 orders of magnitude higher than the diffusivity of Mn in austenite across temperatures, largely due to the lower activation energy [81]. For example, at 1100 ^oC the diffusion coefficient of Mn in γ is 3.5e-15 m^2s^{-1} and in α it is 3.1e-13 m^2s^{-1}. However, the dark spots enriched in Si and Mn also appeared inside grains, so a segregation mechanism is unlikely.

2.5.5 Mechanical properties and surface roughness

For all duplex steels processed by SLM, the heat treatment necessary to recrystallize γ and obtain the duplex microstructure will also recover the mechanical properties [7,8]. The reasons given for the change are the reduction in density of dislocations and dissolution of Cr_2N [7]. Dislocation density was not characterized in this study, but other reports show a reduction in dislocation density after heat treatment of the SLM manufactured duplex 2205 parts [7].

After the heat treatment the ultimate tensile strength decreased from 872±33 MPa to 622±19 MPa and the elongation increased from 11±2.0% to 21.3±1.4% as presented in

Table 2.9. Compared to the reference wrought sample (882 MPa, 25% elongation) and results for annealed SLM DSS2205 reported in literature (720-870 MPa, 23-46% elongation) [7,8], the UTS and elongation were measured to be low. This suggests the presence of defects which cause premature necking and failure, such as the 1% residual porosity and the suggested oxides.

SLM manufactured parts, and 3D printed parts in general, are known to have anisotropic properties. For example, the as-built parts printed in this work show a difference of +60 HV when comparing testing parallel and perpendicular to build direction as shown in Table 2.9. The reason is likely the grain orientation, which shows elongation along the build direction. Microhardness anisotropy disappears after the heat treatment. The grains still show elongation along the build direction. It's possible the cause of the anisotropy in the as-built samples it not so much a function of the grain orientation, but the presence of the layering defects as shown in Figure 2.8.

It is established that higher surface roughness is detrimental to corrosion performance. For example, the detrimental effects of the native roughness on the corrosion performance of AlSi10Mg and 316L manufactured by SLM have been demonstrated [60,82]. It is important to characterize the surface roughness for SLM manufactured parts so that appropriate surface finishing procedures may be designed. While no clear trend was observed with surface roughness, there were a few interesting observations. For the surface roughness measured perpendicular to build direction (laser facing surface) the highest surface roughness (28.6±3.8 μm) occurred at the lowest volumetric energy density (119 J/mm^3), and the lowest surface roughness (5.9±2.1 μm) occurred at the highest volumetric energy density (463 J/mm^3) as shown in Figure 2.13b. The tendency toward high roughness at low VED could be explained by lack of fusion and the resultant high surface porosity [83]. The low surface roughness at high VED could be due to increased spattering [84]. It is interesting that the lowest roughness condition (highest volumetric energy density, 463 J/mm^3) had one of the lowest relative densities measured during the experiment (96.7%). This could be due to the formation of keyhole porosity. Studies on SLM Ti-6Al-4V show that keyhole porosity is most prevalent at high VED when power is optimum and scan speed is low [73]. As a comparison to these results shown in Figures 2.13a-b, 1D and 2D mill finishes for wrought stainless steels have roughness values of

~5.5 and ~0.4 μm, respectively [85]. 1D mill finishes have been hot rolled and acid pickled to remove the mill scale. 2D finishes go through an additional, polished roller. It is clear when considering both the parallel and perpendicular surface roughness of the SLM 2205 parts combined, it is higher than any surface roughness found in typical service. As such, surface finishing procedures may need to be considered.

2.6 Conclusions

Duplex stainless steel 2205 parts were successfully built via SLM. The optimal processing conditions on an ORLAS Laser Creator were determined and subsequent characterization of phase content, grain orientation, texture, chemical composition, mechanical properties, and surface roughness were accomplished. A standard solution annealing heat treatment was done to restore a nearly 50-50 balance between δ and γ. Comparisons were made between as-built, annealed, and wrought counterparts. Areas with a significant knowledge gap, such as grain orientation, chemical composition, and surface roughness, were studied. Certain key findings are reported here:

1. The duplex microstructure is recovered using the solution annealing heat treatment of 1100 °C for 1 hr in air atmosphere followed by water quenching. A nearly balanced phase content is achieved when using such a technique. The phase content was characterized successfully using optical image analysis, EBSD, or magnetometer and was 53.0±4.8 % ferrite, 51.7±0.7 % ferrite and 55.7 ±1.0 % ferrite respectively. A future avenue of research for heat treatment is the effect on the observed Si and Mn segregation.
2. The orientation of the grains is influenced by the processing condition. There is significant orientation along the build direction, consistent with directional solidification from the powder bed to the surface. The measured aspect ratio of the grains is approximately 2:1 for both as-built and annealed. There are also grains oriented in accordance with the +45^{o} /-45^{o} scan strategy as shown in Figures 2.6b and 2.6d. The effect of novel scan strategies on grain orientations is a future opportunity for study.
3. The grain orientation resulted in a preferred crystallographic orientation. Most notable is the strong [001] texture of ferrite grains before and after heat treatment. The measured texture index of the ferrite in the as-built and annealed condition is

19.1 and 17.8 respectively. Austenite grains also orient along the build direction, but a significant proportion appear to orient in accordance with the melt tracks. EBSD shows a mixed texture with the [110] and [001] directions having a texture index of 8.5 and 8.4 respectively. XRD relative intensity measurements are consistent with EBSD for ferrite. The [001] peak is dominant in as-built and annealed conditions, with relative intensity of 1. The XRD results for austenite are not entirely consistent with the EBSD. XRD shows a relative intensity of 1 for [110], 0.40 for [111], and only 0.25 for [001] directions.

4. The bulk composition meets expectations for DSS 2205 which explains the balanced phase content. This is also promising for corrosion applications. Cr and Mo are reported as 22.20 wt. % and 2.97 wt. % for the powder and were measured as 22.24±0.21 wt. % and 3.19±0.11 wt. % in the annealed SLM parts, respectively. However, elemental segregation is present in both as-built and heat treated conditions and may cause problems. In the as-built samples, Cr was measured at grain boundaries as 26.87±0.42 wt. % using spot EDS. In the annealed samples, Mn and Si were measured at locations within grains and along grain boundaries as 4.43±0.85 wt. % and 2.53±0.82 wt. % respectively. Identifying the exact nature of the precipitates or inclusions and their number density is the next step forward for compositional analysis.
5. Mechanical properties were measured. As-built samples were hard, strong, and brittle. Microhardness was 419±7 HV, UTS was 872±33 MPa, and elongation was 11±2 %. The heat treatment restored the ductility to an extent, but the properties are still inferior to the wrought counterpart. UTS on the annealed sample measured 622±19 MPa versus the reported 882 MPa for the wrought, and the elongation measured 21.3±1.4 % wrought versus the reported 25 % for the wrought. However, the measured microhardness of the annealed sample, 258±8 HV, was comparable to the measured microhardness of the wrought counterpart, 267±4 HV. This suggests the presence of large, randomly distributed voids and defects which influence the tensile test results but not the microhardness test results. This is likely due to the residual 1% porosity. The effect of higher processing powers on relative density and mechanical properties is an appropriate topic for future research.

6. There is a high native SLM surface roughness across all processing conditions. Measurements varied from 5.5-28.6 μm. This indicates finishing procedures may need to be considered depending on the application. Future work could design a finishing method to reduce roughness.

Acknowledgements

The authors would like to acknowledge the funding of critical equipment provided by the Murdock Charitable Trust (Contract number: 2016231:MNL:5/18/2017). G.N thanks Oregon State School of Mechanical, Industrial, and Manufacturing Engineering. The authors thank Professor Albrecht Jander and the OSU Applied Magnetics Laboratory for running and analyzing the SQUID Magnetometer tests. The authors also thank OSU electron microscopy center and ATAMI facility staff and director.

Chapter 3. The Effect of Build Orientation and Heat Treatment on the Corrosion Performance of Additively Manufactured Duplex Stainless Steel 2205

Greg N. Nigon [a,c], Burkan Isgor [b,c], and Somayeh Pasebani [a,c,2]

[a] School of Mechanical, Industrial and Manufacturing Engineering, Oregon State University, Corvallis, OR, 97330

[b] School of Civil and Construction Engineering, Oregon State University, Corvallis, OR, 97330

[c] Advanced Technology and Manufacturing Institute (ATAMI), Corvallis, OR 97330

3.1 Abstract

Duplex stainless steel 2205 components were built via selective laser melting with gas atomized powder (D_{90} <45μm) using a 250 W Laser in nitrogen environment. The relative density was 99.1±0.3%, and the phase ratio after annealing was 53.0/47.0±4.8% ferrite/austenite. Two build orientations (parallel and perpendicular to build direction), as well as as-built (no heat treatment) and annealed conditions were studied. Corrosion properties were characterized in a 3.5% NaCl electrolyte and compared to 2205 wrought alloy. Corrosion rates from linear polarization resistance were < 1 μm/year for all test conditions. As-built conditions showed anisotropic corrosion rates due to preferential crystallographic and grain orientation. Anisotropic behavior was not replicated on annealed conditions, possibly due to complications from porosity and Si/Mn enriched inclusions. No stable pit formation occurred during cyclic polarization tests although the as-built perpendicular and annealed SLM conditions showed metastable pitting, likely due to surface porosity. The as-built specimens in parallel build orientation did not show metastable pitting due to the (110) ferrite texture and grain orientation along the build direction.

Keywords: Selective laser melting, duplex stainless steel, corrosion, annealing, build orientation

[2] Corresponding author (Somayeh Pasebani): e-mail: somayeh.pasebani@oregonstate.edu; phone: +1-541-737-3685

3.2 Introduction

Parts made by additive manufacturing tend to have different microstructures and features than typical wrought material. For example, parts made by selective laser melting (SLM) may have residual porosity, crystallographic texture, and oxide inclusions [86][87][88]. These characteristics also affect the resulting corrosion performance of the additively manufactured alloys. Several potential applications of SLM require corrosion resistance as in the case of clads[89] and pump impellers [9], which are exposed to seawater, and biomedical implants [90–92], which are required to have low metal dissolution in the human body. This paper focuses on the corrosion behavior of duplex stainless steel (DSS) 2205 produced using SLM in simulated seawater environment (i.e., 3.5% NaCl solution). DSS are commonly used in seawater applications where the corrosion performance of cheaper austenitic grades such as 304 and 316 are insufficient [3,33]. However, DSS parts manufactured using SLM have potential challenges with respect to corrosion, which establishes the main motivation of this paper. Their challenges are discussed here.

The microstructure of metals is one of the most important factors affecting their corrosion resistance. DSS as-built components are fully ferritic, rather than ferritic-austenitic [6–8]. After annealing, the duplex microstructure is restored, with up to 46.4% austenite recovered depending on temperature and time [6,8]. The main effect of the recovered microstructure is recovered mechanical properties: before heat treatment, the parts are hard and brittle, and after heat treatment, the ductility increases [6–8]. In wrought alloys, a significant proportion of corrosion failures occur due to non-equilibrium microstructures associated with excess ferrite content in weldments [40,93]. The effect of the phase transformation after annealing in SLM manufactured DSS on the corrosion performance has not been studied extensively. Preliminary work suggested that the as-built parts are vulnerable to pitting attack while the annealed are not [8].

SLM microstructures often suffer from residual porosity due to various factors such as unstable melt flow, lack of fusion, and gases trapped by the keyhole effect [6,54,86,94]. The amount of porosity varies from study to study and depends on the material and processing parameters used. For duplex stainless steel, studies have reported maximum relative densities as low as 90%[6] and as high as 99.97%[8]. The impact of porosity on

corrosion of SLM manufactured alloys has been a topic of study recently. A report on SLM 316 showed that higher porosities caused a higher frequency of metastable pitting, but did not affect the pitting potential [95]. Another study showed that pitting potentials for 316L decreased by ~300 mV when relative density was <99%, and that lack of fusion pores acted as pit initiation sites[96].

Expected chemical composition of the SLM-built parts is another important factor affecting corrosion resistance, especially to pitting corrosion. One quantitative predictor of pitting resistance based on chemical composition is the Pitting Resistance Equivalent Number (PREN) [34] :

$$PREN = \%Cr + 3.3(\%Mo) + 16(\%N) \quad (1)$$

Equation 1 shows that pitting resistance increases with increasing Cr, Mo, and N content. In addition to these three elements, Ni is also known to improve corrosion resistance [30]. There have been reports of elemental vaporization during SLM, effectively reducing the Cr, Mn, and Ni concentrations [61], which could affect the corrosion performance of the manufactured alloys. Minimizing elemental vaporization is important to manufacture an alloy with expected corrosion properties. Additionally, local variations in chemical composition may affect corrosion performance. Segregation of Cr due to the presence of Cr_2N is cited as the cause of poor resistance to pitting corrosion of welded duplex stainless steels [51]. Cr_2N has been identified in as-built components of SLM duplex stainless steel 2205[7].

Parts produced by additive manufacturing, including SLM, are known to have anisotropic mechanical properties as a result of the layer-wise building, high cooling rates, and resulting grain orientations [13][12][97]. The preferred grain orientation in many SLM manufactured alloys will cause different surfaces of the same component to have a different microstructure exposed to the environment. Ultimately these surfaces will have different crystallographic orientations, which may result in anisotropic corrosion properties. Alloys manufactured by rolling have been shown to have anisotropic corrosion properties as a result of their anisotropic microstructures [98,99]. This phenomenon for SLM alloys has received little attention. Preliminary work on IN718 suggested the corrosion performance of a surface may be sensitive to build angle as a result of the differences in the grain boundary area of the exposed surfaces [11]. Outside of SLM, studies have shown for

magnesium and stainless steel that different crystallographic orientations will corrode at different rates[100,101].

This paper is the first in-depth investigation of the corrosion-related challenges of SLM DSS 2205. A two-factor comparison study is presented here on the effect of heat treatment and build orientation. Conditions before and after heat treatment are termed as-built and annealed, respectively. Two different build orientations are studied which produce two test surfaces, one parallel and one perpendicular to build direction. All four conditions (as-built perpendicular (⊥), as-built parallel (∥), annealed perpendicular (⊥), annealed parallel (∥) are compared to wrought material. In the analysis, attention is focused on the influence of chemical composition and porosity in interpreting the results. Both general corrosion resistance, as well as pitting corrosion resistance, are evaluated. Finally, the feasibility of implementing SLM manufactured parts in seawater environments is discussed.

3.3. Experimental Methods

3.3.1 Selective Laser Melting and Subsequent Heat Treatment

Duplex stainless steel 2205 powder was procured from Carpenter Technology Corporation (D_{90} <45μm). Parametric optimization was done on an ORLAS Laser Creator in an inert nitrogen environment. The condition chosen had a relative density measured after heat treatment by the Archimedes method of 99.1±0.3%. Table 1 shows the fixed SLM processing parameters selected.

Table 3.1. Fixed SLM parameters

Parameter	Value	Parameter	Value
Power (W)	187	Scan Speed (mm/s)	800
Layer height (μm)	30	%Oxygen in chamber	<0.01
Line thickness (μm)	50	Samples	10X15 mm cylinders

The chemical composition of the powder was reported by the vendor. The composition of the SLM parts was determined using Energy Dispersive Spectroscopy (EDS). A FEI Quanta 600F environmental SEM equipped with X-Ray Energy Dispersive Spectrometer was used for this purpose.

The heat treatment was 1100 ^{o}C for one hour, followed by a water quench. Determination of phases and preferred orientations was done with a Bruker D8 Discover X-Ray Diffraction (XRD) tool. Phase balance was measured using three different methods. They were optical microscopy of etched samples, electron backscatter diffraction (FEI Quanta 3D), and SQUID magnetometer (scan range -1.2 T to 1.2 T). Sample preparation for microscopy consisted of the polishing sequence of 240 grit, 400 grit, 600 grit, 800 grit, 1200 grit, and 0.05 μm alumina. Etching for optical microscopy consisted of 3 V for 2-4 s with 40% KOH for annealed samples and 6V 120s in 10% oxalic acid for as-built samples.

3.3.2 Corrosion Testing

The corrosion tests were done using a Gamry Reference 3000 potentiostat/FRA in a three-electrode cell containing SLM-manufactured or wrought disks (with an exposed area of 1.15 cm^2) as the working electrode, a saturated calomel electrode (SCE) as the reference electrode, and a graphite rod as the counter electrode. The test electrolyte was 3.5% NaCl solution produced with reagent grade NaCl (99.98%).

Corrosion testing on SLM-manufactured samples was done before and after the full solution anneal, conditions described in this paper as as-built and annealed. Two different surfaces were tested for each condition, perpendicular and parallel to build direction. To obtain the different surfaces, corrosion cylinders were printed in two different build orientations, as shown in Figure 3.1. The samples after printing had a 15 mm diameter and 10 mm thickness. Before corrosion testing, the SLM manufactured cylinders were cut into 2-3 mm thick disks by diamond precision saw. Wrought samples of DSS 2205 were cut with a band saw from a sheet of 2 mm thickness into squares with side lengths of 15 mm and edges were ground until a 15 mm disk was produced. Polishing for SLM and wrought material was done sequentially from 320 grit to 1200 grit SiC followed by a final step with 0.05 μm alumina to completely remove any surface scratches. The polished surfaces were exposed to the electrolyte using a sample holder that is designed to minimize crevice corrosion.

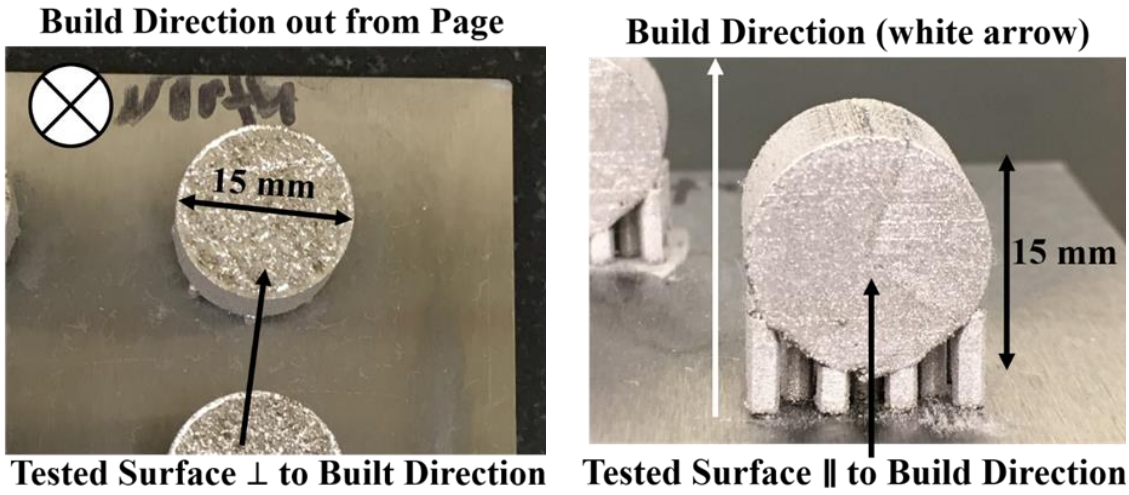

(a) (b)

Figure 3.1. Printed samples (187 W, 800 mm/s) with build orientations such that the surface tested for corrosion was (a) perpendicular and (b) parallel to build direction

The corrosion tests included several techniques that were performed in a sequence. First, open circuit potential (OCP) was monitored for one hour, followed by an electrochemical impedance spectroscopy (EIS) scan. The EIS was performed between the AC frequencies of 50,000 Hz and 0.01 Hz final with 10 measurements per decade. The rms AC voltage amplitude was 5 mV. Following EIS, linear polarization resistance (LPR) test was conducted in the range of ±15mV vs. OCP with a scan rate of 0.166 mV/s per ASTM G61. Following 1800 s of OCP monitoring, the test sequence was concluded with a cyclic polarization (CP) scan between -0.5 V vs. OCP and 0.95 V vs. OCP, with a scan rate of 0.166 mV/s per ASTM G61. The scan range was selected to cover a maximal range of voltage without entering the transpassive regime. The presented EIS, LPR, and CP results were area normalized. The equivalent circuit modeling for EIS data was performed in Gamry Echem Analyst Software (V 6.04).

3.4 Results and Discussion

3.4.1 Microstructure, Crystallographic Orientation, Phases

The microstructure was analyzed with XRD. The as-built parts were fully ferritic, and after annealing, there was a transition to the duplex microstructure (ferrite-austenite) as shown in Figure 3.2.

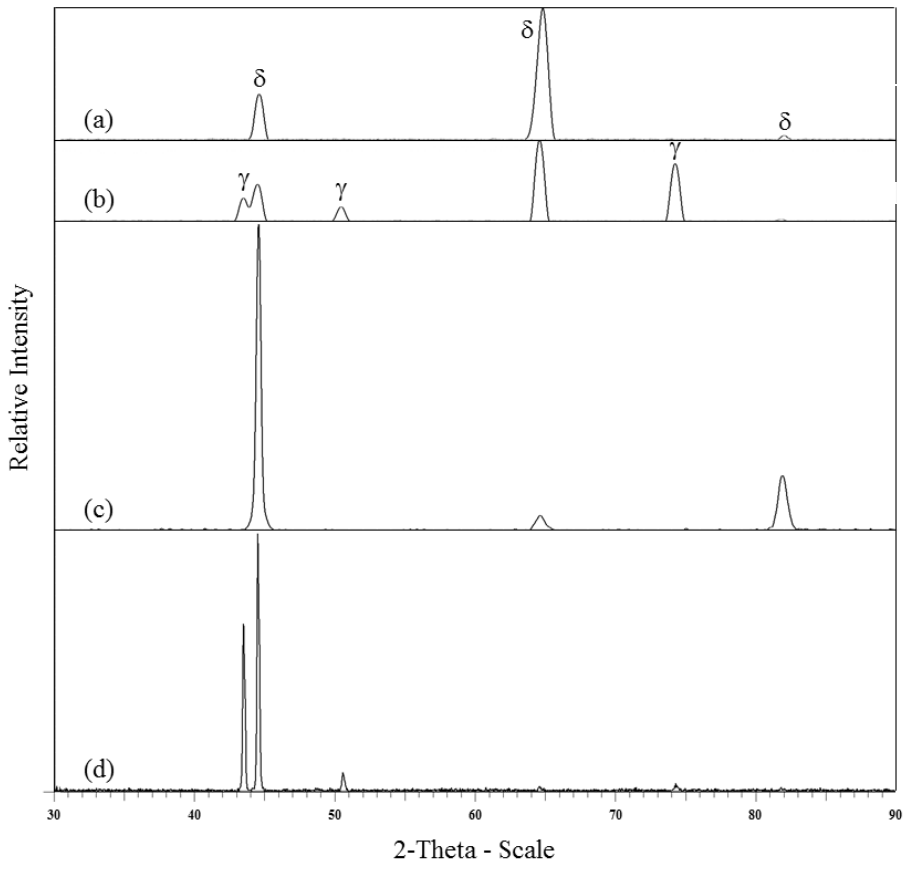

Figure 3.2. The XRD pattern of DSS 2205 processed by SLM at 187W and 800 mm/s (a) as-built perpendicular (b) annealed perpendicular (c) as-built parallel and (d) annealed parallel

Besides showing the phase transition, there was evidence for preferred crystallographic orientations based on relative peak intensities. For the as-built and annealed perpendicular conditions, the second ferritic peak, (200), was far more prevalent than the expectations for a mixed powder sample per the Crystallography Open Database[70]. The relative intensity of this peak was 1 as compared to the relative intensity of 0.128 reported in the database[70]. The preferred orientation for ferrite grains was maintained after annealing. The austenite in the annealed perpendicular condition showed a preferred orientation of (220). The parallel build orientations showed different preferred crystallographic orientations. The as-built parallel condition showed a strong (110) orientation, which was maintained in the ferrite of the annealed parallel sample. The austenite in the annealed parallel condition showed (111) orientation.

Preferred crystallographic orientations have been extensively reported in SLM and are due to grain orientation. In particular, columnar orientations have been observed often

in SLM and have been attributed to directional heat flow into the powder bed[12,13,97,102,103]. However, grains may also orient parallel to the scan direction. Wang et al. discussed these competing grain formation mechanisms in the context of melt pool boundaries[104]. At the "layer-layer" melt pool boundaries (bottom), heat is lost along the build direction, so solidification occurs along the build direction and results in cellular dendrites[104]. At the "track-track" melt pool boundaries (top), maximum heat flux is along the laser scan direction, and the grains orient accordingly[104].

The annealing restored a nearly balanced duplex microstructure. The percent ferrite was measured as 53.0±4.8%. The remainder was austenite. This can be confirmed by observing the phase transformation from optical micrographs, as shown in Figure 3.3. The phase balance met the best results obtained in other studies of SLM duplex stainless steel[6,8]. Prior work has suggested that 1000 ^{o}C annealing yields optimal phase balance for SLM alloys[7,8]. However, those conclusions were based on short five-minute annealing times. Here, a single annealing condition was tested (1100 ^{o}C, 1 hour), and the optimum phase balance was achieved. This suggested that the annealing time may be a more significant factor.

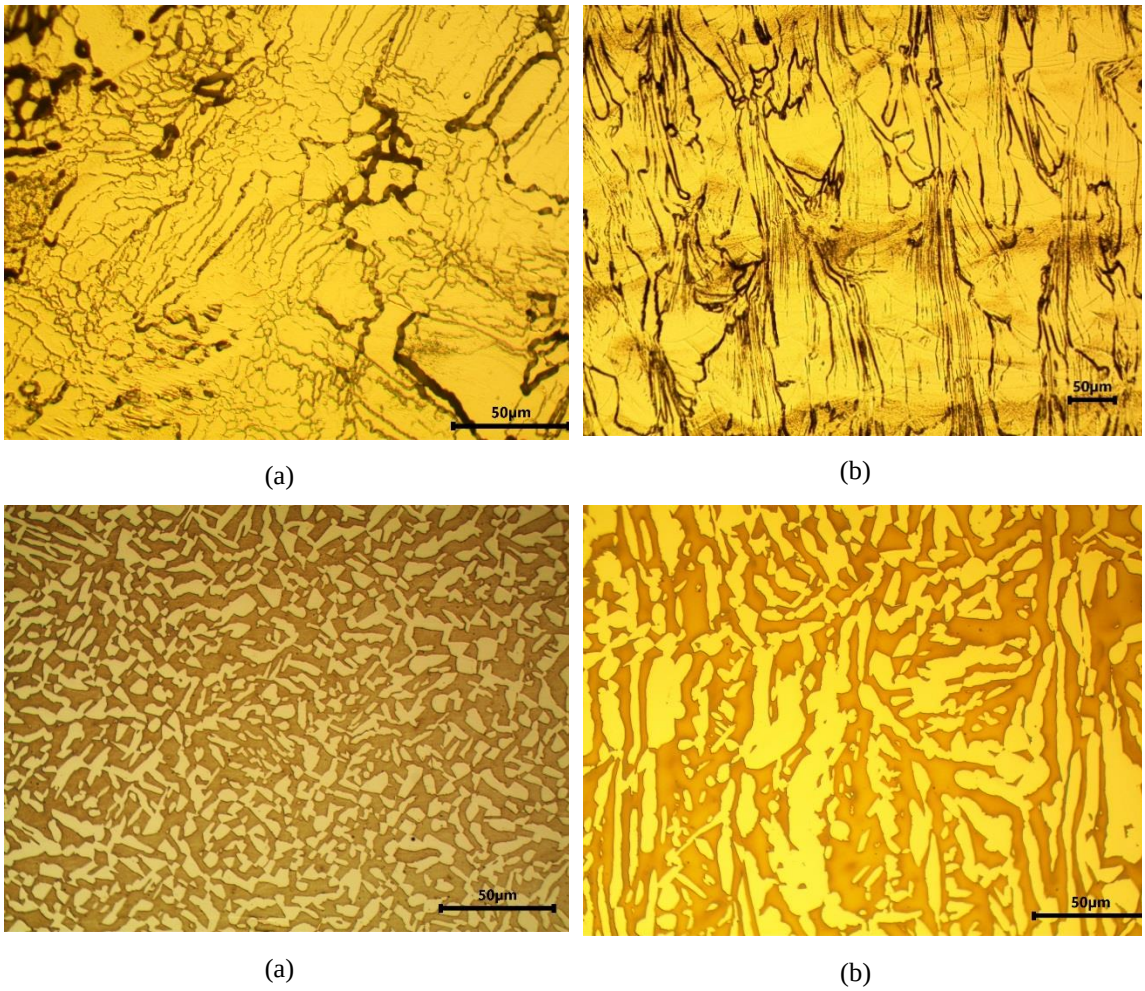

Figure 3.3. Optical micrographs of DSS 2205 processed by SLM at 187W and 800 mm/s
(a) as-built perpendicular (b) as-built parallel (c) annealed perpendicular (d) annealed parallel.
For annealed conditions, ferrite is dark, and austenite is bright.

Per ASTM A890, the ferrite content of a duplex stainless steel cast part should be 30-60% [23]. A study on wrought duplex 2002 (lean) showed the benefits of approaching equal phase balance. A clear trend was observed where slower cooling rates led to higher austenite content, higher critical pitting temperatures, and higher critical pitting potentials [105]. The maximum austenite obtained was ~45%, and this condition showed the best corrosion performance [105]. Several reasons have been put forward for explaining why a balanced, dual-phase microstructure performs better than those with high ferrite content. The most common reason (cited often in welding) is that high cooling rates lead to high ferrite content and precipitation of Cr_2N within the ferrite grains [51,56]. However, a study on super duplex stainless steel suggested the presence of Cr_2N did not adversely affect pitting behavior, as the precipitate size was so small that the Cr depletion zone was not

significant [56]. Cr_2N has been observed in the fully ferritic microstructures of SLM as-built duplex stainless steel 2205 [7]. Another explanation put forward was the relative difference in chemical composition between the ferrite and austenite phases, which was shown to increase as ferrite content increased [106]. The may create a galvanic effect [106].

Another key observation from Figure 3.3 was that the grains of the surfaces parallel to build direction were significantly oriented along the build direction, the underlying reason for the crystallographic orientations shown in Figure 3.2. Heyn lineal intercept procedure[69] for the parallel surfaces yielded an average aspect ratio of 2:1, while for the perpendicular, the measurement yielded 1:1. This elongation along the build direction indicated that the exposed grain boundary area of be the two surfaces (perpendicular and parallel) was likely to be different. It has been suggested that differences in exposed grain boundary area were the cause of differences observed in corrosion potential and corrosion current (E_{corr} and I_{corr}) for SLM IN718 of different build orientations [11]. For example, the authors measured I_{corr} of $0.015\ \mu A/cm^2$ at 0^o build angle (equivalent to the perpendicular nomenclature used in this study) and $0.006\ \mu A/cm^2$ for a 45^o build angle [11]. The atoms at grain boundaries are not as highly bonded as those in bulk, so they would be more susceptible to corrosion.

3.4.2. Residual Porosity

The residual porosity was estimated to be 0.9 ± 0.3 vol. % from the Archimedes Method. For SLM manufactured 316, significant metastable pitting behavior (below critical pitting potential, E_{pit}) occurred with a porosity of 0.4% [95]. Even minor metastable pitting occurred at 0.04% [95]. One specific type of SLM porosity, the lack-of-fusion pore, has been highlighted as a site for pitting attack in 316 [96]. These pores were distinguished by their irregular shape, as opposed to the spherical shape of entrapped gas porosity [96].

The sample to sample variation in porosity, ±0.3%, was significant. This posed an experimental challenge, as it was unknown exactly how the variation in porosity would affect corrosion. All tested conditions in this study, except wrought, contained irregularly shaped pores. Additionally, the size, shape, and distribution of the lack-of-fusion pores were non-uniform. This was important as corrosion is a surface reaction, and the tested samples had surfaces with variable types and levels of porosity. Figure 3.4 shows examples

of different porosities which were present in the samples for the same condition, annealed parallel.

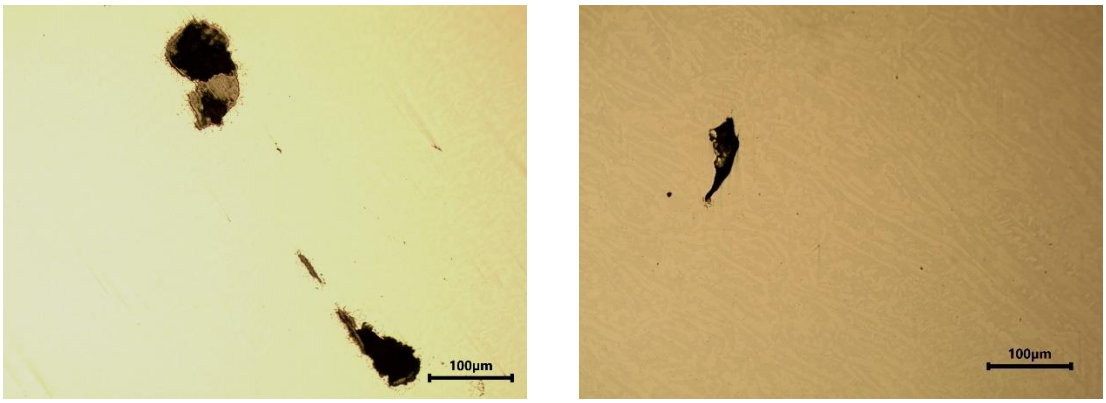

(a) (b)

Figure 3.4. The variation in the level of surface porosity present for the same condition (annealed parallel), but different sample as shown in (a) and (b)

To eliminate lack-of-fusion porosity, it is likely that the power would need to be increased to the 250W used in another study on SLM duplex stainless steel 2205 [8] (not possible in this experiment). Power has been identified as a dominant variable for increasing density [21]. Nevertheless, the bulk porosity obtained here was ~1% and was promising for corrosion resistance.

3.4.3 Chemical Composition

As discussed in the introduction, one of the risks associated with SLM is elemental vaporization. Here, the chemical composition of the SLM parts was consistent with the powder feedstock and DSS 2205 alloys in general. The numerical values can be found in Table 2.

Table 3.2. Chemical composition of powder and SLM built parts

Chemical composition (wt.%)	**Fe**	**Cr**	**Ni**	**Mo**	**Mn**	**Si**
DSS 2205 powder	67.30	22.20	5.40	2.97	1.06	0.68
DSS 2205 as-built	67.10±0.26	22.42±0.10	5.70±0.19	3.29±0.10	0.99±0.10	0.49±0.02
DSS 2205 annealed	67.26±0.21	22.24±0.21	5.76±0.13	3.19±0.11	1.08±0.10	0.46±0.04

The only significant difference in elemental composition between the powder and the SLM alloys was silicon (0.42-0.51 wt.%. in SLM vs. 0.68 wt.% in powder). Silicon concentration in the bulk has not been reported in the literature as having an impact on corrosion properties. Elements known to have an impact on passive film formation and resistance to corrosion (Cr, Ni, and Mo)[30,107] were all within expectations. Nitrogen was not measured in this study. The scan speed of 800 mm/s was likely sufficiently high to prevent overheating of the melt pool and elemental loss, as discussed in a study on 316L clads [89].

Elemental segregation was observed in the SLM manufactured components. In the as-built conditions, Cr was found to segregate. Spot EDS measured 26.87 ± 0.42 wt. % Cr at segregation sites, versus 22.42±0.10 wt. % Cr in bulk. In the annealed conditions, Mn and Si were found to segregate. The Mn and Si measured 4.43±0.85 wt. % and 2.53±0.82 wt. % at segregation sites versus 1.08±0.10 wt. % and 0.46±0.4 wt. % in the bulk. Example locations of segregation sites are shown in Figure 3.5.

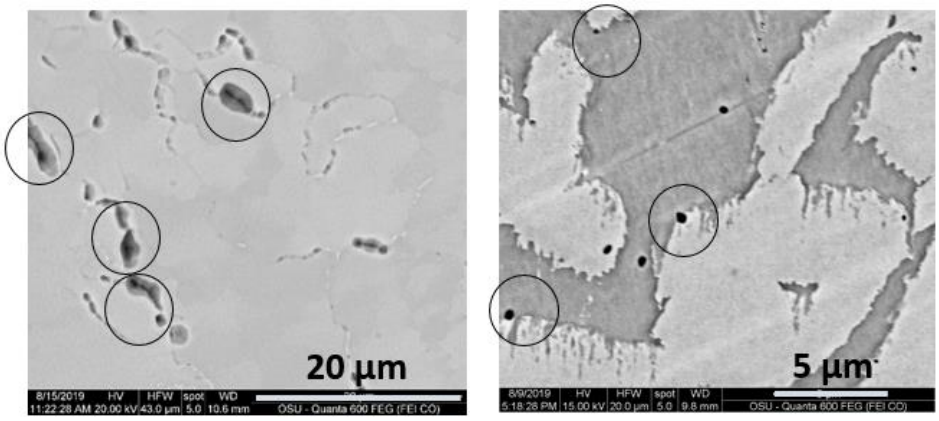

(a) (b)

Figure 3.5. Spot EDS showing segregation site on DSS 2205 processed by SLM at 187W and 800 mm/s (a) as-built and (b) annealed

The elemental segregation found was consistent with reports in prior work. Segregation of Cr was found in SLM DSS 2205 and identified to be from Cr_2N [7]. Segregation of Si and Mn has been commonly reported in SLM 316 and was attributed to the presence of Si and Mn oxides [21,78,88]. The source of oxygen in those studies was likely from the powder feedstock. These factors may influence the corrosion performance.

Inclusions of MnS have been reported as sites of pitting initiation in 300 series stainless steels [108]. The mechanism is uncertain but could be due to the formation of a micro crevice or a microgalvanic coupling [29].

3.4.4. General Corrosion Behavior

The characterization of corrosion properties began with Open Circuit Potential (OCP) monitoring. This allowed for the formation of a stable passive film. Results from representative curves are shown in Figure 3.6. The three dual-phase components (wrought, annealed perpendicular, annealed parallel) began the test with the most negative potentials but increased before stabilizing at -0.130 V.

The as-built perpendicular component decreased OCP at 0.2 hours; however, the repassivation was immediate. The as-built parallel condition had stable OCP from almost the beginning of the test. At the end of the test, all conditions were near -130 mV vs. SCE. This indicated that the passive films which had formed were consistent between the five conditions. The composition of the passive film for duplex stainless steel has been shown to be similar to most stainless steels, although relative amounts of species vary [31]. The passive film for stainless steels generally consists of an inner barrier layer that is rich in Cr_2O_3, CrO_3, Fe_2O_3, and FeO and an outer layer that is rich in $Cr(OH)_3$ and FeOOH [30]. The formation of the passive film during the test was indicated by the increasing OCP (more positive potential, higher passivity).

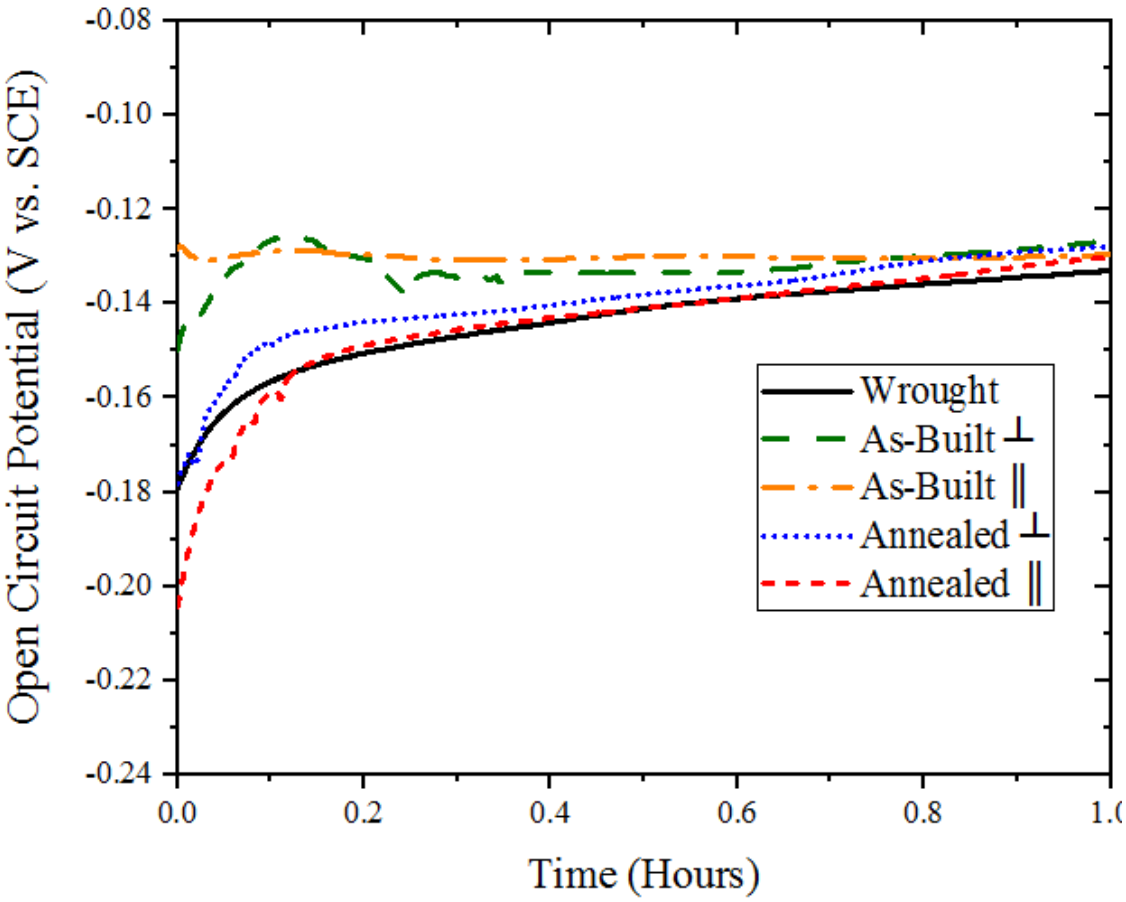

Figure 3.6. Open circuit potential curves for SLM processed duplex stainless steel 2205 (187W, 800 mm/s) and wrought. The drop in the as-built ⊥ curve was measurement noise.

Figure 3.7 shows representative Bode plots for all four SLM conditions (as-built perpendicular, as-built parallel, annealed perpendicular, and annealed parallel) along with wrought. The impedance bode plot (Figure 3.7a) shows the impedance value as a function of frequency. At high frequency, the impedance was reflective of the solution resistance (R_s). In this experiment, the solution was 3.5% NaCl, and the measured R_s was 17.9±0.3 ohm cm^2. As frequency decreased, characteristic features of the electrochemical double layer were probed, specifically R_{ct}, the resistance to passing charge across the double layer, and the capacitive properties of the double-layer [109]. The R_{ct} for stainless steels should be high, assuming the presence of a uniform protective film. The increasing impedance as frequency decreased was reflective of contributions from R_{ct}. From Figure 3.7a, the impedance for all samples was generally similar over the range of frequencies tested, and reasonably high to indicate passivation. However, upon close inspection (inset Figure

3.7a), there were significant differences between the curves at low frequency (0.01 Hz). Wrought and as-built parallel showed the highest impedance (474 and 453 kohm cm.^{2} respectively), the annealed parallel and perpendicular showed median values (377 and 351 kohm cm.^{2}) and the as-built perpendicular showed the lowest (312 kohm cm.^{2}). There were metallurgical factors which could explain the differences in the observed impedance values at low frequencies.

The wrought had no surface porosity, so it was expected that it would perform well. The differences amongst the SLM manufactured samples may be correlated to the preferred grain orientation. Prior work observed that the corrosion rate was sensitive to crystallographic orientation. A study on corrosion of aluminum in NaOH showed corrosion occurred more rapidly on different facets, with most rapid corrosion rates occurring on facets parallel to the (335) planes[110]. These differential corrosion rates were due to the different arrangement of atoms on different planes. Similar work was done recently on the corrosion of magnesium in NaCl solution[100]. This study showed that the basal plane (0001) corroded preferentially[100]. This phenomenon has been observed in stainless steel as well, although the corroding planes vary depending on the crystal structure [101,111]. The general conclusion was that close-packed planes are more resistant to corrosion[101]. For BCC, the (110) plane has the highest planar density, which was the dominant exposed plane for the as-built parallel (Figure 3.2c), which showed higher impedance values (453 kohm cm^2) compared to as-built perpendicular (312 kohm cm.^{2}, (200) orientation). This result was consistent with the experimental observations for polycrystalline BCC iron that (200) planes have higher anodic dissolution rates than the (110) planes [112]. These results came from a study that showed that the pitting potential of API 5L X52 pipeline steel with dominant (110) texture had an E_{pit} 200 mV higher than the same steel with (200) texture.

The anisotropy observed in the as-built components could also be explained from a grain boundary perspective. As discussed earlier and shown in Figure 3.3, the grains were elongated along the build direction, so the exposed grain boundary area of the parallel surfaces would be expected to be lower. Grain boundaries are high energy and are often the locations where elemental segregation occurs, so they are naturally more likely to corrode[29]. Hence, surfaces with higher exposed grain boundaries are more susceptible to corrosion.

Similar corrosion anisotropy remained after annealing, although it was not as significant. This was interesting, as the dominant hkl planes for ferrite and austenite on the annealed parallel cross-section, (110) and (111) have the highest planar density for BCC and FCC respectively. It would be predicted that a similar degree of anisotropy would exist for the annealed compared to the as-built. The reasons for the observed behavior were unclear. One possibility was the observed elemental segregation of Si and Mn. The effect of Si and Mn segregation (likely due to oxide formation[21,78,88]) on the corrosion behavior of SLM components has not been studied in depth. Another factor was the variable sample to sample surface porosity, shown in Figure 3.4. Variable porosity will produce variable surface topographies, which will disrupt the electrochemical double layer and affect the measured impedance results.

Figure 3.7b shows the phase angle bode plot. Important background is that ideal resistors have a 0^o phase angle, while ideal capacitors have a -90^o phase angle[113]. Hence, at high frequencies, when the contribution to impedance was solely R_s, the phase angle was 0^o. As frequency decreased, the phase angle for all conditions reached -85^o, which indicated the capacitive behavior of the double layer. The capacitance of the double layer is indicative of a strong, stable passive film. The results demonstrated that all SLM components were performing well. The as-built parallel condition maintained capacitive behavior over a larger range of frequencies, which indicated a high R_{ct} compared to the other conditions. This was likely due to the same metallurgical factors discussed earlier.

The strong passive film performance of the as-built parallel condition challenged the assumption that the corrosion properties of the dual-phase structure would perform better than the pure ferrite. While poor phase balance has often been cited as the reason for poor corrosion resistance of duplex stainless steel welds, Zhang et al. recently conducted a detailed investigation which showed that precipitation of secondary austenite (Cr depleted) near Cr_2N acted as preferential sites for pitting [51]. Segregation of Cr was observed in the as-built components, but there was no evidence of secondary austenite formation. These results provided more evidence that weld failures in high ferrite content duplex stainless steel are due to Cr depleted austenite, which has been hypothesized in prior work by Hwang and Park [106].

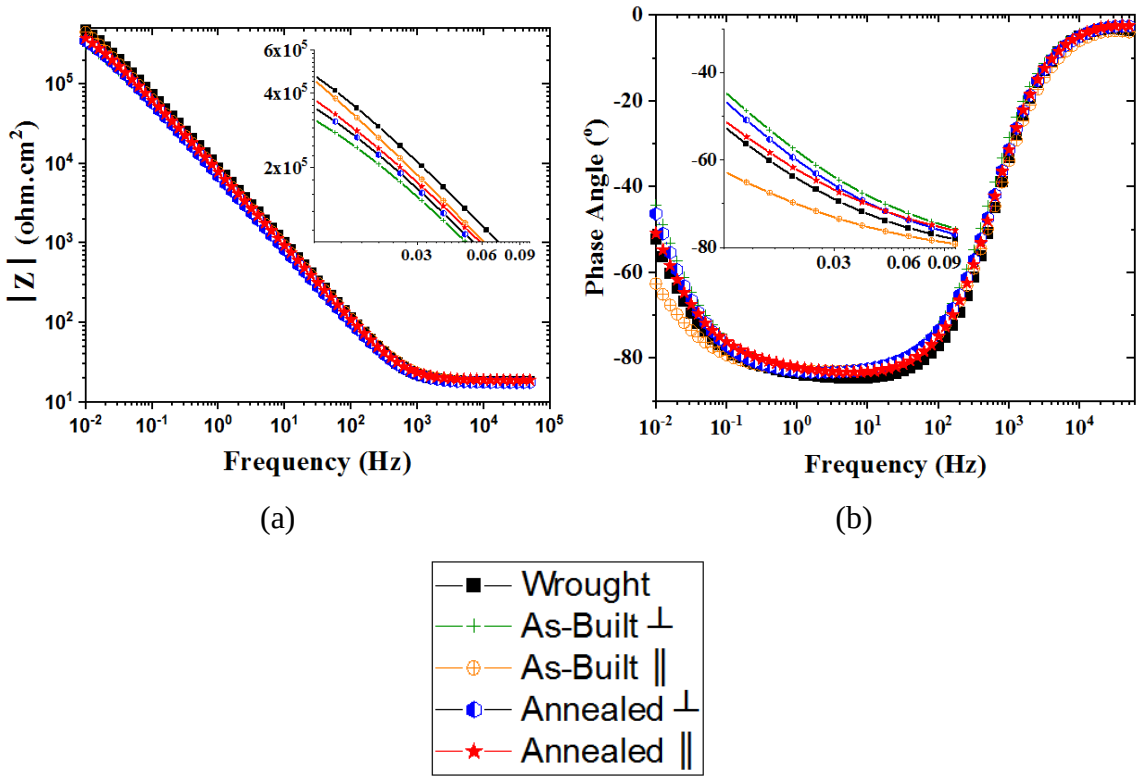

Figure 3.7. EIS data for SLM processed duplex stainless steel 2205 (187W, 800 mm/s) and wrought (a) impedance bode plot (b) phase angle bode plot

The EIS data shown in Figure 3.7 was fit to an equivalent circuit model, specifically the Randles circuit[114]. This circuit consisted of R_s in series with R_{ct}, and a constant phase element (C_{cpe}) in parallel with R_{ct}. The C_{cpe} is an imperfect capacitor and modeled the double-layer capacitance. This circuit has been widely used for modeling corrosion systems[89,115,116]. The calculated parameters are shown in Table 3.

Notable from Table 3 was the parameter α, which was consistently 0.92-0.94 across all conditions. An $\alpha > 0.90$ indicated the passivity of the surface. The calculated values for R_{ct} indicated significant anisotropy in the as-built conditions (1174±46 kohm cm.^{2} for as-built parallel, 469±19 kohm cm.^{2} for as-built perpendicular) and minor anisotropy in the annealed conditions (684±21 kohm cm.^{2} for annealed parallel, 554±13 kohm cm.^{2} for annealed perpendicular). This was likely due to the differences in crystallographic orientation and exposed grain boundary area. The reasons why the annealed conditions did not show as much anisotropy could be due to the Si and Mn segregation or variable

porosity. Additionally, the dual-phase annealed components did not perform quite as well as the dual-phase wrought, likely due to the same defects.

Taken collectively, the average values for R_{ct} were high for all conditions tested. They measured similar to or higher than values reported for wrought 316L (505 kohm cm^2) [89] and wrought super duplex stainless steel (332 kohm $cm.^2$) [117] under identical conditions. This indicated good passivity of the surface. This success was largely an effect of the chemical composition, which was not affected by the processing conditions, and the overall minimization of porosity (~1%). Although detrimental metallurgical effects such as porosity and elemental segregation resulted in variable values between the conditions, there was no clear indication that any condition would perform poorly. This was a promising initial result in terms of implementation in seawater service.

Table 3.3. Parameters for EIS model fitting for SLM processed duplex stainless steel 2205 (187W, 800 mm/s) and wrought in 3.5% NaCl.

Condition	**Avg. R_s (ohm $cm.^2$)**	**R_{ct} (kohm $cm.^2$)**	**C_{CPE}($x10^{-6}$) $ohm^{-1}cm^{-2}s^{\alpha}$**	**α**	**Goodness of fit**
Wrought		811±20	20.7±0.1	0.94±0.01	$8.92x10^{-4}$
As-Built ⊥		469±19	27.3±0.2	0.93±0.01	$2.50x10^{-4}$
As-Built ‖	17.9±0.3	1174±46	23.9±0.1	0.92±0.01	$3.33x10^{-4}$
Annealed ⊥		554±13	26.1±0.1	0.93±0.01	$1.17x10^{-4}$
Annealed ‖		684±21	25.2±0.1	0.93±0.01	$1.39x10^{-3}$

3.4.5 Corrosion Rates

Corrosion rates were calculated from the slope of the Linear Polarization Resistance (LPR) curve (current density vs. potential). Values for the Tafel slopes, β_a, and β_c, were calculated from the respective cyclic polarization curves. The results are shown in Figure 3.8. The as-built conditions showed anisotropic corrosion, which was consistent with the EIS results. However, the annealed conditions showed no anisotropy, and the corrosion rates were not significantly different from the wrought. This inconsistency with the EIS results could be due to the fact that the LPR results were from triplicate samples, so the effects of any processing related variability (such as surface porosity) were more reflected

in the data. It was a promising result and indicated that the general corrosion rates of the annealed conditions in service would be similar to wrought despite the defects.

The anisotropic behavior was confirmed for the as-built conditions. The as-built parallel condition measured the lowest corrosion rate of all samples (0.33±0.10 μm/year), and the as-built parallel condition measured the highest (0.85±0.10 μm/year). As discussed earlier, this was likely due to the differences in crystallographic orientation and exposed grain boundary area. The parallel orientation had planes of (110) preferentially exposed, which have higher planar density than the (200) planes of the perpendicular orientation. The parallel orientations also had grains with a 2:1 aspect ratio along the build direction, which would necessitate a lower exposed grain boundary area than the perpendicular build orientation. The effect of build orientation could not be replicated for the annealed condition, which can be rationalized given the complicating factors such as surface porosities and the presence of Mn/Si enriched inclusions.

A novel finding of this research was that the as-built parallel condition showed improved corrosion resistance over the SLM annealed and wrought counterparts. These results indicated that there was nothing detrimental about a purely ferritic microstructure. Even the as-built perpendicular condition, which only corroded 0.25 μm/year higher than wrought, was not a failure. The as-built parallel condition was able to outperform the wrought due to subtle metallurgical effects from the preferred grain orientation in addition to meeting expectations for bulk chemistry. Some important context is that the dual-phase microstructure is necessary for achieving adequate strength and ductility, which has been shown by authors who worked on SLM duplex stainless steel[7,8].

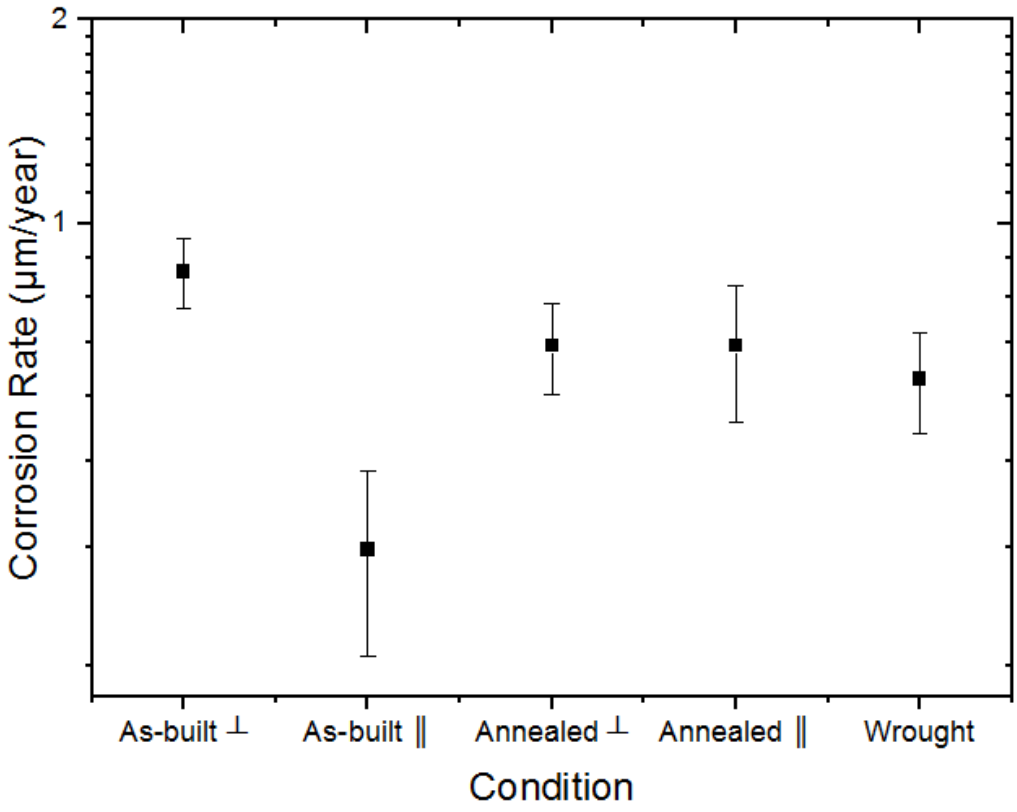

Figure 3.8. Corrosion rates determined from LPR of SLM DSS 2205 processed at 187 W, 800 mm/s and wrought material

3.4.6 Cyclic Polarization (CP)

The results of the CP tests for SLM processed duplex stainless steel 2205 and wrought are shown in Figure 3.9. From Figures 3.9a-b, no conditions tested showed a stable pit formation. The behavior of the SLM processed material was generally comparable to wrought. One exception was the as-built parallel condition, which showed higher corrosion potential (170 mV vs SCE) and repassivation potential (474 mV vs SCE) than wrought (248 mV vs SCE, 418 mV vs SCE). This may have been an effect of the preferred crystallographic orientation and the resistance to anodic dissolution of the (110) ferritic plane. These results were consistent with a study done on Ni-Fe-Cr Alloy 028, which showed that {100} planes are more prone to pitting corrosion than {110} or {111} due to lower atomic packing[118]. They even developed a model to predict pitting resistance based on crystallographic orientation. The annealed parallel condition showed lower corrosion potential (-284 mV vs. SCE) and identical repassivation potential (418 mV vs. SCE) compared to wrought. It would be expected that the annealed parallel would perform

similar to the as-built parallel due to its crystallographic orientation, suggesting the detrimental effect of the Si and Mn inclusions.

Although stable pitting did not occur on any samples tested, metastable pitting occasionally occurred on certain SLM processed conditions. Metastable pitting is an event characterized by the initiation of pitting corrosion due to passive film breakdown (often below critical pitting potential), followed by a period of growth, and finally, cessation of pitting and repair of the passive film[119]. On the CP curve, these were the incidences of a sharp increase in current, followed by a rapid decrease. Select conditions which showed the most metastable pitting are shown in Figure 3.9b. Given that this behavior occurred randomly on SLM as-built and SLM annealed conditions, but not wrought, it was likely that the surface porosities strongly influenced the behavior. Pores have been cited often as the initiation sites for pitting behavior observed in powder metallurgy products [95,120,121]. They are susceptible because of oxygen depletion and local acidification. Other possible initiation sites were the elemental segregation sites of Figure 3.5. It is known that MnS inclusions act as pit initiation sites in 316L[108].

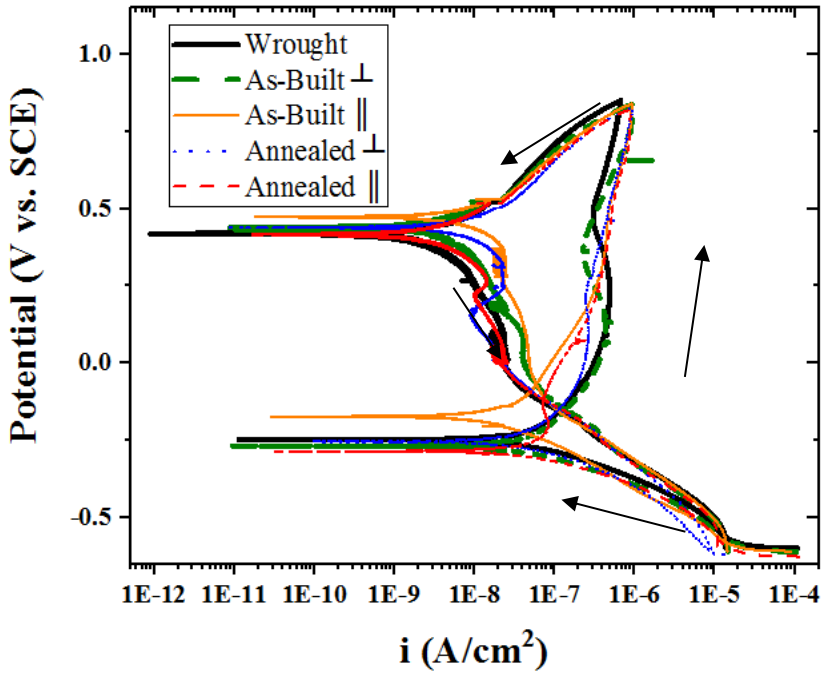

(a)

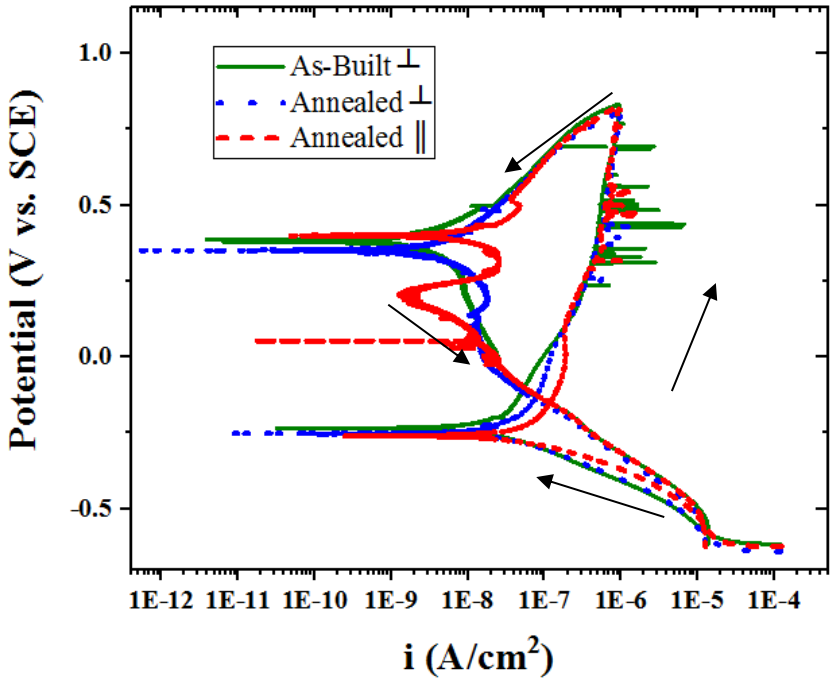

(b)

Figure 3.9. Cyclic polarization curves for (a) SLM processed duplex stainless steel 2205 (187W, 800 mm/s) and wrought in 3.5% NaCl and (b) select experimental runs and conditions which showed metastable pitting. The arrows show the scan direction.

The condition most susceptible to metastable pitting was the as-built perpendicular condition. It recorded the maximum measured current density from a metastable pit event, 10^{-5} A/cm^2, as well as the highest number of metastable pitting events in a single scan (11). The as-built parallel condition showed no metastable pitting, suggesting the strong crystallographic texture affects the resistance to pitting corrosion in addition to general corrosion. It has been shown that the pitting potential of 304 stainless steel is sensitive to crystallographic orientation[111]. High texture index (~35) (200) surfaces had very low pitting potentials (122 mV vs. SCE), while (110) surfaces had high pitting potentials (663 mV vs. SCE)[101].

Both the annealed conditions showed susceptibility to metastable pitting, but the maximum measured current density was only 10^{-6} A/cm^{2,} and the maximum number of events was four. This indicated that there might have been a benefit of the dual-phase microstructure over the single-phase in arresting a pitting event once it has started. The propagation rate of metastable pitting is controlled by factors such as local accumulation of chlorides, local acidification, and diffusion of metal cations out of the pit [119,122]. When considering the perpendicular cross-sections, one basic advantage of the dual-phase is that the number of (200) oriented ferrite grains were essentially decreased by 50%, due to the recrystallization of austenite. As discussed earlier, the (200) BCC planes are more susceptible to dissolution [112]. It was also possible that recrystallization during annealing eliminated the cellular, dendritic microstructures commonly found in SLM materials [12,13,89], which would effectively reduce the number of pathways for grain boundary diffusion of iron.

It was interesting that no steady-state pitting was observed, despite the presence of surface porosities. The most likely explanation was that the passive film was strong, which was reflective of the chemical composition. Poorly selected scan rates (fast) may not allow for sufficient time for pits to grow [29]. In this study, the scan rate was selected as 0.166 mV/s per ASTM G61 [123], and slower scan rates were investigated (0.04 mV/s), which showed no effect. Suitable processing parameters were selected to avoid elemental loss and achieve performance comparable to wrought. However, the presence of metastable pitting raised important concerns about long term service life. A pit that initiates but quickly repassivates would not be of concern. However, it is possible that more aggressive

conditions (high temperatures, more aggressive electrolytes, tight crevices) could create conditions in which the pit would be unable to repassivate. Such a situation may cause an SLM part to fail where a wrought part would not. Future work could be focused on testing more extreme electrolytes.

3.5 Conclusions

Duplex stainless steel 2205 parts were selectively laser melted. Key characteristics were a relative density of 99.1±0.3 %, and a transition from fully ferritic as-built to a dual-phase microstructure after annealing at 1100 ^{o}C for one hour (53.0±4.8% ferrite, austenite remainder). The measured chemical composition of the selectively laser melted and annealed sample, 22.24±0.21 % Cr, 5.76±0.13 % Ni, 3.19±0.11 % Mo, 1.08±0.10 % Mn, and 0.46±0.04 % Si, was consistent with the initial powder feedstock and within expectations for DSS 2205.

The characterization of corrosion properties was subsequently done. As-built and annealed components, at two different build orientations, were tested along with the wrought. The results of LPR and EIS indicated that all conditions were resistant to general corrosion. The corrosion rates calculated from LPR were 0.33±0.10 μm/year and 0.85±0.10 μm/year for as-built parallel and perpendicular build orientation respectively, and 0.66±0.15 μm/year and 0.66±0.10 μm/year for annealed parallel and perpendicular to build direction respectively. The corrosion rate of the wrought sample was 0.59±0.10 μm/year.

Although all alloys performed well, there was an interesting anisotropy observed between the as-built parallel and perpendicular conditions. The as-built parallel condition showed a significantly lower corrosion rate from LPR and higher R_{ct} from EIS (1174±46 kohm cm.^{2} vs. 469±19 kohm cm^2). This was likely due to the different crystallographic orientations. The as-built parallel condition had preferred (110) orientation, while the as-built perpendicular had preferred (200) orientation. Another explanation was the elongation of grains along the build direction (~2:1 aspect ratio), which means that the parallel surfaces would have a lower exposed grain boundary area. Unexpectedly, the SLM annealed samples did not show this anisotropy, as they also maintained preferred orientations. The variable sample to sample surface porosity, the possibility of void formation after annealing, and Mn/Si enriched inclusions could be the reason why a clear trend was not seen.

CP scans were done to determine the resistance to pitting corrosion. Both the wrought and SLM samples showed no evidence of stable pit formation. See Figure 3.9a-b. This was due to the chemical composition and minimization of bulk porosity. However, metastable pitting on the SLM parts was occasionally observed, as shown in Figure 3.9b. It was hypothesized that the local surface porosities were the initiation sites for such behavior. The surface porosities in the samples were not of homogenous size or distribution. Elemental segregation sites could be another possible initiation site. Maximum metastable pitting occurred with the as-built perpendicular condition (up to 10^{-5} A/cm^2 measured in this study), while no metastable pitting was observed on the as-built parallel condition. This was reflective of the anisotropic crystallographic and grain orientation. The annealed conditions behaved isotopically and showed significantly less metastable pitting than the as-built perpendicular condition, with up to 10^{-6} A/cm^2 being measured. Future work would be best focused on corrosion testing in more extreme environments, and on reducing the residual porosity and elemental segregation.

Acknowledgments

The authors would like to thank Pratik Murkute for his valuable input. We acknowledge the funding of critical equipment provided by the Murdock Charitable Trust (Contract number: 2016231:MNL:5/18/2017). G.N thanks Oregon State School of Mechanical, Industrial, and Manufacturing Engineering. The authors thank Professor Albrecht Jander and the OSU Applied Magnetics Laboratory for running and analyzing the SQUID Magnetometer tests. The authors also thank the OSU electron microscopy center and ATAMI facility staff and director.

Chapter 4. Conclusions

4.1 Conclusions

Duplex stainless steel 2205 parts were successfully built via the selective laser melting process. Two subsequent studies were done. The first focused on the additive manufacturing, microstructure, and mechanical properties. The second determined the corrosion performance. Specific characterizations of relative density, chemical composition, grain orientation, and crystallographic texture linked the two studies together. The overarching goal was to evaluate the viability for seawater applications in comparison to the wrought material.

Process parameters were selected to obtain the maximum relative density. In this study, 99.1±0.3% was achieved at 187W, 800 mm/s, 0.03 μm layer thickness, and 0.05 μm hatch spacing. This was not atypical for such a study; however, higher relative densities have been reported. Possible limitations in achieving higher relative density were the power limitation (200W) and inability to preheat the build platform. Nevertheless, a relative density of 99% was high and adequate for meaningful investigations.

The austenitic-ferritic duplex microstructure was recovered using the solution annealing heat treatment of 1100 °C for 1 hr in air atmosphere followed by water quenching. A balanced phase content was achieved, measured by optical image analysis, electron backscatter diffraction, and magnetometer. The results were 53.0±4.8 % ferrite, 51.7±0.7 % ferrite and 55.7 ±1.0 % ferrite respectively. The comparative study of phase analysis highlighted the consistency between methods and indicated that each will yield accurate results. It also opened the door for more extensive use of magnetometer, an automated measurement technique of the bulk phase content (optical microscopy and EBSD are 2D) with almost no sample preparation requirements.

The successful restoration of the austenitic-ferritic microstructure in the annealed condition resulted in a microhardness of 258±8 HV that was comparable to the wrought microhardness of 267±4 HV. However, the ultimate tensile strength of 622±19 MPa and the % elongation of 21.3±1.4 % were inferior to wrought. This was likely due to the residual 1% porosity, which was randomly distributed in the sample. The porosity does not significantly affect microhardness results, however, during a tensile test the pores will act

as crack initiation sites and cause premature failure. For a part manufactured in this methodology, hot isostatic pressing (HIP) could be one option to obtain adequate mechanical properties.

Recovery of the microstructure was expected as the bulk composition was within expectations: there was no elemental vaporization during the print. However, elemental segregation was observed. Key elements which segregated were Cr in the as-built condition (~26% at segregation sites vs ~22% in bulk), and Mn (~4% vs ~1%) and Si (~2% vs ~0.5%) in the annealed condition. Cr may have been present as Cr_2N, which was one factor that explained the brittleness of the as-built samples.

The microstructure, chemical composition, and porosity had minor but interesting effects on the corrosion performance. All tested samples were resistant to general corrosion (comparable to wrought) due to the bulk chemical composition and the overall minimization of porosity. The purely ferritic as-built conditions performed well; in fact, the as-built parallel condition showed the lowest corrosion rates. This suggested that pure ferritic microstructures were not detrimental. Duplex stainless steel weld failures, commonly thought to be caused by excess ferrite, are most likely caused by excessive depletion of Cr in the austenite phases present. No conditions tested showed stable pit formation, but metastable pitting was observed. Compared to the wrought, nearly all SLM conditions showed a higher susceptibility to metastable pitting (the exception being as-built parallel), with up to 10^{-5} A/cm^2 measured during metastable pitting events. This indicated that the porosity and elemental segregation were acting as potential pit initiation sites. A significant research gap lies in understanding the exact mechanism of metastable pit formation and cessation, as well as how metastable pitting behavior would play out during service life. Arguments can be made that it would have no detrimental effect due to the repassivation behavior, but it can also be reasoned that extreme conditions and the presence of tight crevices could lower the service life compared to wrought.

The layer-wise building and $+45^o/-45^o$ scan strategy resulted in a preferred grain orientation. Many grains were orientated along the build direction due to directional heat flow into the powder bed. The measured aspect ratio of the grains was approximately 2:1 for both as-built and annealed. The scan strategy also played a role, as heat will be lost behind the moving beam and thus grains will also solidify along the scan direction. These

orientations were evident when analyzing cross sections perpendicular to build direction. The grains formed a pattern consistent with the +45°/-45° scan tracks.

Preferred grain orientation resulted in crystallographic texture. A strong [001] was found in this study – specifically for the ferrite grains. Cross sections parallel to build direction also showed significant orientation of austenite grains, but there was no [001] texture. The texture of austenite determined from EBSD was mixed with [110] and [001] being dominant. While XRD was consistent for ferrite, for austenite it showed a preferred orientation along [110], and [001] was the least preferred. Austenite nucleation and growth occurred during the heat treatment, so it was difficult to generalize about the directions in which the grains should grow.

The preferred orientation affected the properties of the as-built condition. A higher microhardness was measured on surfaces perpendicular to build direction due to higher exposed grain boundary area from the 2:1 aspect ratio. After the annealing the microhardness anisotropy disappeared.

A similar anisotropy was observed during the corrosion testing. The as-built parallel measured the lowest corrosion across conditions (0.33±0.10 μm/year) while the as-built perpendicular measured the highest (0.85±0.10 μm/year). The metastable pitting behavior of the as-built condition was also sensitive to build orientation. The higher exposed grain boundary area of the perpendicular cross section resulted in higher rates of metastable pit initiation (11 events). The parallel surface showed no metastable pitting. For the annealed samples, the metastable pitting behavior was not sensitive to build orientation. It was greatly diminished compared to the as-built perpendicular (4 events), but still present. There was uncertainty as to why the annealed components did not show anisotropy, given the presence of preferred orientations and grain elongation along the build direction. A possible cause was the prevalence of Si and Mn enriched inclusions, which complicated their behavior. However, the corrosion rates were comparable to wrought (all dual phase conditions ~0.60±0.15 μm/year), so the Si/Mn segregates were not overall diminishing the performance.

Finally, an investigation into the surface roughness of the SLM parts was done. Every sample printed during the optimization rounds showed roughness (5.5-28.6 μm Ra) higher than both the procured wrought (0.3 μm Ra) and the range of typical mill finishes

(0.3-5.0 μm Ra). Roughness may not adversely affect mechanical properties, however for corrosion applications it is widely accepted that higher roughness is detrimental to performance.

The results of the project were promising. However, another stage must be reached before SLM duplex stainless steels could be confidently used in service. The most pressing need is the removal of the residual porosity (possible through hot isostatic pressing) to improve the tensile properties and the reduction in surface roughness. None of these questions and challenges are insurmountable, and there are sure to be opportunities for future work on SLM duplex stainless steels.

4.2 Future Work

The possible directions for future work are discussed briefly here. Potential avenues exist to improve process optimization for even higher density (>99.9%) such as scan strategy and power. HIP treatment and its effect on microstructure would also be worthwhile. An entire study could be devoted to transmission electron microscopy (TEM) on the SLM conditions to analyze the type, composition, and number density of any secondary phases or inclusions present. It may also be possible to find new heat treatments which remove the inclusions. The effect of build orientation on tensile properties would provide a more comprehensive understanding of the anisotropy observed. Given the high surface roughness, there is need to develop a finishing procedure specifically for SLM duplex stainless steels. A deeper understanding of the exceptional corrosion performance of the as-built parallel condition may be informative in designing textures specifically for corrosion applications. Finally, more aggressive electrolytes could be probed to see if stable pit formation occurs on the SLM manufactured components.

REFERENCES

[1] H.D. Solomon, T.M.J. Devine, Duplex Stainless Steels - A Tale of Two Phases, in: R.A. Lula (Ed.), Duplex Stainl. Steel, 1983: pp. 693–756.

[2] Stainless Steel Grade Datasheet, Atlas Steels. (2018). http://www.atlassteels.com.au/site/pages/stainless-steel-datasheets.php.

[3] J. Olsson, M. Snis, Duplex - A new generation of stainless steels for desalination plants, Desalination. 205 (2007) 104–113. https://doi.org/10.1016/j.desal.2006.02.051.

[4] P.K. Gokuldoss, S. Kolla, J. Eckert, Additive manufacturing processes: Selective laser melting, electron beam melting and binder jetting-selection guidelines, Materials (Basel). 10 (2017). https://doi.org/10.3390/ma10060672.

[5] S. Hällgren, L. Pejryd, J. Ekengren, Additive Manufacturing and High Speed Machining -cost Comparison of short Lead Time Manufacturing Methods, Procedia CIRP. 50 (2016) 384–389. https://doi.org/10.1016/j.procir.2016.05.049.

[6] K. Davidson, S. Singamneni, Selective Laser Melting of Duplex Stainless Steel Powders: An Investigation, Mater. Manuf. Process. 31 (2016) 1543–1555. https://doi.org/10.1080/10426914.2015.1090605.

[7] F. Hengsbach, P. Koppa, K. Duschik, M.J. Holzweissig, M. Burns, J. Nellesen, W. Tillmann, T. Tröster, K.P. Hoyer, M. Schaper, Duplex stainless steel fabricated by selective laser melting - Microstructural and mechanical properties, Mater. Des. 133 (2017) 136–142. https://doi.org/10.1016/j.matdes.2017.07.046.

[8] S. Papula, M. Song, A. Pateras, X.-B. Chen, M. Brandt, M. Easton, Y. Yagodzinskyy, I. Virkkunen, H. Hanninen, Selective Laser Melting of Duplex Stainless Steel 2205 : Effect of Post-Processing Heat Treatment on Microstructure, Mechanical Properties, and Corrosion Resistance, Materials (Basel). 12 (2019) 1–15. https://doi.org/10.3390/ma12152468.

[9] M. Huber, M. Hartmann, J. Ess, P. Loeffel, T. Kränzler, R. Rettberg, Process Method for Manufacturing Impellers by Selective Laser Melting (SLM), in: Int. Conf. Addit. Manuf. Prod. Appl. ETH, Sulzer, Zürich, Switzerland, 2017. https://www.sulzer.com/en/shared/about-us/2018/04/11/10/22/white-paper-2-2018.

[10] J.P. Kruth, G. Levy, F. Klocke, T.H.C. Childs, Consolidation phenomena in laser and powder-bed based layered manufacturing, CIRP Ann. - Manuf. Technol. 56 (2007) 730–759. https://doi.org/10.1016/j.cirp.2007.10.004.

[11] D. Du, A. Dong, D. Shu, G. Zhu, B. Sun, X. Li, E. Lavernia, Influence of build orientation on microstructure, mechanical and corrosion behavior of Inconel 718 processed by selective laser melting, Mater. Sci. Eng. A. 760 (2019) 469–480. https://doi.org/10.1016/j.msea.2019.05.013.

[12] T. Niendorf, S. Leuders, A. Riemer, H.A. Richard, D. Schwarze, Highly Anisotropic Steel Processed by Selective Laser Melting, Metall. Mater. Trans. 44B (2013) 794–796. https://doi.org/10.1007/s11663-013-9875-z.

[13] L. Hitzler, J. Hirsch, B. Heine, M. Merkel, W. Hall, A. Öchsner, On the Anisotropic Mechanical Properties of Selective Laser-Melted Stainless Steel, Materials (Basel). 1136 (2017) 1–19. https://doi.org/10.3390/ma10101136.

[14] Duplex Stainless Steel - A Simplified Guide, Br. Stainl. Steel Assoc. (n.d.). https://www.bssa.org.uk/topics.php?article=668.

[15] Practical Guidelines for the Fabrication of Duplex Stainless Steel, 3rd ed., International Molybdenum Association, 2014.

[16] T.H. Chen, J.R. Yang, Microstructural characterization of simulated heat affected zone in a nitrogen-containing 2205 duplex stainless steel, Mater. Sci. Eng. A. 338 (2002) 166–181. https://doi.org/10.1016/S0921-5093(02)00065-5.

[17] J. Komi, Hot Ductility of Austenitic and Duplex Stainless Steels Under Hot Rolling Conditions, University of Oulu, 2001.

[18] C.-C. Hsieh, W. Wu, Precipitation of Phase Using General Diffusion Equation with Comparison to Vitek Diffusion Model in Dissimilar Stainless Steels, J. Metall. 2012 (2012) 1–7. https://doi.org/10.1155/2012/154617.

[19] R. Smallman, A. Ngan, Physical Metallurgy and Advanced Materials, 7th ed., Elsevier Ltd, 2007.

[20] TWI, Austenite Martensite Bainite Pearlite and Ferrite Structures, TWI Ltd. (2020). https://www.twi-global.com/technical-knowledge/faqs/faq-what-are-the-microstructural-constituents-austenite-martensite-bainite-pearlite-and-ferrite (accessed February 2, 2020).

[21] C. Qiu, M. Al Kindi, A.S. Aladawi, I. Al Hatmi, A comprehensive study on microstructure and tensile behaviour of a selectively laser melted stainless steel, Sci. Rep. 8 (2018) 1–16. https://doi.org/10.1038/s41598-018-26136-7.

[22] J. Sakai, I. Matsushima, Y. Kamemura, E. Al., Effects of Metallurgical Factors on Service Performance of Duplex Stainless Steel for Deep Sour Gas Well, in: R.A. Lula (Ed.), Duplex Stainl. Steel, 1983: pp. 211–231.

[23] ASTM International, ASTMA890/A890M-18a, United States, n.d. https://compass.astm.org/EDIT/html_annot.cgi?A890+18a#s00015.

[24] A. Momeni, K. Dehghani, X. Zhang, Mechanical and Microstructural Analysis of 2205 duplex stainless steel under hot working condition, J. Mater. Process. Technol. 47 (2012) 2966–2974. https://doi.org/10.1007/s10853-011-6130-3.

[25] R. Magnabosco, Kinetics of Sigma Phase Formation in Duplex Stainless Steel, Mater. Res. 12 (2009) 321–327. https://doi.org/http://dx.doi.org/10.1590/S1516-14392009000300012.

[26] ASTM, ASTM A790 - Seamless and Welded Ferritic/Austenitic Stainless Steel Pipe, Astm. (2015) 1–9. https://doi.org/10.1520/A0790.

[27] Z. Schulz, Availability and Economics of using Duplex Stainless Steel, in: Corros. 2014, San Antonio, TX, 2014.

[28] J.O. Nilsson, Duplex Stainless Steels - An Interplay between Austenite and Ferrite, Stainl. Steel World Mag. (2017). https://www.materials.sandvik/en-us/news-media/news-and-stories/archive/2017/11/duplex-stainless-steels-an-interplay-between-ferrite-and-austenite/.

[29] D.A. Jones, Principles and Prevention of Corrosion, 2nd ed., Prentice Hall, 1996.

[30] W. Fredriksson, Depth Profile of the Passive Layer on Stainless Steel using Photoelectron Spectroscopy, Acta Univ. Ups. 955 (2012) 1–70.

[31] J. Yao, D.D. Macdonald, C. Dong, Passive film on 2205 duplex stainless steel studied by photo-electrochemistry and ARXPS methods, Corros. Sci. 146 (2019) 221–232. https://doi.org/10.1016/j.corsci.2018.10.020.

[32] Y. Hu, Y. Li, Y. He, J. Wang, X. Liu, Y. Zhang, P. Han, Effects of micro-sized ferrite and austenite grains on the pitting corrosion behavior of lean duplex stainless steel 2101, Metals (Basel). 7 (2017). https://doi.org/10.3390/met7050168.

[33] S.J. Morrow, Materials Selection for Seawater Pumps, in: Proc. 26th Int. Pump Users Symp., 2010: pp. 73–80.

[34] J. Charles, Corrosion Properties, in: I. Alvares-Armas, S. Degallaix-Moreuil (Eds.), Duplex Stainl. Steel, 2009: pp. 47–114.

[35] Duplex Grades, Outokempo. (2018). https://www.nace.org/Corrosion-Central/Corrosion-101/Stress-Corrosion-Cracking-(SCC)/.

[36] Stress Corrosion Cracking, NACE Int. (n.d.). https://www.nace.org/Corrosion-Central/Corrosion-101/Stress-Corrosion-Cracking-(SCC)/.

[37] S. Bernhardsson, J. Oredsson, C. Martenson, The Stress Corrosion Cracking Resistance of Duplex Stainless Steels in Chloride Environments, in: R.A. Lula (Ed.), Duplex Stainl. Steel, 1983: pp. 267–283.

[38] No Title, Sandmeyer Steel Co. (n.d.). https://www.sandmeyersteel.com/SSC-6MO.html.

[39] R. Chaves, I. Costa, H.G. De Melo, S. Wolynec, Evaluation of selective corrosion in UNS S31803 duplex stainless steel with electrochemical impedance spectroscopy, Electrochim. Acta. 51 (2006) 1842–1846. https://doi.org/10.1016/j.electacta.2005.02.105.

[40] C.R. de Farias Azevedo, H. Boschetti Pereira, S. Wolynec, A.F. Padilha, An overview of the recurrent failures of duplex stainless steels, Eng. Fail. Anal. (2019) 161–188. https://doi.org/10.1016/j.engfailanal.2018.12.009.

[41] Y. Tang, N. Dai, J. Wu, Y. Jiang, J. Li, Investigation of influence of surface roughness on pitting corrosion of duplex stainless steel 2205 using various electrochemical techniques, Int. J. Electrochem. Sci. 14 (2019) 6790–6813. https://doi.org/10.20964/2019.07.51.

[42] L. Chen, F.P. Yuan, P. Jiang, J.J. Xie, X.L. Wu, Simultaneous improvement of tensile strength and ductility in micro-duplex structure consisting of austenite and ferrite, Mater. Sci. Eng. A. 618 (2014) 563–571. https://doi.org/10.1016/j.msea.2014.09.014.

[43] S. Wen, C. Lundin, G. Batten, Metallurgical Evaluation of Cast Duplex Stainless Steels and Their Weldments, US Dep. Energy. 1 (2005) 221.

[44] S. Martin, G. Mooren, A. Holtz, Centrifugally Cast Duplex Stainless Steel:

Discussion of Benefits, n.d.

[45] S. Jayet-Gendrot, P. Gilles, C. Migne, Behavior of duplex, stainless steel casting defects under mechanical loadings, Nucl. Eng. Des. (2000) 141–153. https://doi.org/10.1016/s0140-6701(00)96450-6.

[46] S.O. Seidu, A. Onigbajumo, Effect of casting wall thickness and pouring temperature on residual stress build up in aluminum 6063 casting, Federal University of Technology, n.d. http://ljs.academicdirect.org/A29/148_160.htm.

[47] C.A. Clark, P. Guha, Welding Characteristics of Duplex Steels, in: R.A. Lula (Ed.), Duplex Stainl. Steel, 1983: pp. 631–647.

[48] A.H.I. Mourad, A. Khourshid, T. Sharef, Gas tungsten arc and laser beam welding processes effects on duplex stainless steel 2205 properties, Mater. Sci. Eng. A. 549 (2012) 105–113. https://doi.org/10.1016/j.msea.2012.04.012.

[49] I. Alvarez-Armas, S. Degallaix-Moreuil, Duplex Stainless Steels, ISTE Ltd. and John Wiley and Sons, 2009.

[50] Jinsun Liao, Nitride Precipitation in Weld HAZs of a Duplex Stainless Steel, ISIJ Int. 41 (2001) 460–467. https://www.jstage.jst.go.jp/article/isijinternational1989/41/5/41_5_460/_pdf/-char/en.

[51] Z. Zhang, H. Jing, L. Xu, Y. Han, L. Zhao, J. Zhang, Influence of microstructure and elemental partitioning on pitting corrosion resistance of duplex stainless steel welding joints, Appl. Surf. Sci. 394 (2017) 297–314. https://doi.org/10.1016/j.apsusc.2016.10.047.

[52] M. Utrilla, Influence of Heat Treatments on the Corrosion Resistance of Duplex Stainless Steel Manufactured by Powder Metallurgy, NACE Corros. 62 (2006) 84–89.

[53] L.A. Dobrzañski, Z. Brytan, M.A. Grande, M. Rosso, Properties of duplex stainless steels made by powder metallurgy, Arch. Mater. Sci. Eng. 28 (2007) 217–223.

[54] K.P. Davidson, S.B. Singamneni, Metallographic evaluation of duplex stainless steel powders processed by selective laser melting, Rapid Prototyp. J. 23 (2017) 1146–1163. https://doi.org/10.1108/RPJ-04-2016-0053.

[55] U. Scipioni Bertoli, A.J. Wolfer, M.J. Matthews, J.P.R. Delplanque, J.M.

Schoenung, On the limitations of Volumetric Energy Density as a design parameter for Selective Laser Melting, Mater. Des. 113 (2017) 331–340. https://doi.org/10.1016/j.matdes.2016.10.037.

[56] N. Pettersson, R.F.A. Pettersson, S. Wessman, Precipitation of Chromium Nitrides in the Super Duplex Stainless Steel 2507, Metall. Mater. Trans. A Phys. Metall. Mater. Sci. 46 (2015) 1062–1072. https://doi.org/10.1007/s11661-014-2718-y.

[57] Fresh Water for the Future Desalination Made Efficient, KSB Inc. (2014) 1–24.

[58] K.N. Amato, S.M. Gaytan, L.E. Murr, E. Martinez, P.W. Shindo, Microstructures and mechanical behavior of Inconel 718 fabricated by selective laser melting, Acta Mater. 60 (2012) 2229–2239. https://doi.org/10.1016/j.actamat.2011.12.032.

[59] Y. Tang, N. Dai, J. Wu, Y. Jiang, J. Li, Effect of Surface Roughness on Pitting Corrosion of 2205 Duplex Stainless Steel Investigated by Electrochemical Noise Measurements, Mater. Charact. 131 (2019) 181–194. https://doi.org/10.3390/ma12050738.

[60] A. Leon, E. Aghion, Effect of surface roughness on corrosion fatigue performance of AlSi10Mg alloy produced by Selective Laser Melting (SLM), Mater. Charact. 131 (2017) 188–194. https://doi.org/10.1016/j.matchar.2017.06.029.

[61] M. Yakout, M.A. Elbestawi, S.C. Veldhuis, A study of thermal expansion coefficients and microstructure during selective laser melting of Invar 36 and stainless steel 316L, Addit. Manuf. 24 (2018) 405–418. https://doi.org/10.1016/j.addma.2018.09.035.

[62] Mastersizer 3000, Malvern Panalytical. (2019). https://www.malvernpanalytical.com/en/products/product-range/mastersizer-range/mastersizer-3000 (accessed January 3, 2020).

[63] A.A. Bartlett, Demonstration of a crystalline phase change in a solid, Phys. Teach. 13 (1975) 545–547. https://doi.org/10.1119/1.2339261.

[64] C.T. Rueden, J. Schindelin, M.C. Hiner, ImageJ2: ImageJ for the next generation of scientific image data, BMC Bioinformatics. 18 (2017). https://doi.org/10.1186/s12859-017-1934-z.

[65] J. Schindelin, I. Arganda-Carreras, E. Frise, Fiji: an open-source platform for biological-image analysis, Nat. Methods. 9 (2012) 676–682.

https://doi.org/10.1038/nmeth.2019.

[66] W. Elmer, T.W. Eagar, Measuring the residual ferrite content of rapidly solidified stainless steel alloys, Weld. J. 69 (1990) 141s–50s.

[67] A. Forgas Júnior, J. Otubo, R. Magnabosco, Ferrite quantification methodologies for duplex stainless steel, J. Aerosp. Technol. Manag. 8 (2016) 357–362. https://doi.org/10.5028/jatm.v8i3.653.

[68] B. Moskowitz, Classes of Magnetic Materials, Environ. Magn. Work. (1991). http://www.irm.umn.edu/hg2m/hg2m_b/hg2m_b.html (accessed December 20, 2019).

[69] E. Heyn, The Metallographist, 5 (1903) 39–64.

[70] S. Grazulis, D. Chateigner, R.T. Downs, A.T. Yokochi, M. Quiros, L. Lutterotti, E. Manakova, J. Butkus, P. Moeck, A. Le Bail, Crystallography Open Database - an open access collection of crystal structures, J. Appl. Crystallogr. 42 (2009) 726–729.

[71] B.D. Cullity, S.R. Stock, Elements of X-Ray Diffraction, 3rd ed., Prentice Hall, 2001.

[72] R.L. Carr, Evaluating Flow Properties of Solids, Chem. Eng. 72 (1965) 163–168.

[73] A. Thanki, W. Dewulf, A. Witvrouw, S. Yang, Study of keyhole-porosities in selective laser melting using X-ray computed tomography, ICT19. (2019) 1–7. https://doi.org/10.13140/RG.2.2.14592.07684.

[74] K.G. Prashanth, S. Scudino, T. Maity, J. Das, J. Eckert, Is the energy density a reliable parameter for materials synthesis by selective laser melting?, Mater. Res. Lett. 5 (2017) 386–390. https://doi.org/10.1080/21663831.2017.1299808.

[75] R. Saluja, K.M. Moeed, Depiction of Detrimental Metallurgical Effects in Grade 304 Austenitic Stainless Steel Arc Welds, Int. J. Mech. Prod. Eng. Res. Dev. 8 (2018) 207–218.

[76] J.C. De Lacerda, L.C. Cândido, L.B. Godefroid, Effect of volume fraction of phases and precipitates on the mechanical behavior of UNS S31803 duplex stainless steel, Int. J. Fatigue. 74 (2015) 81–87. https://doi.org/10.1016/j.ijfatigue.2014.12.015.

[77] R.W. Balluffi, S.M. Allen, W.C. Carter, Kinetics of Materials, Wiley, Interscience, 2005.

[78] M. Ghayoor, K. Lee, Y. He, C. Chung, B. Paul, S. Pasebani, Microstructural

Analysis of Additively Manufactured 304L Stainless Steel Oxide Dispersion Strengthened Alloy, Microsc. Microanal. 25 (2019) 2594–2595. https://doi.org/10.1017/S1431927619013709.

[79] H.J.T. Ellingham, Reducibiity of Oxides and Sulphides in Metallurgical Processes, J. Soc. Chem. Ind. 63 (1944). https://doi.org/10.1002/jctb.5000630501.

[80] O. Dmitrieva, D. Ponge, G. Inden, J. Millán, P. Choi, J. Sietsma, D. Raabe, Chemical gradients across phase boundaries between martensite and austenite in steel studied by atom probe tomography and simulation, Acta Mater. 59 (2011) 364–374. https://doi.org/10.1016/j.actamat.2010.09.042.

[81] M. Tariq, Interdiffusion of manganese in austenitic and ferritic CrNi Steels, Cryst. Res. Technol. 23 (1988) 1503–1515.

[82] C. Ni, Y. Shi, J. Liu, Effects of inclination angle on surface roughness and corrosion properties of selective laser melted 316L stainless steel, Mater. Res. Express. 6 (2019). https://doi.org/10.1088/2053-1591/aaf2d3.

[83] A.H. Maamoun, Y.F. Xue, M.A. Elbestawi, S.C. Veldhuis, Effect of selective laser melting process parameters on the quality of Al alloy parts: Powder characterization, density, surface roughness, and dimensional accuracy, Materials (Basel). 11 (2018). https://doi.org/10.3390/ma11122343.

[84] Y. Liu, Y. Yang, S. Mai, D. Wang, C. Song, Investigation into spatter behavior during selective laser melting of AISI 316L stainless steel powder, Mater. Des. 87 (2015) 797–806. https://doi.org/10.1016/j.matdes.2015.08.086.

[85] A.P. Systems, Surface Textures Of Stainless Steels, Focus Tech. (n.d.) 1–2. https://www.eirichusa.com/images/downloads/downloads-page/APS Downloads/APS Product Brochures/Surface Textures of SS_TF.pdf (accessed December 16, 2019).

[86] C. Qiu, C. Panwisawas, M. Ward, H.C. Basoalto, J.W. Brooks, M.M. Attallah, On the role of melt flow into the surface structure and porosity development during selective laser melting, Acta Mater. 96 (2015) 72–79. https://doi.org/10.1016/j.actamat.2015.06.004.

[87] L. Thijs, K. Kempen, J.P. Kruth, J. Van Humbeeck, Fine-structured aluminium products with controllable texture by selective laser melting of pre-alloyed

AlSi10Mg powder, Acta Mater. 61 (2013) 1809–1819. https://doi.org/10.1016/j.actamat.2012.11.052.

[88] X. Lou, P.L. Andresen, R.B. Rebak, Oxide inclusions in laser additive manufactured stainless steel and their effects on impact toughness and stress corrosion cracking behavior, J. Nucl. Mater. 499 (2018) 182–190. https://doi.org/10.1016/j.jnucmat.2017.11.036.

[89] P. Murkute, S. Pasebani, O.B. Isgor, Production of corrosion-resistant 316L stainless steel clads on carbon steel using powder bed fusion-selective laser melting, J. Mater. Process. Technol. 273 (2019). https://doi.org/10.1016/j.jmatprotec.2019.05.024.

[90] A. Dehghanghadikolaei, H. Ibrahim, A. Amerinatanzi, M. Hashemi, N.S. Moghaddam, M. Elahinia, Improving corrosion resistance of additively manufactured nickel–titanium biomedical devices by micro-arc oxidation process, J. Mater. Sci. 54 (2019) 7333–7355. https://doi.org/10.1007/s10853-019-03375-1.

[91] D. Zhao, C. Han, Y. Li, J. Li, K. Zhou, Q. Wei, J. Liu, Y. Shi, Improvement on mechanical properties and corrosion resistance of titanium-tantalum alloys in-situ fabricated via selective laser melting, J. Alloys Compd. 804 (2019) 288–298. https://doi.org/10.1016/j.jallcom.2019.06.307.

[92] B. Zhao, H. Wang, N. Qiao, C. Wang, M. Hu, Corrosion resistance characteristics of a Ti-6Al-4V alloy scaffold that is fabricated by electron beam melting and selective laser melting for implantation in vivo, Mater. Sci. Eng. C. 70 (2017) 832–841. https://doi.org/10.1016/j.msec.2016.07.045.

[93] Z. Zhang, H. Jing, L. Xu, Y. Han, L. Zhao, C. Zhou, Effects of nitrogen in shielding gas on microstructure evolution and localized corrosion behavior of duplex stainless steel welding joint, Appl. Surf. Sci. 404 (2017) 110–128. https://doi.org/10.1016/j.apsusc.2017.01.252.

[94] K. V. Yang, P. Rometsch, T. Jarvis, J. Rao, S. Cao, C. Davies, X. Wu, Porosity formation mechanisms and fatigue response in Al-Si-Mg alloys made by selective laser melting, Mater. Sci. Eng. A. 712 (2018) 166–174. https://doi.org/10.1016/j.msea.2017.11.078.

[95] G. Sander, S. Thomas, V. Cruz, M. Jurg, N. Birbilis, X. Gao, M. Brameld, C.R.

Hutchinson, On the corrosion and metastable pitting characteristics of 316l stainless steel produced by selective laser melting, J. Electrochem. Soc. 164 (2017) C250–C257. https://doi.org/10.1149/2.0551706jes.

[96] M. Laleh, A.E. Hughes, S. Yang, J. Li, W. Xu, I. Gibson, M.Y. Tan, Two and three-dimensional characterisation of localised corrosion affected by lack-of-fusion pores in 316L stainless steel produced by selective laser melting, Corros. Sci. (2019) 108394. https://doi.org/10.1016/j.corsci.2019.108394.

[97] M. Ni, C. Chen, X. Wang, P. Wang, R. Li, X. Zhang, K. Zhou, Anisotropic tensile behavior of in situ precipitation strengthened Inconel 718 fabricated by additive manufacturing, Mater. Sci. Eng. A. 701 (2017) 344–351. https://doi.org/10.1016/j.msea.2017.06.098.

[98] F.X. Song, X.M. Zhang, S.D. Liu, N.M. Han, D.F. Li, Anisotropy of localized corrosion in 7050-T7451 Al alloy thick plate, Trans. Nonferrous Met. Soc. China (English Ed. 23 (2013) 2483–2490. https://doi.org/10.1016/S1003-6326(13)62758-2.

[99] W. Zhang, G.S. Frankel, Anisotropy of localized corrosion in AA2024-T3, Electrochem. Solid-State Lett. 3 (2000) 268–270. https://doi.org/10.1149/1.1391121.

[100] L.G. Bland, K. Gusieva, J.R. Scully, Effect of Crystallographic Orientation on the Corrosion of Magnesium: Comparison of Film Forming and Bare Crystal Facets using Electrochemical Impedance and Raman Spectroscopy, Electrochim. Acta. 227 (2017) 136–151. https://doi.org/10.1016/j.electacta.2016.12.107.

[101] S. Krishnan, J. Dumbre, S. Bhatt, E.T. Akinlabi, R. Ramalingam, Effect of Crystallographic Orientation on the Pitting Corrosion Resistance of Laser Surface Melted AISI 304L Austenitic Stainless Steel, Int. Sch. Sci. Res. Innov. 7 (2013) 650–653.

[102] J. Yin, G. Peng, C. Chen, J. Yang, H. Zhu, L. Ke, Z. Wang, D. Wang, M. Ma, G. Wang, X. Zeng, Thermal behavior and grain growth orientation during selective laser melting of Ti-6Al-4V alloy, J. Mater. Process. Technol. 260 (2018) 57–65. https://doi.org/10.1016/j.jmatprotec.2018.04.035.

[103] X. Zhou, K. Li, D. Zhang, X. Liu, J. Ma, W. Liu, Z. Shen, Textures formed in a

CoCrMo alloy by selective laser melting, J. Alloys Compd. 631 (2015) 153–164. https://doi.org/10.1016/j.jallcom.2015.01.096.

[104] M. Wang, H. Li, Y. Tian, H. Guo, X. Fang, Y. Guo, Evolution of grain interfaces in annealed duplex stainless steel after parallel cross rolling and direct rolling, Materials (Basel). 11 (2018) 1–15. https://doi.org/10.3390/ma11050816.

[105] Y. Guo, T. Sun, J. Hu, Y. Jiang, L. Jiang, J. Li, Microstructure evolution and pitting corrosion resistance of the Gleeble-simulated heat-affected zone of a newly developed lean duplex stainless steel 2002, J. Alloys Compd. 658 (2016) 1031–1040. https://doi.org/10.1016/j.jallcom.2015.10.218.

[106] H. Hwang, Y. Park, Effects of Heat Treatment on the Phase Ratio and Corrosion Resistance of Duplex Stainless Steel, Mater. Trans. 50 (2009) 1548–1552. https://doi.org/10.2320/matertrans.MER2008168.

[107] G. Lorang, M.D.C. Belo, A.M.P. Simões, M.G.S. Ferreira, Chemical Composition of Passive Films on AISI 304 Stainless Steel, J. Electrochem. Soc. 141 (1994) 3347–3356. https://doi.org/10.1149/1.2059338.

[108] R. Ke, R. Alkire, Initiation of Corrosion Pits at Inclusions on 304 Stainless Steel, J. Electrochem. Soc. 142 (1995) 4056–4062. https://doi.org/10.1149/1.2048462.

[109] Gamry, Basics of Electrochemical Impedance Spectroscopy, (2020). https://www.gamry.com/application-notes/EIS/basics-of-electrochemical-impedance-spectroscopy/ (accessed October 2, 2020).

[110] T.H. Orem, Influence of crystallographic orientation on the corrosion rate of aluminum in acids and alkalies, J. Res. Natl. Bur. Stand. (1934). 58 (1957) 157. https://doi.org/10.6028/jres.058.022.

[111] X.Y. Wang, Z. Liu, P.H. Chong, Effect of overlaps on phase composition and crystalline orientation of laser-melted surfaces of 321 austenitic stainless steel, Thin Solid Films. 453–454 (2004) 72–75. https://doi.org/10.1016/j.tsf.2003.11.078.

[112] V. Venegas, F. Caleyo, L.E. Vázquez, T. Baudin, J.M. Hallen, On the influence of crystallographic texture on pitting corrosion in pipeline steels, Int. J. Electrochem. Sci. 10 (2015) 3539–3552.

[113] Introduction to Electrochemical Impedance Spectroscopy, 2015. https://www.gamry.com/assets/Uploads/Basics-of-Electrochemical-Impedance-

Spectroscopy.pdf.

[114] Common Equivalent Circuit Models Part 3, 2017.

[115] P. Ghods, O.B. Isgor, G.A. McRae, G.P. Gu, Electrochemical investigation of chloride-induced depassivation of black steel rebar under simulated service conditions, Corros. Sci. 52 (2010) 1649–1659. https://doi.org/10.1016/j.corsci.2010.02.016.

[116] M.E. Orazem, B. Tribollet, Electrochemical Impedance Spectroscopy, John Wiley & Sons, 2008.

[117] P. Murkute, O.B. Isgor, S. Pasebani, Electrochemical investigation of super duplex stainless steel cladded low carbon steel manufactured via powder bed selective laser melting, in: Corros. 2019, NACE International, 2019: pp. 1–10.

[118] L.N. Zhang, J.A. Szpunar, J.X. Dong, O.A. Ojo, X. Wang, Dependence of Crystallographic Orientation on Pitting Corrosion Behavior of Ni-Fe-Cr Alloy 028, Metall. Mater. Trans. B Process Metall. Mater. Process. Sci. 49 (2018) 919–925. https://doi.org/10.1007/s11663-018-1227-6.

[119] W. Tian, N. Du, S. Li, S. Chen, Q. Wu, Metastable pitting corrosion of 304 stainless steel in 3.5% NaCl solution, Corros. Sci. 85 (2014) 372–379. https://doi.org/10.1016/j.corsci.2014.04.033.

[120] D. Kong, X. Ni, C. Dong, L. Zhang, C. Man, J. Yao, K. Xiao, X. Li, Heat treatment effect on the microstructure and corrosion behavior of 316L stainless steel fabricated by selective laser melting for proton exchange membrane fuel cells, Electrochim. Acta. 276 (2018) 293–303. https://doi.org/10.1016/j.electacta.2018.04.188.

[121] T. Meesak, C. Thedsuwan, Corrosion behaviours of stainless steel parts formed by powder metallurgy process, Mater. Today Proc. 5 (2018) 9560–9568. https://doi.org/10.1016/j.matpr.2017.10.138.

[122] T. Li, J.R. Scully, G.S. Frankel, Localized corrosion: Passive film breakdown vs pit growth stability: Part v. Validation of a new framework for pit growth stability using one-dimensional artificial pit electrodes, J. Electrochem. Soc. 166 (2019) C3341–C3354. https://doi.org/10.1149/2.0431911jes.

[123] ASTM International, Standard Test Method for Conducting Cyclic Potentiodynamic Polarization Measurements for Localized Corrosion Susceptibility of Iron-, Nickel-,

or Cobalt-Based Alloys, West Conshohocken, 2018. https://doi.org/10.1520/G0061-86R18.